Hidden Sector Three Different Ways

Jakub Scholtz

A dissertation
submitted in partial fulfillment of the
requirements for the degree of

Doctor of Philosophy

University of Washington

2013

Reading Committee:

Ann E. Nelson, Chair

Stephen D. Ellis

Henry Lubatti

Program Authorized to Offer Degree:
Physics Department

University of Washington

Abstract

Hidden Sector Three Different Ways

Jakub Scholtz

Chair of the Supervisory Committee:
Professor Ann E. Nelson
Physics Department

This thesis is a compilation of three projects that explore the consequences of different Hidden Sector models in various experimental fields. The first project proposes the Hidden Sector is populated by just one $U(1)$ vector particle. It couples to the Standard Model through kinetic mixing and is responsible for a fraction of Dark Matter density of our Universe. The other two projects look at specific signals from a Hidden Sector with two light scalars coupled to the Standard Model through a Higgs Portal. One of these projects looks at collider consequences and the other projects explores how such Hidden Sector may alter rare decays of B-mesons.

TABLE OF CONTENTS

DEDICATION

To my dear wife Laura, my family, friends, colleagues and mentors without whom I would not get here.

Chapter 1

INTRODUCTION TO HIDDEN SECTORS

The Standard Model is very good. In fact, it is extremely good. You could say that it does not include neutrino masses, Dark Matter, Dark Energy, gravity and that our knowledge of the Higgs sector is very limited. Yet, you would be hard pressed to find 5σ deviations that would shed any light on how to include the missing parts.

But we do know there is more: Dark Matter. We certainly wish to build a successful theory of Dark Matter. On one hand, we are driven to believe that we should extend the Standard Model by the least amount necessary to build a such a theory. On the other hand, it seems absurd that the Dark Matter sector, which makes up five times as much energy density of the Universe, should be simple. If Dark Matter is a manifestation of its own non-minimal sector, then we may as well think about the consequences of the entire sector it is contained within.

Consider building an extension of the Standard Model by adding additional particles, say a Dirac fermion ψ. This new fermion is a singlet under the Standard Model gauge group transformations; it transforms as $(1, 1, 0)$ under $SU(3)_c \times SU(2)_W \times U(1)$. If the Lagrangian associated with our extension has no other particles and no operators that contain both Standard Model fields and ψ, there are no interactions possible between the Standard Model particles and ψ. Since we are exclusively made out of Standard Model particles it is impossible to interact with ψ. The particles associated with ψ can be considered a part of another sector that is hidden from us: the Hidden Sector. Of course, ψ is still coupled to the $\sqrt{\det g}$ term from the measure of integration ($\mathcal{S} = \int \mathcal{L}\sqrt{-\det g}dx^4$), so we could theoretically manipulate and detect ψ through its subtle gravitational effects.

Indeed, coupled with a reasonable mechanism that would populate the right density of ψ, this extension would present a perfectly good, albeit depressing, Dark Matter candidate. I call this scenario depressing because we can interact with this Hidden Sector only through

gravitational interactions suppressed by the Planck scale – particles in this Hidden Sector would be beyond the reach of any experiment we are currently able to fund or build. Although a completely decoupled Hidden Sector is a logical possibility, we are unable to test its consequences. Of course, we are far more interested in theories that can be experimentally tested. In order to create theories with testable consequences, model builders consider adding some interactions between the Hidden Sector and the Standard Model.

One way to add interactions between the Standard Model and the Hidden Sector fields is to include the so-called Portals. A Portal consists of a set of renormalizable operators [1] that involve both Hidden Sector and Standard Model fields. They usually arise from mixing between fields with the same representation from each sector. For example take a $U(1)$ vector field Φ_μ, with field strength $\Phi_{\mu\nu}$. Call it the Dark Photon. We can make the Dark Photon a Standard Model and Hidden Sector singlet, which means it is in the same representation as the Standard Model photon A_μ (with field strength $F_{\mu\nu}$). Since both $F_{\mu\nu}$ and $\Phi_{\mu\nu}$ are gauge invariant, the operator $\kappa F_{\mu\nu}\Phi^{\mu\nu}$ is gauge invariant and renormalizable – according to [1] it is a good operator to form a Portal. This kind of Portal, called the Kinetic Mixing Portal or $U(1)$ Portal, was first introduced by [2]. The parameter κ is a measure of probability that we detect a Dark Photon after we created a normal photon, due to the nonzero matrix element:

$$\langle A(p_1,\epsilon_1)|\kappa F_{\mu\nu}\Phi^{\mu\nu}|\Phi(p_2,\epsilon_2)\rangle = 2\kappa\left[(p_1p_2)(\epsilon_1\epsilon_2) - (p_1\epsilon_2)(p_2\epsilon_1)\right] \tag{1.1}$$

It is more convenient to approach this system in a different basis as will be explained in chapter 2.

In chapters 3 and 4 you will see another example of Portals: the Higgs Portal. This Portal, suggested in [1, 3, 4], arises from mass mixing between a Standard Model Higgs particle (or particles) and a Hidden Sector scalar. Note that in this case it is not necessary that the particles involved in the Portal are in the same representation: take an Hidden Sector scalar S, which is an Standard Model singlet. If S transforms trivially under every symmetry group of our model, then we can add a dimension three operator $\Lambda S(HH^\dagger - v^2)$, where v is the vacuum expectation value (vev) of the Higgs field H. Note that $(HH^\dagger - v^2)$

is a singlet and so is the entire operator[1]. After Electro-Weak symmetry breaking (EWSB), the operator $\Lambda S(HH^\dagger - v^2)$ contains $\Lambda v S h$, which mixes the neutral Higgs boson h and the scalar S. Even if S is not a singlet, the operator $\lambda(HH^\dagger - v^2)(SS^\dagger - w^2)$ is a singlet and after symmetry breaking in both sectors (should that happen) it will contain a mass mixing operator $\lambda v w h s$, where $s = S + w$ with w being the vev of the S field. As in the case of kinetic mixing, the probability to detect a s after radiating h is nonzero due to this operator; as in the Kinetic mixing case, it will be much more convenient to work in a different basis.

Whichever Portal is present, it allows interactions between the two sectors, making it possible to create and detect Hidden Sector particles with our instruments. This means that Hidden Sector with Portal models present hypotheses that may become, in principle, testable and are therefore worth proposing.

This thesis is a compilation of three projects that explore the consequences of different Hidden Sector models in various experimental fields. The first project proposes the Hidden Sector is populated by just one $U(1)$ vector particle. It couples to the Standard Model through kinetic mixing and is responsible for a fraction of Dark Matter density of our Universe. The other two projects look at specific signals from a Hidden Sector with two light scalars coupled to the Standard Model through a Higgs Portal. One of these projects looks at collider consequences and the other projects explores how such Hidden Sector may alter rare decays of B-mesons.

---

[1]I added the $-\Lambda S v^2$ term in order to remove the tadpole that arises from the $\Lambda S H H^\dagger$ operator after Electroweak symmetry breaking.

Chapter 2

COSMIC FRONTIER: DARK LIGHT, DARK MATTER AND THE MISALIGNMENT MECHANISM

2.1 Introduction to Cosmology

In the last two decades, Modern Cosmology has become a precision science. The main paradigm, Inflationary ΛCDM, has become the Standard Model of Cosmology. Although this model is very successful at explaining all the observations from Cosmic Microwave Background experiments, deep space surveys as well as supernovae observations, it does not explain the nature of its two dominant components: Dark Energy and Dark Matter.

In this Section, I will outline some of the basic features of this model. However, a reader interested in studying Cosmology would benefit from reading two books: *Modern Cosmology* by Scott Dodelson [5] and *Cosmology* by Steven Weinberg [6]. In my opinion it is best to start with the first for a gentler introduction and follow up with the second for more depth.

The Standard Model of Cosmology rests on two assumptions: Homogeneity and Isotropy of the Universe. A homogeneous Universe appears the same no matter where the observer is stationed; it is translation invariant. An isotropic Universe appears the same no matter which direction the observer looks; it is rotationally invariant. These two requirements are not exact. On small scales the presence of our Sun and the Milky Way as well as the local Galaxy Group obviously break these assumptions. However, on much larger length scales the Universe appears homogeneous and isotropic. This constrains the geometric structure of the Universe to the Friedmann-Robertson-Walker (FRW) metric:

$$ds^2 = -dt^2 + a(t)^2 \left[\frac{dr^2}{1 - kr^2} + r^2 d\Omega^2 \right], \tag{2.1}$$

where $a(t)$ is called the scale factor, $k \in \{-1, 0, 1\}$ determines the curvature of the Universe and $d\Omega$ is the usual spherical volume element. Notice that for $k = 0$, the length element is the flat space length element $dr^2 + r^2 d\Omega^2$. Our Universe is flat [7] and I will set $k = 0$ for

the rest of this thesis. A useful way to view this metric is to use a different time coordinate η, so that the metric becomes:

$$ds^2 = a(t)^2 \left[-d\eta^2 + dr^2 + r^2 d\Omega^2\right], \tag{2.2}$$

which can be achieved by demanding $d\eta = dt/a(t)$. Notice that in these coordinates radial light rays are parametrized by $d\eta = \pm dr$, and it is easier to study the causal structure of such a Universe. In order to determine the dependence of $a(t)$ on time we need to solve the Einstein equations:

$$G_{\mu\nu} = 8\pi G T_{\mu\nu} \tag{2.3}$$

Given the Universe is homogeneous and isotropic, we can constrain its energy-momentum tensor to a simple form corresponding to a isotropic, homogeneous fluid:

$$T_{\mu\nu} = \begin{pmatrix} -\rho & & & \\ & p & & \\ & & p & \\ & & & p \end{pmatrix} \tag{2.4}$$

The solutions to Einstein equations with our metric and energy-momentum tensor ansatze are called the Friedmann equations:

$$\begin{aligned} \left(\frac{\dot{a}}{a}\right)^2 &= \frac{8\pi G}{3}\rho \\ \frac{\ddot{a}}{a} &= -\frac{4\pi G}{3}\left(\rho + 3p\right) \end{aligned} \tag{2.5}$$

We call $\dot{a}/a = H$ the Hubble constant (although it is not a constant), because it describes the rate of the expansion of the Universe. This can be verified easily: the distance between two coordinate fixed points with coordinate distance Δr is $s = a(t)\Delta r$. This distance changes with time $ds/dt = \dot{a}(t)\Delta r$, therefore the rate at which two coordinate-fixed points recede from each other is proportional to their distance and the Hubble constant:

$$\frac{ds}{dt} = \frac{\dot{a}(t)}{a(t)} s = Hs \tag{2.6}$$

If we know $p(\rho)$ we can solve for time evolution of both $a(t)$ and $\rho(t)$, which would tell us all about the history of the Universe. Indeed assuming $p = w\rho$, we can solve these

equations easily. This is a useful assumption: for example, a universe filled with pressureless dust ($p = 0$) corresponds to a choice $w = 0$, and a universe filled with massless radiation corresponds to $w = 1/3$. With this assumption, unless $w = -1$, the solution to Friedmann equations are:

$$\begin{aligned} a &\sim t^{\frac{2}{3(w+1)}} \\ \rho &\sim a^{-3(w+1)} \end{aligned} \tag{2.7}$$

For pedagogical purposes I will now break the deductive flow and introduce the types of "matter" we find in our Universe.

We are all aware of the baryonic component of our Universe – this is us and all the matter you have ever seen. The baryonic matter is a misnomer since leptons are included, but the name stuck. All the stars, planets and gas (which forms the majority) are made out of the same Standard Model particles we encounter every day. However, they all make up only about 5% of the energy density of our current Universe. Stars and planets do not exert any significant pressure on each other and neither does gas. It may seem wrong to conclude that gas can be described as pressureless: after all, $pV = nRT$. However, a nonrelativistic collection of particles with mass m has an energy density approximately equal to $\rho \sim mn$ and so $p = w\rho = \rho(T/m)$. Therefore, until the gas becomes relativistic (very hot), it is as good as pressureless and $w = 0$ is a great approximation.

There is a large and growing body of evidence that another pressureless component of our Universe exists. Already in the first half of the 20th century Zwicky suggested to solve an apparent discrepancy in galactic rotation curves by adding missing non-luminous matter [8]. The discrepancy he was proposing to solve is between the predicted and the measured velocity distributions of stars inside galaxies. The principle behind such comparison is rather simple: we believe we can measure the density of matter in a galaxy by tracking the luminosity of a galaxy as a function of its radius. Assuming we understand the ratio between luminous and non-luminous matter in a galaxy, we can reconstruct the gravitational potential of the galaxy, and hence predict orbital velocities of its stars – the rotation curve. We can also measure the redshift difference between the light coming from opposite edges of a given annulus inside the galaxy, which gives us a direct measurement of the stars' velocities.

Figure 2.1: A composite image of the Bullet Cluster: Stars measured in the visible spectrum (shown in their own color), hot gas is imaged in X-rays (shown in red) and the weak lensing potential (shown in blue).

In the second half of 20th century Rubin and Ford made precision measurements [9] and observed that the inferred and the measured velocity profiles do not agree for many galaxies. Today's even more accurate measurements indicate that the discrepancy can be removed by adding a diffuse halo of particles. We call this missing component Dark Matter. Since a diffuse halo resolves the discrepancy we conclude that Dark Matter does not interact with itself very much, otherwise it would collapse into a disc just as the baryonic component of the galaxy did.

As you will see in the following paragraphs nonrelativistic DM is also required for a correct structure formation and to produce the correct fluctuations of the Cosmic Microwave Background. Finally, there is a beautiful example of a system in which two clusters of galaxies collided in the past – the Bullet Cluster. The galaxies themselves have their paths almost unaltered, as collisions between them are very rare. However, the gas that forms a much bigger component of the galaxy clusters can be observed in X-rays. We can see the shockwave produced by the collision as well as that the gas is now lagging behind the free

moving galaxies in figure 2.1. However, the weak lensing data shows that majority of the mass of the two clusters does not correspond to where the gas is. This evidence points to existence of another type of gravitationally bound matter that interacts very weakly with itself as well as with the interstellar gas.

Dark Matter is not the only theory that attempts to resolve these issues. Since all of the above discrepancies stem from gravitational effects, some theories propose to modify either gravitational laws or equations of motion for matter. These theories are called Modified Newtonian Dynamics (MOND) and Modified Gravity (MOG). For a good summary I would refer the reader to [10]. To my best knowledge, none of these theories presents an elegant solution to all the issues outlined above. Therefore, in this thesis I am going to assume Dark Matter exists and solves these problems.

Our Universe also contains a very dilute gas of photons. These photons dominated the early Universe but as the Universe cooled this photon gas made up an increasingly smaller part of the total energy density. A pure $U(1)$ gauge theory is conformal, which constrains the trace of energy momentum tensor: $T^{\mu}_{\mu} = 0$, which implies $w = 1/3$. The radiation component of our Universe, called the Cosmic Microwave Background, has temperature 2.7 K which corresponds to energy density of about 5×10^{-5} of the total energy density of the Universe.

Until recently, I would have you believe this would be the end of the list of types of matter in our Universe. However, in 1998 a group of astronomers found evidence [11] for another component: Dark Energy. Observing supernovae, they measured that $\ddot{a} > 0$: the Universe is accelerating in its expansion. This kind of behavior can be achieved in a universe that is dominated by a fluid with $w < -1/3$, from equation 2.7. Our Universe is dominated by Dark Energy: about 70% of its energy density is made up by Dark Energy. The special case $w = -1$ corresponds to the cosmological constant, for which $\rho = \text{const}$ and $a \sim e^{H}t$, with $H = \rho^2/(8\pi G)$ being a true constant. For a better summary of the entire issue you can read [12].

Since energy density of a box filled with photons is proportional to T^4, the temperature of a radiation-dominated Universe drops with the scale factor $T \sim a^{-1}$, which is the faster than any other type of matter. Today, we measure the temperature of Cosmic Microwave

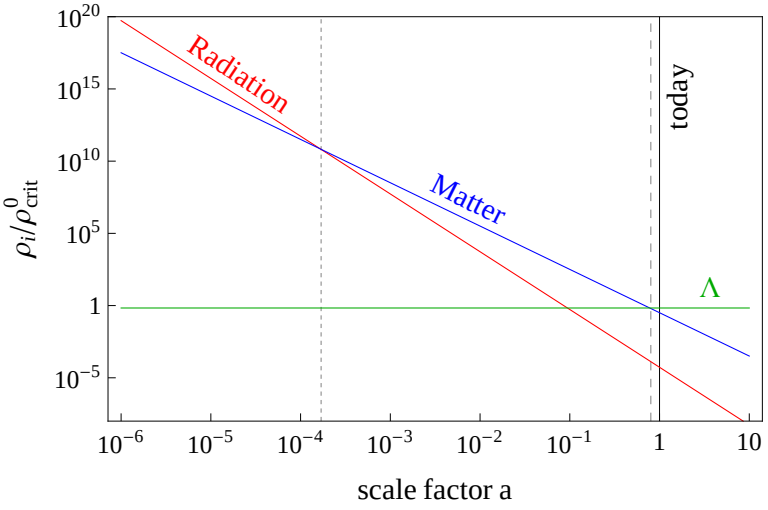

Figure 2.2: Extrapolating backwards from today's Universe, we can track the evolution of relative energy density of various components. The scale factor has been normalized so that $a = 1$ corresponds to today. The dashed line indicates the time when our Universe became Dark Energy dominated and the dotted line marks the transition from a radiation-dominated Universe to matter-dominated Universe. The energy density of different components has been normalized to the current critical density of our Universe.

Background Radiation $T \sim 2.7$ K, by extrapolation when the Universe was sufficiently young it was much hotter, and its energy density was dominated by radiation. I plot how the various components of the Universe evolved in figure 2.2.

How exactly did the Cosmic Microwave Background come about? Imagine a Universe filled with radiation and a little bit of ordinary matter. Above the ionization temperature of ordinary matter our Universe is filled with free charged particles. Therefore, photons will have a very short scattering length, and will be in local equilibrium with the charged matter. Once the temperature drops below the ionization temperature, some of the proton-electron pairs bind, reducing the amount of free charge. This makes the average scattering length of photons much longer and makes the Universe transparent to these photons. The time slice at which this happens is called the Surface of the Last Scattering. Since photons do

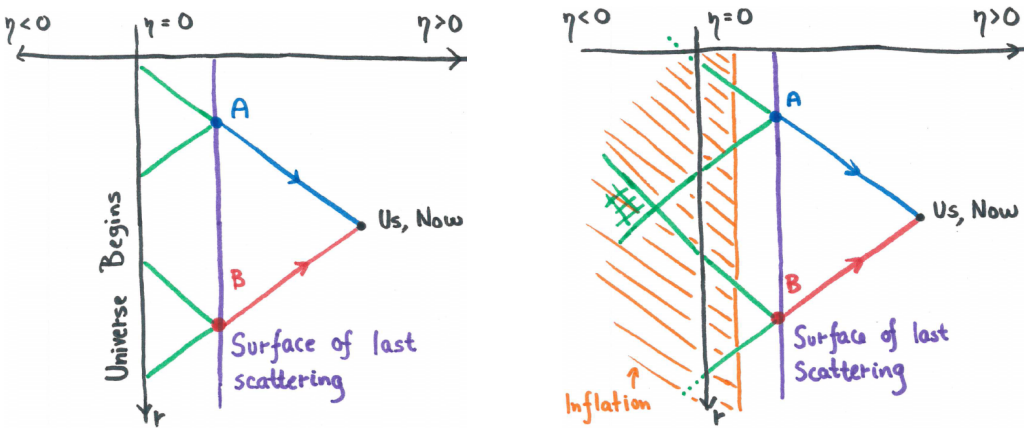

Figure 2.3: Inflation solves the problem...

not interact much with matter after this period, they carry a slowly redshifting snapshot of what our Universe looked like at the Surface of the Last Scattering.

A systematic full sky study of the Cosmic Microwave Background started with the Cosmic Background Explorer (COBE), continued with the Wilkinson Microwave Anisotropy Probe (WMAP) and has recently been improved by the Planck mission. It is important to add that there were also earlier and concurrent balloon missions and ground telescope observations that contributed significantly to our studies of the Cosmic Microwave Background, despite the fact they did not provide full sky coverage. The first thing we notice about the Cosmic Microwave Background is that it is incredibly uniform. Once we remove the dipole caused by Earth's motion with respect to the Cosmic Microwave Background, these deviations are on the order 10^{-4}. On one hand, this tells us the Universe was very isotropic at the Last Scattering Surface. However, it also causes a significant problem for our cosmology: it implies that the entire Surface of the Last Scattering was in causal contact. The left panel of figure 2.3 illustrates this. The blue and red light rays traveled to us from points A and B on the Surface of Last Scattering. However, the past lightcones of A and B share a past only if the conformal time from beginning of our Universe to Surface of Last Scattering is larger than the conformal time from the surface to present: $\eta_{LS} - \eta_0 > \eta_{now} - \eta_{LS}$. We can verify that this is not true and that past lightcones of A and B have no points in common.

However, suppose that at some very early stage before the Last Scattering, our Universe went through a phase of accelerating expansion – a period of Inflation. As we have seen before, this corresponds to a universe dominated by Dark Energy with $w \leq -1/3$. In order to probe the causal structure of this universe, I will switch to the covariant time:

$$\Delta\eta = \int_0^{t'} \frac{dt}{a(t)} \sim \begin{cases} \frac{1}{a_0} \log(t)\Big|_0^{t'} & w = -\frac{1}{3} \\ \frac{3(w+1)}{a_0(3w+1)} t^{\frac{3w+1}{3(w+1)}}\Big|_0^{t'} & -1 < w < -\frac{1}{3} \\ \frac{1}{a_0 H}\left(1 - e^{-Ht'}\right) & w = -1. \end{cases} \tag{2.8}$$

First, we notice that for $-1 < w \leq -1/3$, $a = 0$ at $t = 0$ marks the beginning of such a universe. However, $t = 0$, corresponds to $\eta \to -\infty$, and past lightcones of A and B have enough time to intersect. If $w = -1$, then there is no time such that $a = 0$, and such a universe has an infinite past in coordinate t as well as in conformal time η, the past lightcones of A and B have enough time to intersect. The second picture in figure 2.3 illustrates how Inflation extends the conformal past of A and B and solves this problem.

Inflation solves other problems. Although I have elected to choose $k = 0$ in equation 2.1, the initial conditions for a universe that appears flat at later stages of its evolution seem fine-tuned unless this universe goes through an Inflationary stage. Moreover, the large expansion factor dilutes all kinds of exotic objects that we do not observe in our Universe, such as magnetic monopoles and cosmic strings.

So far we have learned about the uniformity of the Cosmic Microwave Background. We can learn even more by studying the spectrum of its deviations from uniformity. Usually, we decompose its excitations into spherical harmonics and plot the power in each. Figure 2.4 show the sky and its spherical decomposition as seen by the Planck Satellite [7]. The peaks in the observed spectrum are sensitive to many cosmological parameters such as matter density, baryonic density (Dark Matter density is their difference), Dark Energy density as well as curvature of the Universe. A great way to get a feel for how these peaks depend on various cosmological parameters can be found on Professor Hu's website [13] as well as in [14]. Figure 2.1 contains a small subset of plots from this paper. Given the small measurement uncertainties visible in the Planck data, the reader can see that we have a strong case for a Universe with 70% Dark Energy, 25% Dark Matter, 5% Ordinary Matter

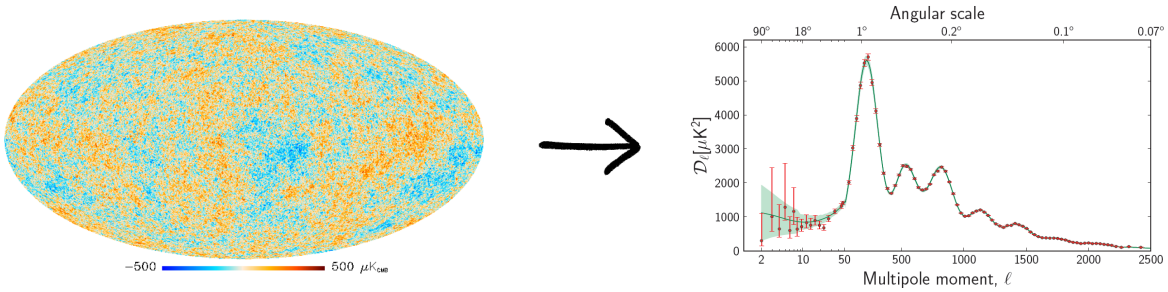

Figure 2.4: The temperature map of the Cosmic Microwave Background and its decomposition into spherical modes [7].

and a small amount of radiation.

2.1.1 Conclusion

Modern Cosmology relies on a large set of independent measurements that give us powerful insights into history of our Universe. The Dark Matter component of this model is necessary to explain many phenomena including structure formation, the precise shape of the Cosmic Microwave Background spectrum and rotational curves of galaxies. This component does not seem to interact much with ordinary matter and itself. There are many different motivated Dark Matter theories such as axions and Weakly Interacting Massive Particles. Nevertheless it is possible they are incorrect. The following section is a paper [15] we have written with Ann Nelson in order to propose an unusual Dark Matter candidate.

2.2 Dark Photon

Although some authors [16–18] have proposed that Dark Matter is a vector particle, none have succeeded in generating a sufficient relic density. We propose a variation that allows us to generate an extremely cold light vector component of the Universe, with a pressureless equation of state. Our inspiration comes from the fact that nature seems to make use of almost every renormalizable Lagrangian term: Abelian and Non-Abelian gauge theories,

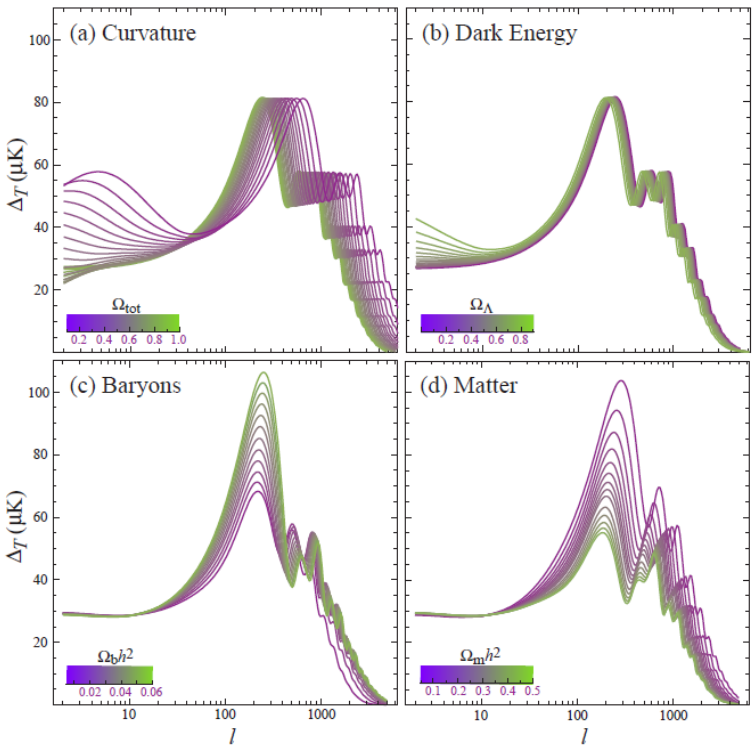

Figure 2.5: The power spectrum of the Cosmic Microwave Background and its dependence on various cosmological parameters.

Yukawa couplings as well as ϕ^4 theory. Yet, even though the Stueckelberg mass [19, 20] is renormalizable in four dimensions, it does not appear in the Standard Model. If Nature indeed does not make arbitrary choices among consistent theories, then there should exist a spin one field with a Stueckelberg mass. Therefore, if this boson is sufficiently weakly coupled to the Standard Model, it is worth considering whether it is a good candidate for Dark Matter. It is easy to populate the Universe with this particle: like the axion [21], during Inflation the expectation value of a light boson fluctuates. Immediately after Inflation, the value of the field in our horizon is a randomly selected (or perhaps anthropically selected [22–24]) initial condition. After Inflation, when the Hubble constant is of order of the boson mass, the field begins to oscillate. This oscillating field may be thought of as a Universe-sized Bose-Einstein condensate, as described in section 2.2.2. Such a particle is allowed to kinetically mix with the photon via a renormalizable interaction. Therefore, at some level, it presumably does mix, although no lower bound on the mixing parameter is required for the model to work. In section 2.2.4 we find the upper bounds on the kinetic mixing parameter such that the early Universe neither thermalizes nor evaporates this condensate. We also ensure that the vector boson lifetime is sufficiently long, and consider constraints on the coupling from possible apparent Lorentz violating effects.

2.2.1 A Model of Light Vector Dark Matter

Our massive vector will be represented by ϕ^μ in a Lagrangian of the form:

$$-\mathcal{L} = \frac{1}{4}\left(F^{\mu\nu}F_{\mu\nu} + \phi^{\mu\nu}\phi_{\mu\nu} + 2\chi\phi^{\mu\nu}F_{\mu\nu}\right) + \frac{M^2}{2}\phi_\mu\phi^\mu + J_\mu A^\mu \tag{2.9}$$

where A^μ and $F^{\mu\nu}$ represent the field strength of ordinary photon, J^μ is the ordinary charged current and $\phi^{\mu\nu} = \partial^\mu\phi^\nu - \partial^\nu\phi^\mu$. Applying a non-unitary transformation $A \to A - \chi\phi$ and $\phi \to \phi + \mathcal{O}(\chi^2)$, we can redefine our fields in terms of the mass eigenstates called *massless* photon and *heavy* photon:

$$-\mathcal{L} = \frac{1}{4}\left(F^{\mu\nu}F_{\mu\nu} + \phi^{\mu\nu}\phi_{\mu\nu}\right) + \frac{M^2}{2}\phi_\mu\phi^\mu + J_\mu(A^\mu - \chi\phi^\mu) \tag{2.10}$$

By rotating ($\tilde{A} = A - \chi\phi$ and $\tilde{\phi} = \phi + \chi A$) we can reach the flavor eigenstates, called *interacting* and *sterile* photon. These two mix through their mass term:

$$-\mathcal{L} = \frac{1}{4}\left(\tilde{F}^{\mu\nu}\tilde{F}_{\mu\nu} + \tilde{\phi}^{\mu\nu}\tilde{\phi}_{\mu\nu}\right) + \frac{M^2}{2}(\tilde{\phi}_\mu - \chi\tilde{A}_\mu)(\tilde{\phi}^\mu - \chi\tilde{A}^\mu) + J_\mu\tilde{A}^\mu \tag{2.11}$$

Unless otherwise stated, we will use the mass eigenstate basis. In this basis, the heavy photon couples to the electromagnetic current with the coupling constant scaled by $e \to \chi e$. In the limit $M = 0$, we could perform a rotation between the degenerate heavy and light eigenstates to a new set of states, one of which would be massless and completely decoupled. However, if we assume the heavy photon is the Dark Matter, with a finite energy density produced via the misalignment mechanism, then the number density is inversely proportional to the mass and therefore it makes no sense to take this limit.

Note that the model has two free parameters: M and χ. Fundamental theory gives us little guidance for their values. The theory is technically natural for any values of M and χ, in the sense that for a cutoff of order the Planck scale, the renormalized values are of similar size to the bare values. If we assume that the $U(1)$ of the Standard Model is grand-unified into a semi-simple or simple group, then χ can only be induced via loop corrections. In this case, if the mass of the particles in the loops m_C is below the grand unification scale Λ_{GUT}, the natural size of χ is of order $(g^2/(16\pi^2))^n$, where n is the number of loops required to induce the kinetic mixing, and g is the relevant combination of coupling constants in the loops. We will see that for ϕ to be viable Dark Matter, χ has to be tiny, less than 10^{-7} over the entire mass range, so for $g \sim 1$, n should be greater than or equal to about 3. If the particles in the loops are heavier than the grand unification scale, there is an additional suppression of at least $(\Lambda_{GUT}/m_C)^2$.

2.2.2 Misalignment Mechanism for Vector Dark Matter genesis during Inflation

The misalignment mechanism for producing a boson condensate has been considered in connection with the axion [21, 25–28] and various other light scalar fields such as moduli. Spatially varying modes of a bosonic field will be smoothed by the expansion of the universe. However the zero-momentum component of the scalar field A in the Friedmann-Robertson-

Walker (FRW) background has the equation of motion:

$$\ddot{A} + 3H(t)\dot{A} + m^2 A = 0 \tag{2.12}$$

which is reminiscent of a harmonic oscillator, with a time dependent damping term $H(t)$. In the early Universe, $H(t) \gg m$, the scalar is effectively massless and its Compton wavelength does not fit into the horizon. The field is stuck: it does not go through a single oscillation and therefore we observe no particles. The value of the field is assumed to take on some random nonzero value, because when the mass term is negligible there is no reason to prefer a field value of $\phi^\mu = 0$. An episode of Inflation will generally produce a spatially uniform field, but for $m \ll H$ in any causally connected patch of the universe the mean value of the field takes on some random, non zero value. After Inflation, the Hubble constant begins to decrease. As soon as the discriminant $9H^2 - 4m^2$ becomes negative, the field A begins to oscillate and we can quantize the different modes and call them particles. Since, up to the small perturbations in the temperature, $H(\eta)$ is everywhere the same, the transition happens everywhere in the Universe at the same time (in the rest frame of A). We are left an energy density which may be thought of as a coherent state of a macroscopic number of particles. The particles are extremely cold and nonrelativistic, whatever their mass. An adiabatic perturbation spectrum arising from the fluctuations of the Inflaton field [28, 29] will imprint adiabatic spatial variations on the density of the scalar particles, as is needed to fit the WMAP data. On large distance scales, compared with the particle Compton wavelength $1/m$, the dynamics of gravitational structure formation is identical to that for any weakly interacting massive particle.

Note that Inflation will produce isocurvature perturbations arising from fluctuations of the scalar field A. Such perturbations are highly constrained, and will place an m dependent upper bound on the Inflation scale [21, 23, 28, 30–34] for this scenario.

We can show that the same scenario applies to a light massive vector in an FRW Universe. As shown in the appendix, the equation of motion for such a vector is:

$$-\partial_\nu \left(\phi^{\mu\nu}\sqrt{-g}\right) = -M^2\phi^\mu\sqrt{-g} \tag{2.13}$$

As Inflation blows up a small patch of space, we can assume the Dark Photon is uniformly distributed and picks a particular polarization. This means that in the Cosmic frame $\partial_i\phi^\mu =$

0, and the time component of (2.13) implies $\phi^0 = 0$ as long as $M \neq 0$. The spatial component of (2.13) satisfies:

$$\ddot{\phi^i} + 3H\dot{\phi^i} + M^2\phi^i = 0 \tag{2.14}$$

We see that each spatial component of the vector satisfies the same equation of motion as the scalar A in the previous example and so has the same dynamics. After entering the lightly damped oscillation regime the vector behaves just like dust, with $d(\rho a^3)/dt = 0$, where $\rho = \langle M^2\phi^2 \rangle$. Taking the upper bound of $\phi = m_{pl}$ when $M \sim H$ we can see that the mass of ϕ^μ should satisfy $M \geq \Omega_{DM}^2 H_0 \hbar = 6.6 \times 10^{-35}$eV. This mass corresponds to a wavelength of about 10^{11}pc. This lower bound on the mass is weaker than the one implied by the existence of compact galaxies [35] with $L \sim 1$ kpc and $M_{CG} \sim 2 \times 10^{11} M_\odot$. Requiring that the Compton wavelength of the Dark Matter is low enough to allow structure formation on the kiloparsec scale gives a sharper bound on the lowest mass:

$$1 \text{ kpc} < \frac{\hbar}{\Delta p} = \frac{\hbar}{M v_{esc}} \quad \Rightarrow \quad M \geq 1.67 \times 10^{-24} \text{ eV} \tag{2.15}$$

The amount of Dark Matter produced by this mechanism becomes simply a randomly chosen initial condition for the value of the field in our patch of the universe. In other regions of the universe, which are beyond our current horizon, the Dark Matter abundance is different. In [24] it was shown that for an axion or similar Dark Matter condensate produced during Inflation, assuming other parameters do not vary, the regions of Universe with Dark Matter abundance of the same order as observed in our Universe are the most highly correlated with physical features of our Universe that seem favorable for the existence of observers, allowing for an "anthropic" explanation of the Dark Matter density.

2.2.3 Stueckelberg versus the Higgs mechanism

The vector mass $M^2\phi^\mu\phi_\mu$ is not manifestly gauge invariant. In the Standard Model of particle physics, all massive vector particles acquire their mass due to a Higgs mechanism. However, if the ϕ were to get its mass from the Higgs mechanism, the inflationary misalignment mechanism will not work to produce a condensate. Assuming the Higgs Lagrangian is:

$$\mathcal{L} = [(\partial_\mu + ig\phi_\mu)\varphi]^2 + \lambda(\varphi^2 - m^2/(2\lambda))^2 \tag{2.16}$$

the mass term for ϕ is $M^2\phi^2 = g^2m^2\phi^2/(2\lambda)$, however, the symmetry breaking happens around $T^2 \sim m^2/g^2$, which implies that the ϕ is massless above this temperature. Therefore, in order to make sure that there exists a time when $M \leq H(T)$ while ϕ is not massless, we need to satisfy:

$$1 \leq H/M = \frac{T^2}{Mm_{pl}} = \frac{m^2}{Mg^2m_{pl}} = \frac{2\lambda M}{g^4 m_{pl}} \tag{2.17}$$

Therefore we need:

$$\frac{M}{m_{pl}} \geq \frac{g^4}{2\lambda} \tag{2.18}$$

We can look at the Z boson to illustrate this condition: the right hand side is of the order $2g^4v^2/m_h^2 \sim 10^{-3}$ even for a heavy Higgs (500 GeV) and so a condensate of W and Z bosons could not have been created by a misalignment mechanism. However, one could imagine taking the limit in which $M^2 = g^2v^2 = g^2m^2/2\lambda$ is fixed, but both $m_h \to \infty$ and $\lambda \to \infty$. In this case the right hand side of (2.18) can be made arbitrarily small and the vector retains its mass for arbitrarily high temperature. The limit $m_h \to \infty$ can be handled in a better way: parametrize the Higgs in polar coordinates $\varphi = (v + h)e^{i\theta/v}$ and integrate out the heavy h. The effective Lagrangian of the light degrees of freedom takes the form:

$$\mathcal{L} = -\frac{1}{4}F^2 - \frac{1}{2}(MA^\mu + \partial^\mu\theta)^2, \tag{2.19}$$

which is identical to the Stueckelberg Lagrangian [19, 20], with θ filling the role of the Stueckelberg scalar field that fixes the correct number of degrees of freedom for a massive vector. This Lagrangian is still invariant under:

$$\begin{aligned} \Delta_\lambda A &= A + \partial\lambda \\ \Delta_\lambda \theta &= \theta - M\lambda \end{aligned} \tag{2.20}$$

A redefinition $\phi^\mu = A^\mu + \partial^\mu\theta$ leads to $F^{\mu\nu} = \phi^{\mu\nu} = \partial^\mu\phi^\nu - \partial^\nu\phi^\mu$ and gives us a massive vector described by:

$$\mathcal{L}_\mathcal{S} = -\frac{1}{4}\phi^{\mu\nu}\phi_{\mu\nu} - \frac{M^2}{2}\phi^\mu\phi_\mu \tag{2.21}$$

Naturally, this Lagrangian is still invariant under Δ_λ, although it is not invariant under the naive gauge transformation $\phi^\mu \to \phi^\mu + \partial^\mu\lambda$. Unlike the nonabelian case, for a $U(1)$ gauge theory, the Higgs boson is not needed to unitarize the scattering of the longitudinal mode of a massive vector boson, and is unnecessary for renormalizability.

2.2.4 Bounds

Early Universe - Compton Evaporation

In order to be a successful Dark Matter candidate, the Dark Photon has to be a stable particle both in a vacuum and in the dense, ionized early Universe. For light ϕ bosons, we need to ensure that the Dark Photon population does not get thermalized, otherwise it would become relativistic and fail to be a good Dark Matter candidate. As with photons and plasmas, the main process for thermalization is the Compton-like scattering process: $\phi e^{\pm} \to \phi e^{\pm}$. However, this process will be suppressed by a factor of χ^2 with respect to two other processes: $\phi e^{\pm} \leftrightarrow \gamma e^{\pm}$. We will call the right-going process Compton evaporation and the left-going Inverse Compton evaporation. In order to ensure there are enough Dark Photons left after interaction with plasma, we require that the Compton evaporation rate Γ is smaller than the expansion rate of the universe $H(T)$. This condition also implies that the thermalization rate from Compton-like scattering is small and there is enough cold Dark Matter to populate our Universe. In order to investigate this bound we need to know the product of the velocity and cross-section $v\sigma(M,p)$ as a function of the Dark Photon mass M and electron three-momentum p, which can be re-expressed for $M \ll m_e$:

$$v\sigma(M,p) = \frac{8\alpha^2\chi^2\pi(3m^2+2p^2)}{9m^2(m^2+p^2)} + \mathcal{O}(M) \tag{2.22}$$

The width of the Dark Photon in plasma is then given by the thermal average over the electron momentum density distribution for a given temperature of the Universe. We would like this width to be smaller than the characteristic expansion rate of the Universe at a given temperature:

$$H(T) > \Gamma(T) = \int dp^3 \sigma(M,p) v(p) n(p,T,\mu(T)) \tag{2.23}$$

Where we have used the exact $\sigma(M,p)$, not the approximate expression (2.22), $n(p,T,\mu)$ is the Fermi-Dirac distribution with chemical potential μ. We have chosen $\mu = 0$ for $T \gtrsim m_e$. For $T < m_e$ we picked μ to be consistent with today's electron co-moving density. Given that the early Universe is growing less and less dense, the strongest bound on χ is in effect at the earliest time the Dark Photon is present, when the misalignment

mechanism kicks in at $M \sim H$. This guarantees that if the Dark Photon survives the first characteristic time period, then it will not evaporate anymore during the subsequent time. The condition $H \sim \Gamma$ does not guarantee this, but is a lower bound on such survival. We find it is unnecessary to consider particles other than the electron, since the contribution of all other charged particles with mass m_i and charge q_i will be suppressed by a factor $g_i(m_e/m_i)^2(q_i/q_e)^4$, which together with their suppressed thermal momentum distributions will make their contribution small. Likewise, it is unnecessary to consider other evaporation processes such as $\phi\gamma \to \gamma\gamma$ since they become important for Dark Photon mass of order $M = (m_{pl}m_e^2)^{1/3} \sim 10^{13}$ eV – well above the range we consider in this paper.

The bound imposed by Compton evaporation is plotted in figure 2.7 and labeled Early Universe. We would like to point out two features. When the Universe reaches temperatures of order $T \sim 0.1m_e$, its free charge density significantly drops and the evaporation process becomes much less effective. This temperature marks the generation of Dark Photon with mass $M \sim T^2/m_{pl} \sim 10^{-18}$ eV, hence the sharp dip in the bound on χ in this region. On the other hand, since the cross-section starts dropping off when $\sqrt{s} \sim m_e^2/M$ and $\sqrt{s} \sim T$, we can estimate a change in the slope of the bound around $M \sim (m_e^4/m_{pl})^{1/3}$. This agrees with the observed dip at $M \sim 10^{-2}$ eV.

Decays

Apart from Compton evaporation, we can consider pure vacuum decay processes, which become significant once $M > m_e$ or $M > M_W$. Requiring that the Dark Photon is stable on cosmological timescales requires that $\sum \Gamma_i < H_0$:

Process	Width	Notes
$\phi \to l^+l^-$	$\Gamma_1 = \chi^2\alpha\frac{M^2+2m_l^2}{2M^2}\sqrt{M^2-4m_l^2}$	$M > 2m_l$, Exact
$\phi \to \nu\bar{\nu}$	$\Gamma_2 = \frac{\chi^2\alpha^3}{16\pi}\left(\frac{M}{M_W}\right)^4\sqrt{M^2-4m_\nu^2}$	Estimate of the loop process
$\phi \to \gamma\gamma\gamma$	$\Gamma_3 = \frac{17\chi^2\alpha^4 M}{11664000\pi^3}\left(\frac{M}{m_e}\right)^8$	See [36], valid for $M < m_e$

The bounds imposed by these decays are plotted in figure 2.7.

Earth Detection

Although ϕ_μ does not satisfy Maxwell's equations, its coupling to ordinary matter is the same as that of the photon A_μ. Therefore, a nonzero ϕ_μ will appear as a combination of electric and magnetic fields with strength suppressed by a factor of χ. Such fields will be detectable in various precision experiments and it is our desire to quantify the expected phenomena as accurately as possible.

By our hypothesis, in the Dark Matter rest frame $\phi_\mu = \delta_{\mu 3} A_3 \cos(Mt)$ therefore it mimics an electric field $E_3 = \chi A_3 M \sin(Mt)$. Given that the local density of Dark Matter is $T_{00} = M^2 A_3^2/2 = 0.3\,\mathrm{GeV/cm^3}$, we can infer that the amplitude of the electric field is

$$E = \sqrt{2 \times 0.3\,\mathrm{GeV/cm^3}/\epsilon_0} \approx 3300\chi\,\mathrm{V/m} \tag{2.24}$$

However, there is no reason to believe that the Dark Matter rest frame is identical with the Earth frame and hence we need to perform a Lorentz boost to the right frame. Given $\vec{\phi} = (\phi_x, \phi_y, \phi_z)\cos(Mt)$ and the velocity with respect to the Dark Matter rest frame $\vec{v}$, the B-fields in the Earth frame will be:

$$\vec{B} = \vec{\nabla} \times L_{\vec{v}}(\vec{\phi}) = \gamma M \vec{v} \times \vec{\phi} \cos(\gamma M t). \tag{2.25}$$

We should note that at $v = 0.001c$, $\gamma = 1 + \mathcal{O}\left(10^{-6}\right)$, and that $|M\phi|$ is the magnitude of electric field in the Dark Matter rest frame. Therefore the B-field is simply $\vec{B} = \vec{v} \times \vec{E}$, precisely as expected.

Attenuation

If these fields are to be detected by Earth-based experiments we need to check that the Dark Photon field is not screened by the atmosphere or by the many shields that experimental physicists put up in order to protect their experiments from stray electric and magnetic fields. In materials, bound electrons will only contribute to shielding if M falls close to some energy gap of a kinematically allowed transition, however, even such transitions will be suppressed by factor of χ^2. On the other hand, free electrons in metals will allow a

continuum of transitions, that would lead to Compton evaporation effects. Therefore, we will treat the interaction of Dark Photons with materials as a wall penetration by weakly interacting particles, similarly to what we have done with the early Universe. The change in Dark Photon density will be proportional to:

$$a = \exp\left(-\int dx\, n(x)\sigma(M, v)\right) \tag{2.26}$$

where $n(x)$ is the free electron density of the shielding material and $\sigma(M, Mv)$ is the Compton Evaporation cross-section and $v = 0.001c$ is the assumed velocity with respect to the local Dark Matter flow. Given that the respective average densities of free electrons in the ionosphere and copper are $n_{at} \sim 3 \times 10^{11}$ m^{-3} and $n_{\rm Cu} \sim 10^{29}$ m^{-3}, it is clear that a whole column of 1000 km of atmosphere corresponds to a layer of metal about 10^{-12} m thick – much less than any normal electric shielding of earthborne experiments hence we can disregard this contribution. Moreover, the early Universe bound on χ gives an attenuation length longer than 1 m in a copper plate; once combined with the bounds from the next section, the attenuation length is larger than 10^{10} m.

Atomic Physics

The Stark effect associated with the background dark electric field would induce a shift in the ground state energy of a hydrogen-like atom of the order $\Delta E_S = -m_e(3a_0^2 eE_d/2\hbar)^2 \sim \chi^2 \times 10^{-15}$ eV, which is 5 orders of magnitude smaller than the current limits [37], even if $\chi = 1$. The Zeeman effect would produce a shift of $\Delta E_Z = 5\chi \times 10^{-13}$ eV. This is still too small to register. The advantage of the Zeeman effect is that it is linear the field magnitude, hence in χ, which makes up for the fact that the magnetic field is suppressed by a factor of v/c. However, effects linear in fields go as $\cos(Mt)$, implying a zero time average, and so a search without prior knowledge of M would be time consuming. However, in the region of small mass ($M \lesssim 10^{-22}$ eV ~ 1 year) the slow oscillations imply no need for averaging. In this regime the slowly changing background electric field would mimic a slow drift in α. As an example we can take a system comprised of two clocks: one driven by two photon transition from $1s \to 2s$ in hydrogen and the other by the hyperfine transition in Cesium. The major correction to the hydrogen clock rate comes as a Stark effect with a relative shift

in the frequency:

$$\frac{\delta\omega}{\omega} = \frac{\Delta E_{1s} - \Delta E_{2s}}{E_{1s} - E_{2s}} = -\frac{\Delta E_{2s}}{E_{1s} - E_{2s}} = \sum_{n\geq 2} \frac{|\langle 2,0,0\,|e\mathcal{E}z|\,n,1,0\rangle|^2}{(E_{200} - E_{n10})(E_{200} - E_{100})} \tag{2.27}$$

Notice that the $n = 2$ term dominates the sum since the degeneracy of the 2s and 2p states is broken by the lamb shift with $\Delta E(2p - 2s) \sim 10^{-6}$ eV, whereas the rest is on the order of 1 eV. Therefore:

$$\frac{\delta\omega_{\rm H}}{\omega_{\rm H}} = \frac{0.55(\chi e\mathcal{E}a_0)^2}{(\Delta E_{lamb})(E_{1s\to 2s})} \sim 4\chi^2 \times 10^{-10} \tag{2.28}$$

Note that the Zeeman shift is identical for the 1s and 2s orbitals, therefore there is no contribution linear in χ.

In Cesium the Stark shift does not distinguish the states, but the Zeeman effect contributes by splitting the hyperfine triplet into three distinct levels, and induces a change in the clock frequency on the order:

$$\frac{\delta\omega_{\rm Cs}}{\omega_{\rm Cs}} = -\frac{\mu_e B}{\Delta E_{hyp}} \sim 1.5\chi \times 10^{-8} \tag{2.29}$$

Clearly the Cesium clock effect dominates for small χ. Therefore, as $\mathcal{E}$ oscillates very slowly, the experiment sees a drift in $\delta\omega/\omega$, which could be (naively) interpreted as drift in α of the order:

$$\frac{\dot{\alpha}}{\alpha} = M\frac{\delta\omega}{2\omega} \sim 1.5\chi \times 10^{-8} \left(\frac{M}{10^{-22}\text{ eV}}\right)\ \text{year}^{-1} \tag{2.30}$$

However, if the frequency of the oscillations is comparable to the time scales of an experiment, such as sampling rate and averaging times of individual data points, the sensitivity becomes more complicated. We pick [38] as a model example to illustrate our point. Fisher *et al.* made measurements in June 1999 and February 2003, which, given the spacing between these two dates, can be interpreted as two measurements separated by 44 months ($T = 1320$ days), each averaged over roughly one month ($t_0 = 30$ days). Therefore, the experiment should perceive a change in the value of the field equal to:

$$\delta\phi(\varphi_0) = \frac{\phi_0}{t_0}\left(\int_{t=0}^{t=T} dt\cos\left[M(t+T)/h + \varphi_0\right] - \int_{t=0}^{t=t_0} dt\cos\left[Mt/h + \varphi_0\right]\right), \tag{2.31}$$

where φ_0 is an unknown phase of the field. Performing the integral and factorizing gives us:

$$\delta\phi(\varphi_0) = \frac{4\phi_0}{Mt_0}\ \sin\left(\frac{MT}{2}\right)\sin\left(\frac{Mt_0}{2}\right)\sin\left(\varphi_0 + \frac{M(t_0+T)}{2}\right). \tag{2.32}$$

This means that for certain fine-tuned phases $\varphi_0 \sim -M(t_0+T)/2$ the experiment could see nothing by simply being unlucky. However, we know that 95% of time $|\sin(\varphi_0 + M(t_0+T)/2)| \geq \sin(0.05/4 \times 2\pi) = 0.0785$ and so 95% of time $\delta\phi$ is larger than:

$$|\delta\phi| \geq \left| \frac{4\phi_0}{Mt_0} \sin\left(\frac{MT}{2}\right) \sin\left(\frac{Mt_0}{2}\right) \sin\left(\frac{5\pi}{200}\right) \right|. \tag{2.33}$$

We use this expression to put a 95% confidence bound on χ and plot it as α-drift in figure 2.7. Note that in the event that the sampling frequency of the experiment is a harmonic of the the oscillation frequency of the field, the experiment will also become insensitive to such a drift. This would show up as an oscillatory behavior in the bound on χ and we have replaced the region where these oscillations become too narrow to display with a dashed line in figure 2.7.

We would like to conclude the analysis of the fine structure constant drift bounds with two notes. First, as the Cesium contribution dominates and the exact interaction of different atomic levels in Cesium is beyond the scope of this paper, we would like to shelve this bound as tentative and in need of focused treatment. Second, presence of Dark Matter in the form of Dark Photon only mimics a drift in α and could be potentially resolved from an actual drift if one were to measure different energy splittings that depend on different powers of α.

Adiabatic Conversion

In the flavor basis, the Dark Photon and ordinary photon mix through the off-diagonal mass terms. In a thermal environment the mass matrix takes the form:

$$\mathcal{M}^2 = \frac{1}{2} \begin{pmatrix} m_\gamma(x)^2 + \mathcal{O}(\chi^2) & -\chi M^2 \\ -\chi M^2 & M^2 + \mathcal{O}(\chi^2) \end{pmatrix}, \tag{2.34}$$

where $m_\gamma^2(x,t) = e^2 n_e(x,t)/m_e$ is the plasma mass, which may depend on time or position. Should the plasma mass be slowly varying then there could be an adiabatic conversion between different states. Mirizzi *et al.* explore this effect in the context of changing electron density in the Universe as it expands and distorts the Cosmic Microwave Background through an excess of converted Dark Photons [39], and they offer a very useful comparison of this process to the neutrino Mikheyev-Smirnov-Wolfenstein effect. We observe that this

process could be much more severe in the environment of ionized gas that forms a significant portion of typical clusters of galaxies.

Figure 2.6 shows the energy of an eigenstate of the mass matrix as a function of radial distance of a particle from the center of the cluster. As an example we will follow a Dark Photon that is infalling into a cluster. If the Dark Photon infalls adiabatically it stays in the same eigenstate of the mass operator which contains more of the original photon state after it crosses the point where $m_\gamma \sim M$. Therefore, the Dark Photon is converted into an ordinary photon that thermalizes very quickly (the cluster gas temperatures are in the range $10^6 - 10^7$ K, [40]). Photons generate pressure and as a result the cluster loses the gravitational glue holding it together. Since we do observe clusters of ionized gas, it is imperative that the section of parameter space be excluded.

How slow is adiabatic? In order to cross from one level to another we require that the characteristic time associated with the change in the system needs to be on the order of the gap between the energy levels. We can compute the rate of change of the photon plasma mass at the point where the energy gap is minimal to get:

$$t^{-1}|_{m_\gamma(x)=M} = \frac{1}{m_\gamma(x)}\frac{dm_\gamma(x)}{dt}\bigg|_{m_\gamma(x)=M} = \frac{v}{m_\gamma(x)}\frac{dm_\gamma(x)}{dx}\bigg|_{m_\gamma(x)=M} = \frac{v}{2}\frac{n'(x)}{n(x)}\bigg|_{m_\gamma(x)=M}. \tag{2.35}$$

On the other hand, the mass gap between the states is minimal when $M = m_\gamma$, which turns out to be:

$$\Delta E|_{M=m_\gamma} = \chi M. \tag{2.36}$$

We take a free electron density curve from [41], replotted in figure 2.6, to determine the portion of (χ, M) parameter space in which this infall turns out to be adiabatic, taking the velocity of infall to be the escape velocity $v(r) = \sqrt{GM_c/r}$. We note that this mechanism will only work for a mass range of 10^{-13} eV - 10^{-11} eV, with the lower limit coming from the density of voids and the upper from the highest densities inside clusters. We have plotted the resulting region in figure 2.7 and marked it AdC.

Breaking Lorentz Invariance

The existence of Dark Matter necessarily causes apparent Lorentz violation because it defines a preferred frame – its own rest frame. The effects of this frame can be measured through its coupling to the Standard Model particles. However, even if those couplings were zero the gravitational interaction would remain. Even in the Dark Matter rest frame there is additional Lorentz violation due to the polarization of the Dark Photon.

Moreover, we can see the gravitational violation of Lorentz symmetry by looking at the stress-energy tensor. Assuming the polarization points in the z-direction $A_i = \delta_{i3} A \cos(Mt)$, we get:

$$T_{\mu\nu} = \frac{M^2 A^2}{2} \begin{pmatrix} -1 & & & \\ & \cos(2Mt) & & \\ & & \cos(2Mt) & \\ & & & -\cos(2Mt) \end{pmatrix}. \tag{2.37}$$

The time average of $T_{\mu\nu}$ corresponds to pressureless dust, just as we concluded from equation 2.14. Moreover, at late times the frequency of oscillations is shorter than the expansion rate of the Universe. The field begins to oscillate when $M \sim H$, at this time the oscillations cannot be averaged over a period and the Dark Matter contribution to the Stress-Energy tensor is not rotationally invariant. However, at that early time radiation dominates the energy density of the Universe and Dark Matter is a minor perturbation, therefore the lack of rotational symmetry of $T_{\mu\nu}$ does not produce any significant effect.

2.2.5 Summary

A nonrelativistic condensate of light vector particles could be produced during Inflation and is a viable candidate for the Dark Matter component of the Universe. For ultralight vector particles, a small kinetic mixing term with the photon could allow this particle to be detectable. After considering the constraints on the mixing parameter from cosmology and astrophysics, we find that there are some regions of parameter space that could give unusual laboratory signatures of Dark Matter, such as apparent time dependent shifts in electromagnetic properties of matter and Dark Matter conversion to visible photons in

plasmas. It is peculiar that although Dark Photon picks a unique direction in the Universe, it lacks a mechanism to imprint this direction onto the Standard Model contents of our Universe. This model offers a unique experimental signature: weak background electric and magnetic fields that cannot be screened.

Appendix

Equations of Motion in the Early Universe

The kinetic term in the Lagrangian for a massive vector $\mathcal{L} = \phi^{\mu\nu}\phi_{\mu\nu}/4 + M^2\phi^\mu\phi_\mu/2$, can be simplified to:

$$\begin{aligned}
\frac{1}{4}\phi_{\mu\nu}\phi^{\mu\nu} &= \frac{1}{4}(\partial_\mu\phi_\nu - \partial_\nu\phi_\mu)(\partial^\mu\phi^\nu - \partial^\nu\phi^\mu) \\
&= \frac{1}{2}(\partial_\mu\phi_\nu\partial^\mu\phi^\nu - \partial_\mu\phi_\nu\partial^\nu A^\mu) \\
&= \frac{1}{2}(\partial^\alpha\phi^\beta)(\partial^\gamma A^\delta)(g_{\alpha\gamma}g_{\beta\delta} - g_{\alpha\delta}g_{\beta\gamma}) \\
\frac{\delta\mathcal{L}}{\delta(\partial^\alpha\phi^\beta)} &= (\partial^\gamma\phi^\delta)(g_{\alpha\gamma}g_{\beta\delta} - g_{\alpha\delta}g_{\beta\gamma}) = \phi_{\alpha\beta}.
\end{aligned}$$

Therefore, the equation of motion in curved space reads:

$$\partial^\alpha(\sqrt{-g}\phi_{\alpha\beta}) = M^2\phi_\beta\sqrt{-g}. \tag{2.38}$$

Where in FRW metric this means:

$$\begin{aligned}
-\partial_0 a^3(t)\phi_{0\beta} + a^3(t)\partial_i\phi_{i\beta} &= a^3(t)M^2\phi_\beta \\
-3\dot{a}a^2\phi_{0\beta} - a^3(t)\partial_0\phi_{0\beta} + a^3(t)\partial_i\phi_{i\beta} &= a^3(t)M^2\phi_\beta \\
-a^3(t)\left(\partial_0\phi_{0\beta} + 3\dot{a}/a\phi_{0\beta} - a^2(t)\partial_i\phi_{i\beta} + M^2\phi_\beta\right) &= 0.
\end{aligned} \tag{2.39}$$

Keeping in mind that for our candidate $\partial_i\phi_\alpha = 0$ in the cosmic frame, $a(t) \neq 0$ after or during Inflation and $\dot{a}/a = H$, the last line turns into:

$$\begin{aligned}
\partial_0\phi_{0\beta} + 3H\phi_{0\beta} + M^2\phi_\beta &= 0 \\
\partial_0(\partial_0\phi_\beta - \partial_\beta\phi_0) + 3H(\partial_0\phi_\beta - \partial_\beta\phi_0) + M^2\phi_\beta &= 0.
\end{aligned} \tag{2.40}$$

Therefore, the time component $\beta = 0$ gives us:

$$\partial_0(\partial_0\phi_0 - \partial_0\phi_0) + 3H(\partial_0\phi_0 - \partial_0\phi_0) + M^2\phi_0 = 0$$
$$M^2\phi_0 = 0. \tag{2.41}$$

On the other hand, the spatial component $\beta = i$ implies the equation for a Hubble-damped harmonic oscillator:

$$\partial_0(\partial_0\phi_i - \partial_i\phi_0) + 3H(\partial_0\phi_i - \partial_i\phi_0) + M^2\phi_i = 0$$
$$\partial_0\partial_0\phi_i + 3H\partial_0\phi_i + M^2\phi_i = 0. \tag{2.42}$$

Compton Evaporation Matrix Elements

For reference we have evaluated the matrix elements for the Compton Evaporation. The momenta were assigned as follows:

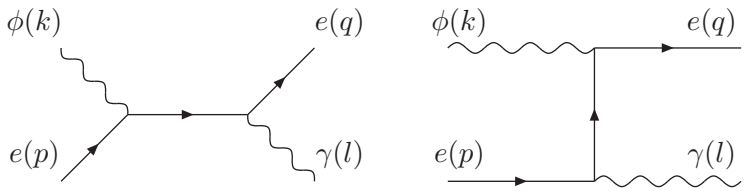

a) the s-channel b) the u-channel

With this convention the matrix element becomes:

$$iT = \chi e^2 \epsilon^*_\mu(l)\epsilon_\beta(k)\bar{u}(q)\left(i\gamma^\mu \frac{-i(m - \not{p} - \not{k})}{(p+k)^2 + m^2} i\gamma^\beta + i\gamma^\beta \frac{-i(m - \not{p} + \not{l})}{(p-l)^2 + m^2} i\gamma^\mu\right) u(p)$$

Which implies that:

$$\langle|T|^2\rangle = \frac{64\pi^2\chi^2\alpha^2}{3}\left(2\frac{(m^2+M^2)(4m^2-t) - 3m^2M^2}{(m^2-u)(m^2-s)} + \right.$$
$$\left. + \frac{m^4 + 2m^2M^2 + m^2(3s+u) - us}{(m^2-s)^2} + \frac{m^4 + 2m^2M^2 + m^2(3u+s) - us}{(m^2-u)^2}\right)$$

Which agrees, up to a number of degrees factor, with regular Compton Scattering in the limit $M \to 0$, $\chi = 1$.

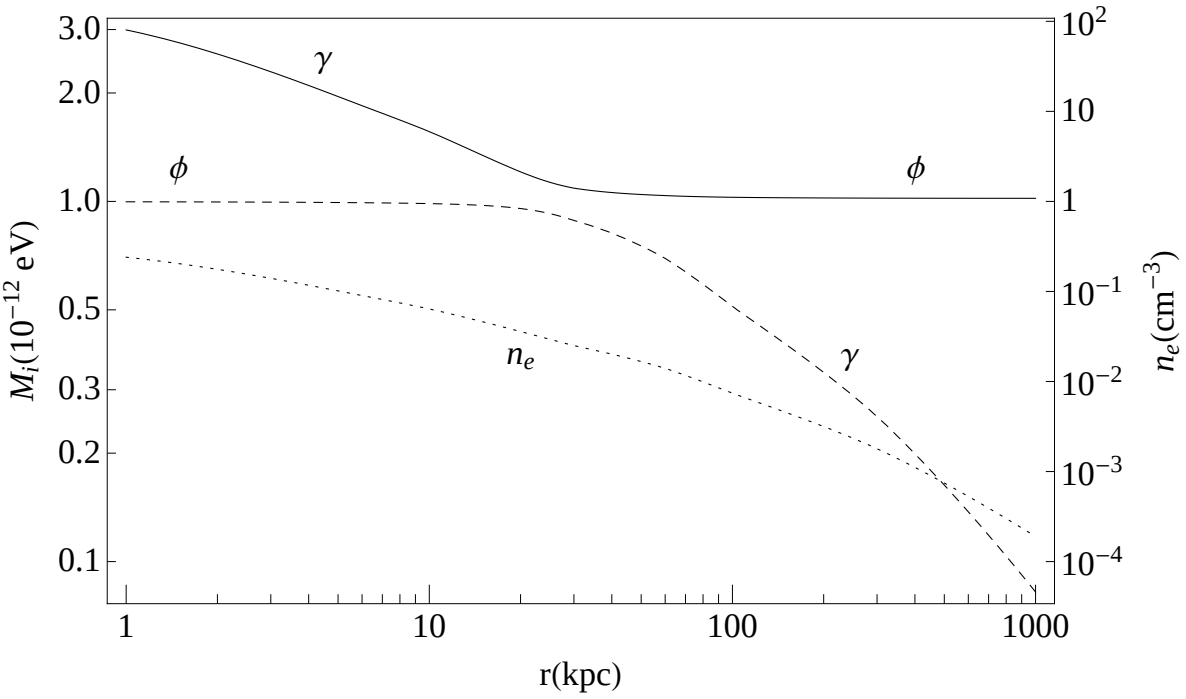

Figure 2.6: Mass mixing in plasma: The solid and dashed curves show the eigenvalues of the mass matrix as a function of the radial position inside the cluster. The dotted line shows the density of the ionized gas in the cluster also as a function of the radial position. In order to make the level crossing visible we have adopted $M = 10^{-12}$ eV and $\chi = 0.2$.

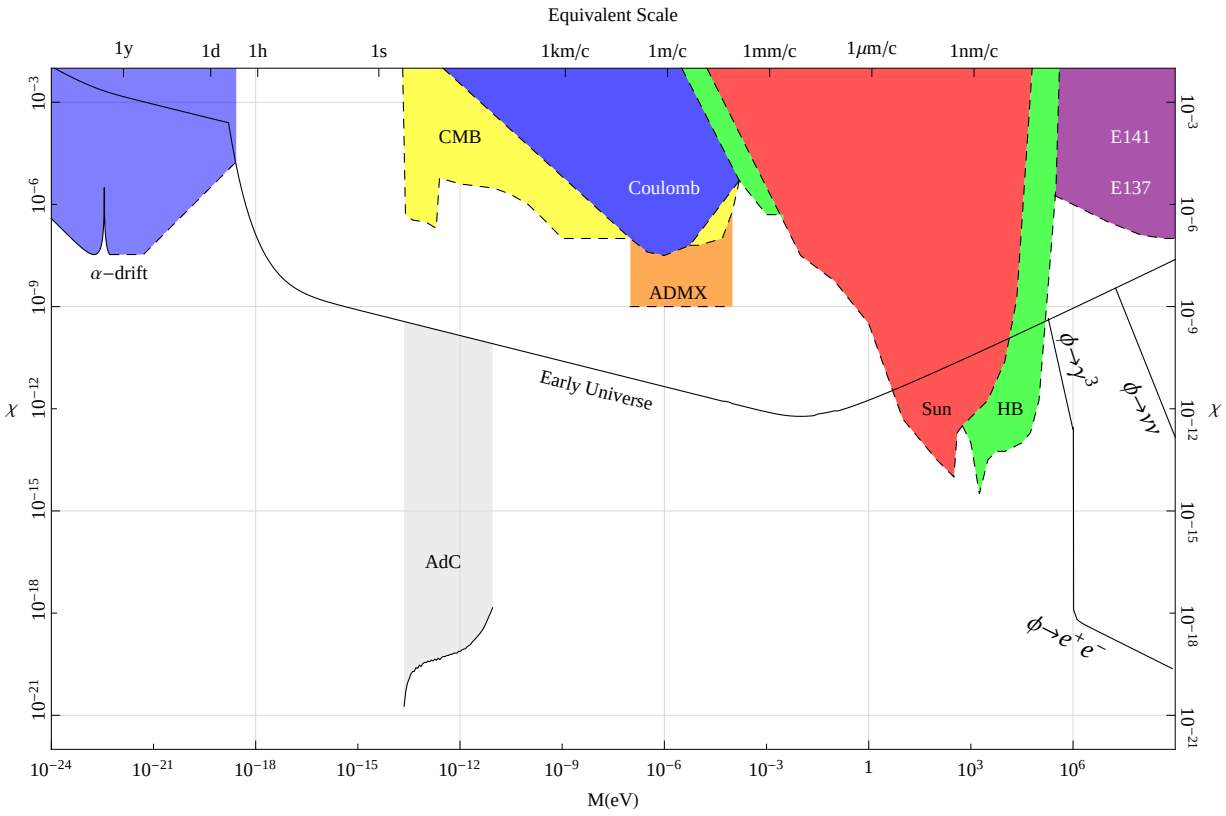

Figure 2.7: Summary of Constraints: The early Universe behavior puts a dominant bound on χ in the higher mass range, for $M > 2m_e$ the bounds are dominated by decays. The Shaded region called AdC marks the possible combinations of (χ, M) that could lead to adiabatic conversions. We have marked out the projection of the limits that can be achieved by ADMX [42](Orange) – axion search experiment turned into a light shining through the wall experiment. The bounds put by shaded regions with dotted lines come from a summary by [17] and comprise the bounds by both theoretical and experimental considerations such as lifetime of the Sun (Red), Horizontal Branch Star limits (Green), Coulomb law tests (Blue), CMB pollution by the Dark Photon (Yellow) and beam dump experiments E141 and E137 (Purple). In the low mass region the dominant bound comes from the drift of the fine structure constant (Blue, solid/dashed).

2.3 Future Directions

There are several directions that warrant additional research. The Adiabatic Conversion from section 2.2.4 presents a very strong constraint on the kinetic mixing parameter χ over a range of two orders of magnitude in mass. However, the density distribution of the hot gas inside a galaxy cluster is not necessarily smooth. The local fluctuations in this density may violate the required adiabaticity condition. The degree of this violation is not clear because the de Broglie wavelength of the Dark Photon approaches 1 lightsecond and thus the Dark Photon may be unable to resolve these local fluctuations. Therefore a more detailed study of this effect would be welcome.

The apparent drift in the fine structure constant from section 2.2.4 is a promising way to probe the kinetic mixing for the lightest Dark Photon when all other methods become insensitive. However, it requires a more detailed study of the exact structure of the Cesium atom beyond the simplified view we have taken in our work. Moreover, it would be useful to identify a set of measurements and their combinations such that we can remove the degeneracy between real drift in the fine structure constant and variations caused by the Dark Photon. Results of such a project would be helpful to our experimental colleagues.

Chapter 3

HIGH ENERGY FRONTIER: PHOTON JETS AT LHC

3.1 Introduction

In this project we consider a Hidden Sector with two scalars n_1, n_2 such that we can produce a cascade decay of the Higgs particle: $h \to 2n_1 \to (n_1 \to 2n_2)(n_1 \to 2n_2) = 4n_2 \to 8\gamma$. If n_1 and n_2 are light compared to the mass of the Higgs, we can produce an an interesting signal. In the rest frame of the Higgs, the two n_1s come out back to back. When the n_1s decay into pairs of n_2s, the angle between the n_2s is roughly $\Delta\theta \sim 2m_1/p_1$, where m_1 is mass of n_1 and $p_1 \sim m_h/2$ is the momentum of n_1. As long as m_1/m_h is small, the two n_2s are nearly collinear with the direction of their parent n_1. For the same reason, when the n_2s decay further into photons, the angle between the photons is roughly $2m_2/m_h$. As a result, we get two back-to-back beams of four collimated photons as illustrated in figure 3.1. We call these collimated beams of photons Photon Jets. This type of signal requires a

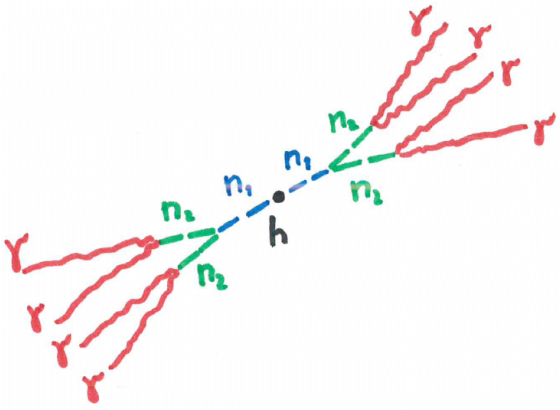

Figure 3.1: We arrange a peculiar decay chain for the Higgs boson.

more complicated analysis; in order to understand the complications, the reader needs to

be familiar with Collider Physics. A reader knowledgeable in both Collider Physics and Jet Substructure should feel free to jump straight to section 3.5. Everyone else is encouraged to read the next three sections.

3.2 Colliders

Colliders are machines designed to probe high energy processes and discover new massive particles. In order to be able to do so, our experimental colleagues create beams of particles and cross these beams to cause collisions where individual particles come into the center of mass frame with a large amount of available kinetic energy. If the two incoming particle have four-momenta p_1 and p_2, the center of mass frame has energy $\sqrt{s} = \sqrt{(p_1 + p_2)^2}$, which represents the upper bound on the mass of a particle that can be created in this collision. Fixed target machines are still used, however although colliding two beams is technologically harder, it allows for higher $\sqrt{s}$. At the time of this thesis the Large Hadron Collider (LHC) is the leading high energy proton-proton facility. It operates with two proton beams at $\sqrt{s} = 8$ TeV and will soon be upgraded to $13 - 14$ TeV.

3.2.1 Coordinates

The symmetries of the beam setup influence the coordinate system we use to describe all the physical quantities. The beam axis is the z-axis and p_z is the component of momentum along this axis. The plane defined by the x and y-axes is called the transverse plane. Parameterizing the transverse plane in polar coordinates gives us the azimuthal angle ϕ and the magnitude of momentum in this plane is called p_T. Note that $p_T^2 + p_z^2 = p_x^2 + p_y^2 + p_z^2 = |p|^2$. Instead of defining another angular variable such that $p_z = |p| \cos\theta$ and $p_T = |p| \sin\theta$, we use pseudorapidity η defined by $p_z = p_T \sinh\eta$. As the name suggests pseudorapidity η and rapidity $y = \tanh^{-1}(|p|/E)$ are related: when a particle is massless (or highly relativistic), these two variables coincide. We use η because it is mass independent and the collider environment is relativistic enough that it makes a good approximation to y. As opposed to rapidity y, pseudorapidity η is in one-to-one correspondence with the previously defined angle θ:

$$\eta = -\log\tan(\theta/2) \tag{3.1}$$

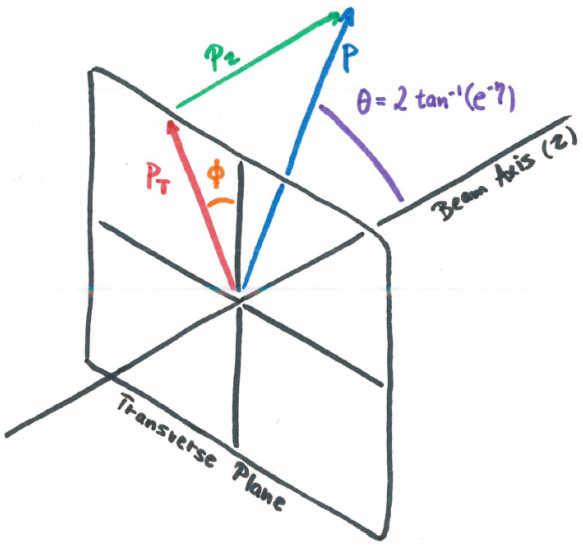

Figure 3.2: Coordinates used in Collider Physics

We use η instead of θ, because it turns out that for many processes the cross-section is nearly constant in η and so it is a good spatial coordinate. Moreover, differences of pseudorapidities between two particles are invariant under boosts in the z-direction. We will see in the next section this is useful in hadron colliders. Figure 3.2 illustrates the entire coordinate system.

3.2.2 Hadron Colliders

There are two ways to accelerate particles to large momentum. With a linear accelerator it can be done in one shot. A longer accelerator allows for a higher accessible $\sqrt{s}$ and costs more. The acceleration can also be achieved by bending the linear accelerator into a ring and passing the particle many times around this ring. However, keeping charged particles on a circular orbit leads to energy losses through synchrotron radiation. The power radiated by a relativistic particle of energy E on a circular orbit of radius R due is given by Jackson in [43]:

$$P = \frac{2}{3}\frac{q^2 c}{R^2}\beta^4\gamma^4 \sim \frac{1}{R^2}\left(\frac{E}{m}\right)^4 \tag{3.2}$$

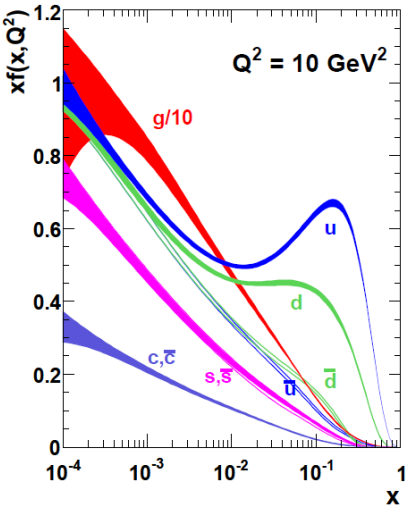

Figure 3.3: Parton Distribution Functions for $Q^2 = 10$ GeV^2 as extracted by the MSTW group [44] with their 1σ uncertainty bands.

As a result, electron beams radiate significantly more than muon or proton beams. Since the amount of power available to an accelerator is limited by financial as well as social considerations[1] the peak beam energy achievable is then lower for electrons. The proton-proton and proton-anti-proton colliders are the reality of our era. Because of the $1/R^2$ dependence, it is also advantageous to build rings as large as the available initial investments allow. Moreover, the bending power of magnets used to keep the beam circular is also a limiting factor that influences the size of the collider.

When two electrons with momenta p_1 and p_2 scatter, the center of mass energy is $\sqrt{s} = \sqrt{(p_1 + p_2)^2}$. However, when two protons participate in an inelastic collision they do not interact as a whole: their quarks, anti-quarks and gluons (called partons) interact with each other. A parton rarely carries all of the momentum of the original proton. We call the fraction of the energy carried by a parton x and its probability distribution is called the Parton Distribution Function (PDF). These are measured at some scale and then extrapolated across all scales. One example of PDFs are plotted in figure 3.3.

[1]For example, the local grid has to have sufficient capacity to power the accelerator.

Since the two colliding partons do not necessarily share the same x, their center of mass is moving in the detector frame. This motion is only significant along the beam axis since the momentum in the transverse plane is not boosted and thus on the order of $\Lambda_{QCD} \lesssim 1$ GeV. In order to remove dependence on this unknown boost we can use variables that are invariant under boosts in the beam direction.

3.2.3 The Detector

Just colliding the beams is not enough. We need to record the particles that come out of the collision in order to reconstruct the collision event and extract meaningful physical information. The recording is done by instrumentation collectively called a detector. Modern detector designs are dominated by the so-called "4π" coverage, meaning the detector completely surrounds the beam interaction point (IP) except for the two directions from which the beams enter the detector. The two all purpose detectors designed for LHC are called ATLAS and CMS. Although one may argue that their design philosophies differ, the general scheme for both detectors is remarkably similar. Since the University of Washington Elementary Particle Experiment Group is part of the ATLAS collaboration, I am more familiar with the ATLAS detector and I will proceed to base my description of a particle detector on the ATLAS model as described in [45] and shown in figure 3.4.

I will describe the elements of the detector in the same order in which a particle traveling from the interaction point encounters them. The typical trajectory of a particle inside a detector can be seen in figure 3.5. Before introducing the detector subsystems I would like to mention that some of the detector subsystems contain a magnetic field to the beam axis. This way a trajectory of a charged particle is bent. The radius of curvature of this track is inversely proportional to the particle momentum divided by its charge. Therefore, we can learn about the sign of its charge and assuming it is not an exotic particle also its momentum.

The first section a particle encounters in the detector is the tracker. The tracker is made out of materials that can detect a charged particle passing through with minimal influence on the trajectory of the particle. The first two parts of the ATLAS tracker consist of

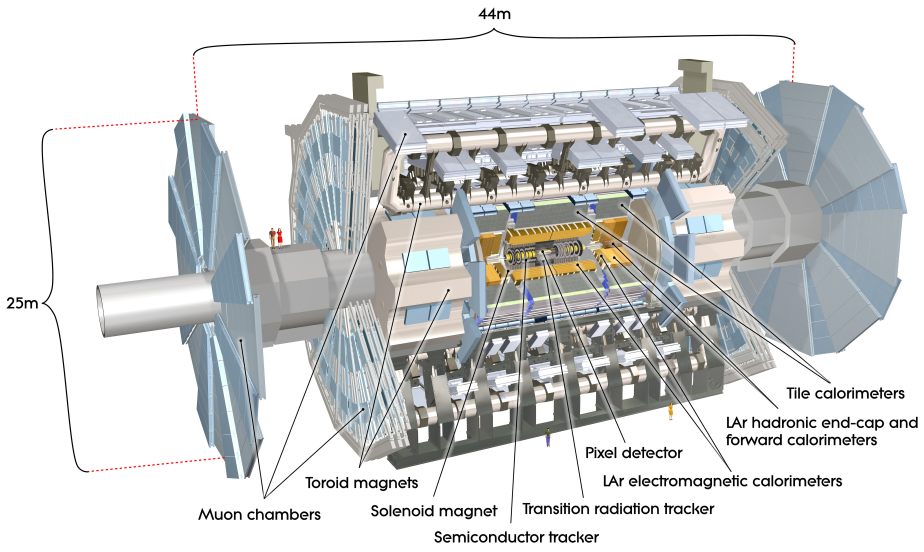

Figure 3.4: ATLAS detector [46]

silicon strips and pixels and work like Charged Coupled Devices (CCD) in digital cameras. As a charged particle passes through silicon layers, it is likely to ionize the silicon in its vicinity triggering a current in the device. The third part of the tracker consists of tubes filled with gas that gets ionized by passing charged particles. The ions are then collected on a biased electrode running through the middle of the tube. From the timing of the ions one can deduce the position of the ionization inside the tube and locate where the track intersects the tube. This way, each layer of the tracker can recover a point along the particle trajectory. Recovering several points along one trajectory then allows us to reconstruct this track. An average event may contain many tracks that intersect, and it is important to appreciate that the track density is very large and track reconstruction presents a very complex pattern recognition problem. Yet, tracking provides incredibly valuable information, without which many physics analyses would be greatly compromised.

Once a particle leaves the tracker, it enters the two calorimeters. Whereas the tracker is designed to have as little interaction with the particle as possible in order to measure its

position and momentum, the two calorimeters are designed measure the particle's energy by absorbing all of it. In order to obtain some directional information, the calorimeter is segmented into a grid of cells in the $\eta - \phi$ directions. Different layers of the calorimeters may be segmented coarsely or finely. However, keep in mind that a single particle generally interacts with more than one calorimeter cell and multiple particles may interact with the same calorimeter cell. For example, a single photon will deposit energy in several calorimeter cells because as it passes through the calorimeter it creates a cascade of additional photons and electron-positron pairs. The first part of the calorimeter, the Electromagnetic Calorimeter (ECal), is designed to absorb particles that interact electromagnetically, such as photons and electrons. The second part, the Hadronic Calorimeter (HCal), is designed to contain all the energy of the particles that interact mainly through the strong interaction. Of course, this separation is not perfect. For example, charged pions radiate part of their energy in the ECal, and charged pions with low momentum may even loose most of their energy in the ECal. On the other hand, some hard (energetic) photons may "punch through" into the Hadronic Calorimeter. The output of the calorimeter is often presented as a "lego plot", showing the energy depositions in the $\eta - \phi$ plane (for example, figure 3.7).

Not every particle is fully absorbed in the calorimeters. Muons have a very small charge-to-mass ratio, which means that their radiation losses are relatively small. They also do not interact through the strong interaction. As a result, muons deposit very little energy in both calorimeters as they pass through them. This may seem problematic, but instead it is a blessing: their peculiar nature not only makes them easy to identify, but also motivates the next stage of the detector. The outer layer of the detector is the muon spectrometer, a specialized muon tracker designed to measure the muons' three-momentum thus extracting all the available information. In the ATLAS detector the magnetic field in the muon spectrometer is in the r-z plane and helps to measure determine the muon momentum. This entire process is well summarized in figure 3.5.

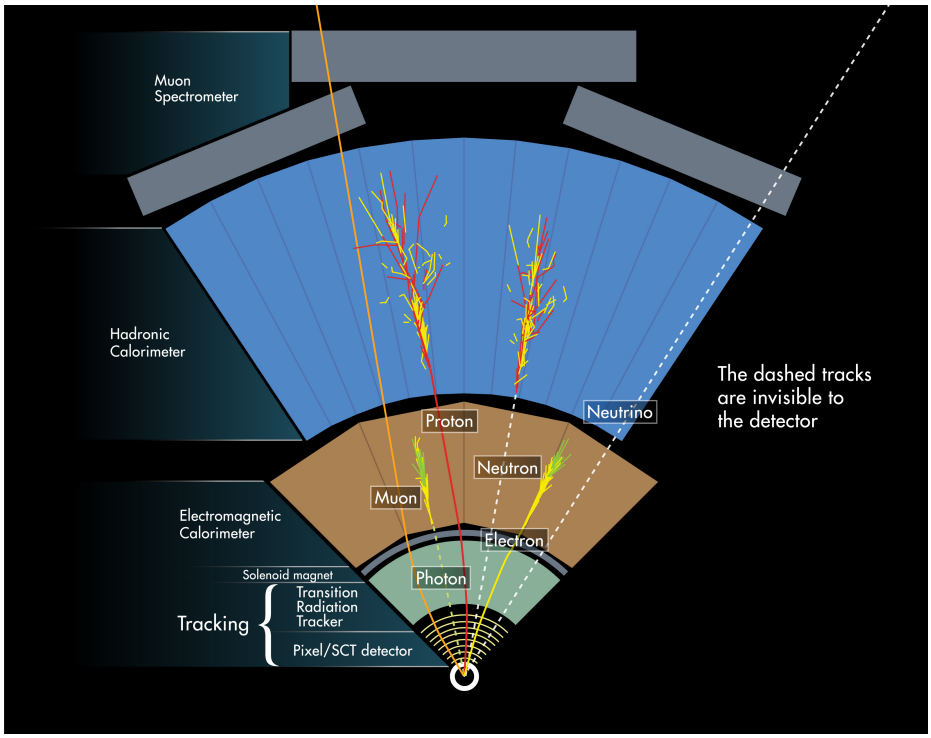

Figure 3.5: ATLAS detector subsystems [46] and their interaction with particles.

3.2.4 Event Reconstruction

Once an event is recorded it needs to be reconstructed. Tracker hits are reconstructed into tracks. Calorimeter cells are combined into clusters. Muon spectrometer hits are reconstructed as candidate muons. These proto-objects are then analyzed in different ways to extract candidate photons, electrons, muons and jets (I will write more about jets in the next section). First, we show a simplified example of how particles may be identified. Every candidate ECal cluster (a set of nearby ECal cells with energy deposits) is a candidate electron or candidate photon. In order to reduce the probability a photon is mis-identified as an electron and vice versa, all candidates without a reconstructed charged track in their direction are candidate photons and those with a reconstructed track become candidate electrons. Since photons are not expected to leak too much into HCal, any candidate photon with too much energy deposited in the HCal in the same direction as the candidate photon are discarded (this is called the HCal isolation criterion).

Of course, this does not mean all that is left is a collection of photons. Some electrons tracks may not be reconstructed and thus appear as photons. Some photons may interact with the matter of the detector and convert into an electron-positron pair. These converted photons leave behind tracks and need extra attention. Neutral pions decay into pairs of photons which, unless resolved, appear as a single photon and pollute the sample. Luckily neutral pions usually come together with another nearby hadron and therefore fail the H-cal isolation criterion. This shows that a considerable amount of effort needs to be devoted to accurately reconstructing each particle and event. A good starting point to read more about event reconstruction can be found in [47].

3.2.5 Signal and Background

Once we obtain a set of reconstructed events we can start doing physics analyses, such as determining the production cross-section of the Higgs particle or measuring the mass of the top quark. These are essentially counting experiments: we define the kind of event we seek, the signal, and count how often it happens. Unfortunately, there are other events that look identical, similar or can be misreconstructed to look like signal. These are the background.

The art lies in devising sets of discriminants that reduce the background and not the signal so that the signal-over-noise ratio improves[2].

Now, you should be able to see why a set of four collimated photons may cause trouble. A single photon, unless converted, leaves no tracks and then hits several calorimeter cells. Four collimated photons may also leave no tracks. If they are collimated enough, they could hit almost the same number of calorimeter cells.

Why does it matter? It matters because whereas $h \to 2\gamma$ is a standard (albeit very important) decay channel for the Higgs boson, $h \to 8\gamma$ would be significant evidence of New Physics. In terms of the previous paragraphs, if the Higgs decay into two photons is our signal, then photon-jets are a background and vice versa. Are there discriminants that can help us tell them apart? Luckily there is a large array of tools to analyze complex energy depositions in the calorimeter – they are all associated with jets.

3.3 Jets and Substructure

3.3.1 Jets

Suppose I wanted to study $e^+e^- \to \mu^+\mu^-$ scattering. The best I could do is to build a e^+e^- collider and look for muons in the detector. The differential cross-section can be easily computed. The next-to-leading order correction comes from interference between the tree-level and the one-loop diagrams, as shown on the left hand side of figure 3.3.1:

The loop diagram has both Infrared (IR) and Ultraviolet (UV) logarithmic divergence. This divergence has the opposite sign, but the same form that we would encounter if we were to compute the cross-section for $e^+e^- \to \mu^+\mu^-\gamma$. The sum of these two contributions (of the same order in α) would be finite. For a detailed treatment of this issue I would heartily encourage the reader to carefully go through Peskin and Schroeder (Chapters 6 and 17). It seems strange that cross-sections for two different final state processes are formally infinite,

[2]The noise is proportional to the square root of the expected background count. Since the background events represent a random process with average rate b, the actual number of background events has a variance $\sqrt{b}$. Since we cannot know the exact number of recorded background events (only its average value) we can only subtract the average value and the variance represents the average amount of unremovable background we need to find the signal in – this is why the noise is proportional to the square root of the expected background count.

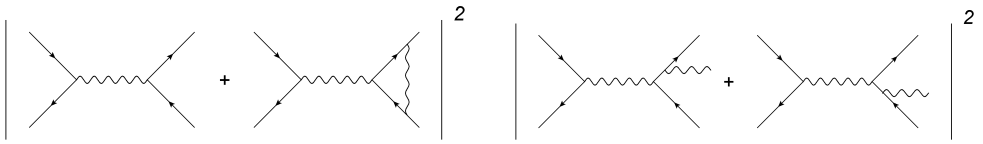

Figure 3.6: Interference between two diagrams on the left is naively the only contribution to the first order correction to $e^+e^- \to \mu^+\mu^-$. However, the processes represented by diagrams on the right may be physically indistinguishable from $e^+e^- \to \mu^+\mu^-$, so we must include them as well.

yet their sum is finite. But these two processes are not different at all: $e^+e^- \to \mu^+\mu^-\gamma$ diverges precisely when the radiated photon becomes infinitely soft or collinear with one of the muons, which is when we cannot resolve it with our detector. Since we cannot see the difference it becomes part of the $e^+e^- \to \mu^+\mu^-$ process. The infinities arose because we were trying to split the physical measurement between two parts we could not physically distinguish. In reality we cannot distinguish a muon and a muon with a perfectly collinear or soft photon – both of these are part of what we call a physical muon.

We could have handled this differently. We could have estimated the softest or most collinear photon our detectors would be able to detect and resolve. Then we would use these parameters as IR cut-offs to our integrals, carrying corrections terms of order $(\alpha \log(E_{min}/m_\mu))^n$ and $(\alpha \log(\theta_{min}E_{min}/m_\mu))^n$ for n radiated photons. The logarithms of very small E_{min}/m_μ or $\theta_{min}E_{min}/m_\mu$ can be large. Unless α is small enough, the perturbative series obtained from considering one or more radiated photons is only asymptotic and may not be well behaved. In QED, α is small, and we do not encounter problems. But if the final states are colored the QCD corrections from radiated gluons come with α_s and are not necessarily small. Then it is better to think in terms of inclusive measurements such as $\sigma(e^+e^- \to \bar{q}q) + \sigma(e^+e^- \to \bar{q}qg) + \sigma(e^+e^- \to \bar{q}qgg) + \ldots$ that remove these logarithms entirely. Therefore, if we want to avoid these potentially large logarithmic corrections we need to design variables, procedures and objects that avoid IR and collinear singularities – this notion is called IR safety.

There is another difficulty with QCD: quarks and gluons are not good final states. An isolated quark may be a reasonable state to think about at scales much higher than 1 GeV $\sim$ (fm)$^{-1}$, when the strong coupling constant α_s is small. But once the $\bar{q}q$ pair splits any farther, quarks fail to be the appropriate degrees of freedom and we need to describe the physics in terms of hadrons.

The process of transitioning between colored quark and gluon states and color-singlet state, or hadrons, is called hadronization. Although we cannot predict how a particular event hadronizes from first principles, we can still make predictions. It turns out that one can factorize the high-energy perturbative processes and the non-perturbative low energy processes such as hadronization. Moreover, IR safe variables and objects are fairly insensitive to hadronization. This discovery allowed us to make predictions in perturbative QCD and relate the energy flow of the perturbative process to the pattern of energy depositions in the calorimeter. In order to relate these two concepts a new object has been created: the jet.

A jet is a result of applying a jet-algorithm to a collection of four-vectors. Currently, the jet community uses several jet-algorithms. Modern, recombination, jet-algorithms work in a similar fashion. Each jet-algorithm is associated with a particular metric d_{ij} that determines distance between two four-vectors v_i, v_j. As already mentioned, we start with a set of four-vectors and a preset parameter R. The algorithm proceeds to merge the closest pair of four-vectors in the set by replacing the pair with their sum, until all the pairwise distances d_{ij} are larger than R. Every four-vector that is left after this clustering is a jet. All the four-vectors that were merged into a jet are its constituents.

You can see how a jet-algorithm would be applied to the calorimeter output: each cell with energy deposit E can be turned into a light-like four-vector in the direction of the cell from the IP, with the time component equal to E. These four-vectors can then be clustered in order to identify the jets in the calorimeter. In reality calorimeter cells are first grouped into bigger clusters whose four-vectors form the initial set.

On the theory side, using the $e^+e^- \to \bar{q}qg$ calculation we can compute the probability that two of the three "final state particles" will end up within a distance less than R away from each other, forming two jets instead of three. This shows why jets are IR-safe objects.

All the IR and collinear divergences are treated inclusively: an infinitely soft gluon may not be captured inside the jet that contains the quark that radiated this gluon, but the missing infinitely soft momentum does not influence this or any other jet in this event. Similarly, assuming the distance metric is reasonable, an arbitrary number of gluons that are radiated along the quark still end up in the same jet.

There are three metrics in use. They all have a similar form: $d_{ij} = \min(p_{Ti}, p_{Tj})^{2p} \Delta R^2$, where p_{Ti} is the transverse momentum of p_i^μ and $\Delta R^2 = (\eta_i - \eta_j)^2 + (\phi_i - \phi_j)^2$ is the distance between the two vectors in η, ϕ plane. The k_T-algorithm [48] uses $p = 1$, the Cambridge/Aachen algorithm [49] uses $p = 0$ and the anti-k_T algorithm [50] uses $p = -1$. Each algorithm has its own uses. In a general environment, the k_T-algorithm merges particles that were most likely radiated by each other because d_{ij} is small for soft and collinear particles. Therefore, it simulates the reverse shower process of QCD well. However, the edges of such a jet tend to be very irregular as soft particles get pulled into the jet first. On the other hand, the anti-k_T algorithm tends to build clean, circular jets. When two jets are close to each other the higher p_T jet "takes a bite" out of its less fortunate neighbor. The anti-k_T jets may not be faithful interpretations of their QCD past, but they are significantly easier to calibrate by our experimental colleagues. The C/A algorithm is always somewhere in between k_T and anti-k_T and its shower reconstruction is purely geometric. Figure 3.7 illustrates well how different jet-algorithms produce different jets.

I would like to stress a certain point: many physicists from outside of the jet-physics community tend to build an "organic" understanding of jets. They assume that each (hard) parton initiates a jet. This concept is called the parton-jet duality. And it is wrong. First, this is not an IR-safe statement. Unless a hard collinear gluon radiated from a quark is treated as part of the same jet we run afoul of the collinear divergence. In order to avoid problems of this kind we use jet-algorithms. Jets are products of jet-algorithms. Therefore, if I were to change my jet-algorithm I would get different and possibly a different number of jets.

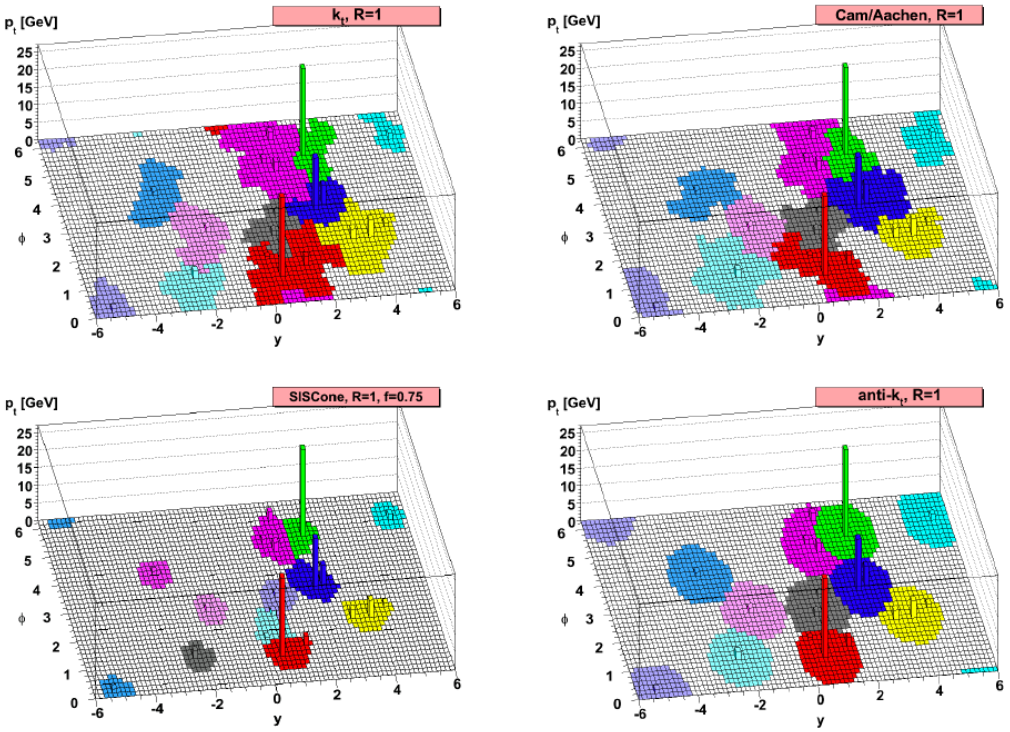

Figure 3.7: Example of clustering by different jet algorithms with the same size parameter [50]. SISCone is a jet-algorithm from Tevatron no longer in use.

3.3.2 Jet Substructure

Even before jets were fully understood some authors [51, 52] asked careful questions about their internal structure, or substructure of jets. These are natural questions to ask. Suppose our collider produces a heavy particle at rest, for example a W boson. W bosons decay into quark anti-quark pairs and we expect to observe two jets since the two quarks come out back-to-back. If we crank up the collider energy the W comes out boosted enough that its decay products become part of a single jet. In order to resolve these Ws one would like to be able to look inside the jet and see if there are two distinct blobs of energy, each corresponding with one of the quarks[3].

[3]Notice the tacit assumption of Parton-Subjet Duality

The field truly flourished after [53] suggested that there are processes for which the signal-to-noise ratio improves in the highly-boosted regime, because as we require higher final state energy the background drops off faster than the signal. In the highly-boosted regime substructure techniques become essential since all the decay products are now inside a single jet. There are many substructure techniques that are worth introducing. Nevertheless, this section will be limited to those we have used in our project. An interested reader may find [54] a good starting point for further study.

Subjets

Once a jet-algorithm has identified a jet j we know its set of its constituent four-vectors $s_j = \{p_i^\mu\}$. If we were to run the jet-algorithm again on s_j it would yield j. In order to obtain n subjets of j we need to stop the jet-algorithm when n four-vectors remain. Another way to see this process is to imagine the entire clustering history (as illustrated in figure 3.8) and take $n-1$ merging steps back to the point when precisely n four-vectors remain. Notice that the jet-algorithm we used to find subjets may be a completely different from the jet-algorithm we used to find the jet j. In fact, we identify jets with the anti-k_T algorithm and look for their subjets with the k_T algorithm. You will see this in our paper.What are subjets good for? For example, top quark initiated jets tend to have two subjets v_1 and v_2 whose masses $|v_1|, |v_2|$ are consistent with the masses of the decay products of the top quark – the W boson and the bottom quark. This is loosely illustrated in figure 3.9. Requiring such a substructure in a jet may significantly reduce the background from jets that do not contain decay products of the top quark.

N-subjettiness

As long as there are enough initial four-vectors inside s_j, we can ask for an arbitrary number n of subjets. However, we will not know which n best reflects the physical substrucutre of the jet j. Authors of [55, 56] came up with a elegant way to solve this problem. They have designed a set of variables called n-subjettiness. They are defined by:

$$\tau_n = \sum_i p_{T,i} \min\left(\Delta R_{1,i}, \ldots, \Delta R_{n,i}\right), \tag{3.3}$$

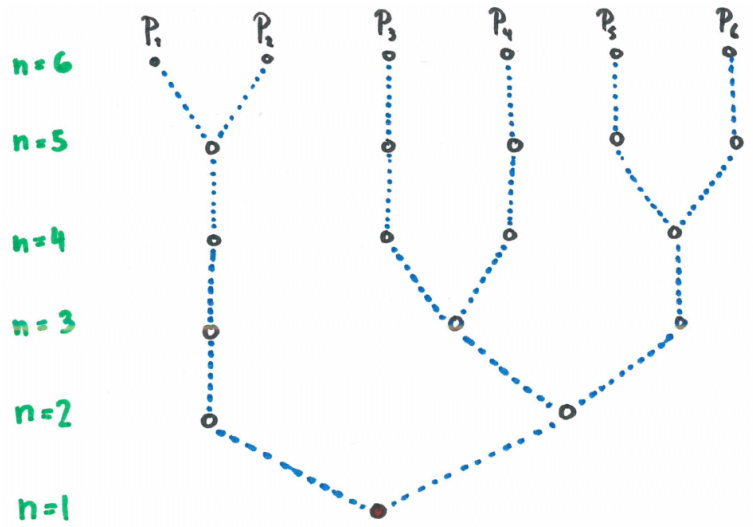

Figure 3.8: An example of jet clustering with six initial four-vectors $p_1, \ldots, p_6$. The green numbers on the left show the number of subjets obtained if the jet-algorithm were to stop at that step.

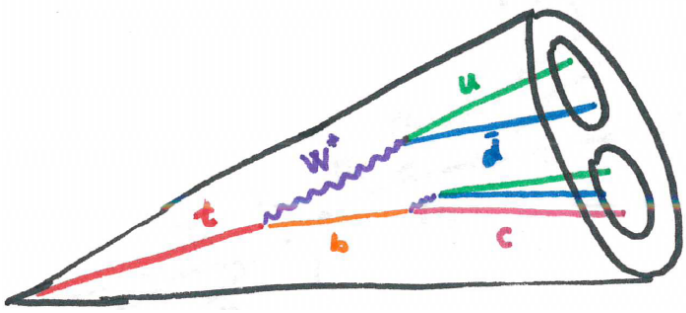

Figure 3.9: This illustration show our motivation for looking for two subjets in order to separate top-initiated subjets from other backgrounds. This illustration completely omits hadronization as well as misrepresents the lifetimes of the individual particles.

where i runs over all constituent four-vectors p_i^μ, $p_{T,i}$ are the transverse momenta associated with p_i^μ,, and $\Delta R_{k,i}$ is the (η, ϕ) distance between p_i^μ and the k-th subjet in the set of n subjets of j. Although this may not seem intuitive at first, a natural interpretation is at hand: τ_n tells us how well the jet constituents align with the n axes defined by the n subjets of the jet. If τ_{n+1} is much smaller than τ_n, then the jet is much better described by $n+1$ axes rather than n axes. If, on the other hand, τ_{n+1} and τ_n are comparable, it means that adding another axis to describe the substructure of the jet is unnecessary. This is why it is often useful to study the ratios $\tau_{n,n+1} = \tau_{n+1}/\tau_n$. Although there may not be a simple one-to-one correspondence between the number of hard partons inside a jet and the drop in $\tau_{n,n+1}$, it is a very useful variable.

3.4 Conclusion

By now, you can not only see why beams of four collimated photons may require additional attention, but you also have the tools to do so. The following section is a paper [57] Stephen Ellis, Tuhin Roy and I have written in order to address the issue of collinear photon beams.

3.5 Photon Jets

3.5.1 Introduction

The Large Hadron Collider (LHC) has clearly exhibited its ability to make discoveries with the observation of a new resonance [58, 59] with even spin that decays to photons and Z bosons as expected of the Standard Model (SM) Higgs particle. Thus precise measurements of the decays of this resonance into various channels (whether standard or not), are of the utmost importance. At the same time, it is essential to verify our understanding of the existing channels, in particular, $h \to \gamma\gamma$. How well are these photons defined? Can physics objects other than single photons leave signatures in the detector similar to that of a photon? Not surprisingly, the answer is yes [60–62]. Given the granularity of the calorimeters, an object consisting of (nearly) collinear photons, typically labeled a photon-jet, will generate a signature similar to that of a single photon. The possibility that the Higgs particle decays to multiple collinear photons is not new [60, 62]. Simple models where the Higgs decays

to almost massless scalars that each in turn decay to a pair of photons, typically do not give rise to events with four separately identifiable photons, but rather to pairs of photon-jets, each with 2 photons. Slightly more complicated models can produce Higgs decays to photon-jets with $4, 6, \cdots$ photons. We will discuss concrete models where the Higgs decays to photon-jets with 2 and 4 photons per photon-jet. Thus it is essential to develop tools to separate single photons from photon-jets from QCD-jets. Otherwise we are unlikely to understand either the signal or the background.

ATLAS recently made attempts to identify photon-jets from Higgs decays [63]. These analyses rely on relaxing the isolation/shower shape criteria, which use the differing distributions of energy deposition within the calorimeter cells to quite successfully discriminate single photons from QCD-jets. Unfortunately, the parameters of the underlying model can be easily adjusted so that the resultant photon-jets pass the strictest isolation/shower shape criteria just like photons. More importantly, loosening isolation criteria results in a larger fake rate for QCD-jets. Discriminating photon-jets from QCD-jets is more challenging than separating single photons from QCD-jets.

Fortunately jet substructure techniques [51, 53, 64–67] have recently been developed to distinguish QCD-jets from jets containing boosted heavy particle decays, and we can use this work for detection of photon-jets. More broadly, 'jets', as defined by an infrared safe jet clustering algorithm, are being proposed as a universal language to describe *all* calorimeter objects including single photons, photon-jets and QCD-jets. By using the tools developed in jet substructure physics, we do not need to rely on isolation cuts. We supplement the traditional/conventional variables currently used to discriminate photons from QCD-jets with substructure variables that probe in detail the energy distribution within the jet. Note that the photons-jets are composed of energetic photons distributed inside the jet, where the distribution is a result of the kinematic features of the model, e.g., the masses and spins of the intermediate particles. The existence of this structure within photon-jet suggests that substructure variables will be efficient at finding and discriminating photon-jets. We show that our analysis is capable of separating photon-jets from both single photons and QCD-jets *at least as* efficiently as the traditional discriminators separate photons from QCD-jets.

There is another important advantage to applying jet substructure techniques to purely

electro-magnetic calorimeter (ECal) objects. The introduction of 'grooming' algorithms (including filtering [53, 68, 69], pruning [70, 71], and trimming [72]) promised to suppress the undesirable contributions to purely hadronic jets from the underlying event (the largely uncorrelated soft interactions surrounding the interesting hard scattering) and from pile-up (the truly uncorrelated proton-proton collisions that occur in the same time window). Indeed, the recent results from studies at ATLAS [73] and CMS [74] indicate this grooming is effective. We expect that this substructure-based grooming will work as well for all ECal based objects.

It should be noted, that in the context of Higgs physics, the decay to photon-jets is not the only example where the collinearity of the decay products adds complexity to the analysis. Collinearity plays a role for traditional decays of the Higgs boson when it is boosted. In Ref. [53], the authors exploited the collinearity of the b-quarks in boosted Higgs decays (both quarks in a single jet) to greatly enhance the chances of detecting the $h \to b\bar{b}$ channel, featuring jet substructure as a mainstream tool (see also Refs. [51, 64, 65]). The application of jet substructure in Higgs physics has now become a very active area of research, applied both to the SM Higgs [75–77] as well to beyond the SM Higgs scenarios [78–83]. For reviews, more detailed descriptions, and references see Refs. [84, 85].

The rest of this chapter is organized as follows: in Sec. 3.5.2, we start with a simplified model for photon-jets. We propose a set of benchmark points, where we take different combinations of masses and parameters in the simplified model to produce photon-jets displaying a variety of distinct kinematics. In Sec. 3.5.3 we define the details of our simulation. We describe, in detail, how we generate samples of photon-jets, one for each of the benchmark points, QCD-jets, and single photons. We present our analysis in Sec. 3.5.4. We describe all the variables that we use in this work to discriminate photon-jets from QCD-jets from single photons. Then we combine these variables in a multivariate analysis. We train boosted decision trees (BDTs) using the samples of jets and use these to optimize the discriminating power of our analyses. We also show how these BDTs can be used to simultaneously separate photon-jets, photons, and QCD-jets from each other. Our conclusions are presented in Sec. 3.5.5.

3.5.2 Simple Model for Photon-Jets

By definition, photons-jets refer to calorimeter objects consisting of more than one hard photon. However, such a broad definition presents a challenge since all photon-jets are not the same. They differ in terms of the number of hard constituent photons as well as in the distribution of those photons within the photon-jet. To provide a systematic phenomenological study of photon-jets we classify these objects in more detail in terms of the production mechanism and consider a broad range. We will refer to the various production scenarios as 'benchmark' scenarios. We find that a simple model in the spirit of Ref. [86] with two new particles is sufficient to characterize these benchmarks. The model includes a small number of interactions and we can vary the strength of these interaction and the new particle masses in order to generate the benchmark scenarios. In particular, we introduce two scalar fields n_1 and n_2 of mass m_1 and m_2 respectively. Without loss of generality, we choose the naming convention such that $m_1 > m_2$. Neither n_1 nor n_2 carry any SM charges. We use the following interactions to generate photon-jets

$$\frac{1}{2}\mu_h\, h n_1^2 + \frac{1}{2}\mu_{12}\, n_1 n_2^2 + \left(\frac{\eta_1}{m_1}\, n_1 + \frac{\eta_2}{m_2}\, n_2\right) F^{\mu\nu} F_{\mu\nu}\ , \tag{3.4}$$

where μ_h, μ_{12} are mass parameters, η_1, η_2 are dimensionless coupling constants, and $F_{\mu\nu}$ is the electromagnetic field strength operator.

This simple model bears a resemblance to a Higgs portal scenario [1, 3, 4] because of the μ_h coupling. In the Higgs portal language, n_1 and n_2 constitute a 'hidden' sector while the coupling μ_h provides a tunnel to the corresponding 'hidden valley'. The electromagnetic couplings (proportional to the η parameters) provide ways for the new particles to decay back to SM particles, photons in this case. With respect to Higgs physics, this simple model provides a realistic example where the SM Higgs field decays through the new particles to multiple photons. In the limit $m_1 \ll m_h$, the resultant photons (the decay products of n_1) are essentially collinear.

In Table 3.1 we list the benchmark scenarios (labeled photon-jet study points or PJSPs) that we investigate in this work. All are generated by varying the parameters in equation (3.4). The symbol X in Table 3.1 denotes that a non-zero value is selected for that parameter, which then determines the decay mode. We have chosen the benchmarks in such

a way that the parameters denoted by X only change the *total* width of the decaying particles. As long as the decays are prompt, the exact values of these parameters are irrelevant to the phenomenological properties of the photon-jets. In all these study points we take the

Study Points	m_1 (GeV)	m_2 (GeV)	μ_{12} (GeV)	η_1	η_2
PJSP **1**	0.5				
PJSP **2**	1.0		0	X	
PJSP **3**	10.0				
PJSP **4**	2.0	0.5			
PJSP **5**	5.0	0.5			
PJSP **6**		1.0	X	0	X
PJSP **7**	10.0	0.5			
PJSP **8**		1.0			

Table 3.1: The study points used in our analysis. For PJSP $\mathbf{1}-\mathbf{3}$, n_2 does not participate in the decay chain since $\mu_{12}=0$ and the m_2 and η_2 columns are empty. By X we denote that a non-zero value is chosen for the parameter, which facilitates prompt decays, but the specific value plays no role.

Higgs particle to decay to a pair of n_1 particles. The small n_1 mass ($m_1 \ll m_h$) ensures that the decay products of the n_1 are highly collimated. In the Higgs particle rest frame, which is close to the laboratory frame on average, each n_1 has momentum $\sim m_h/2$ and the typical angular separation between the n_1 decay products is of the order of $4m_1/m_h$. Note that, given we always consider $m_1 \leq 10$ GeV, we expect the typical angular separation between the n_1 decay products to be $\lesssim 1/3$ (we use $m_h = 120$ GeV). As long as the angular size of photon-jets is larger than 1/3, we expect to capture all the decay products of the n_1 in each photon-jet for all the benchmark points.

For the study points PJSP $\mathbf{1}-\mathbf{3}$ the mass parameter μ_{12} is set to zero and $n_1 \to \gamma\gamma$ is the only possible n_1 decay mode. Hence these scenarios are characterized by photons-jets

with typically 2 hard photons per jet, and n_2 plays no role in the phenomenology (so no n_2 mass or coupling values are included in the table). In these scenarios the Higgs particle cascade decays to four photons ($h \to n_1 n_1 \to \gamma\gamma\gamma\gamma$). The precise value of m_1 governs the angular separation of the two photons inside the photon-jets. For a very small m_1, each photon-jet looks much like a single photon. (Of course, if the Higgs is highly boosted, the decay results in a single photon-jet containing all 4 photons.)

For study points PJSP $\mathbf{4-8}$ we set η_1 to zero and μ_{12} to a non-zero value. In these contrasting scenarios the only n_1 decay mode involves the chain $n_1 \to n_2 n_2 \to \gamma\gamma\gamma\gamma$. Hence the Higgs decays again to two photon-jets, but now each photon-jet typically contains four photons (the n_1 decay products). (In this case, a highly boosted Higgs yields a single photon-jet containing 8 photons.)

3.5.3 Simulation Details

In order to generate samples of photons-jets, we implement the simple model of equation (3.4) in MadGraph 5 [87]. For each benchmark point we generate matrix elements corresponding to the process $pp \to h \to n_1 n_1$ (via gluon fusion) using MadGraph 5 with $m_h = 120$ GeV, which we employ as input to Pythia 8.1 [88,89] in order to generate the full events and for the subsequent n_1 decays. Since the Higgs production is evaluated at lowest order, the produced Higgs particles have zero transverse momentum. We use the QCD dijet events generated by standalone Pythia 8.1 to provide a sample of QCD-jets. In order to define a sample of single photons, we also generate $pp \to h \to \gamma\gamma$ events where the photons are well separated. Finally, we include initial state radiation (ISR), final state radiation (FSR) and multiple parton interactions (MI, i.e., the UE) as implemented in Pythia 8.1 to simulate the relevant busy hadronic collider environment.

The Pythia output final states are subjected to our minimal detector simulation. In the following we describe briefly how we treat the final state particles in each event:

- We identify all charged particles with transverse momentum $p_T > 2$ GeV and pseudorapidity $|\eta| < 2.5$ as charged tracks.

- In a real detector, tracks are also generated if photons convert within the pixel part of

the tracker. In this work, we simulate this photon conversion process by associating with each photon a probability for it to convert in the tracker. [4]

The probability is a function of the number of radiation lengths of material the photon has to traverse in order to escape the inner part of the tracker. We use the specifications of the ATLAS detector in order to model this pseudorapidity dependent probability distribution. The details of this procedure are outlined in section 3.5.6.

- In our simulation, all particles (except charged particles with $E < 0.1$ GeV) reach the calorimeters, and all of these (except muons with $p_T > 0.5$ GeV) deposit all of their energy in the calorimeters. The electromagnetic calorimeter (ECal) is modeled as cells of size 0.025×0.025 in (η-ϕ), whereas the hadronic calorimeter (HCal) is taken to have more coarse granularity with 0.1×0.1 cells. Besides photons and electrons, soft muons and soft hadrons (soft means $E < 0.5$ GeV) are treated as depositing all of their energy in the ECal. More energetic hadrons are absorbed in the HCal, while more energetic muons escape the calorimeter. For a more detailed picture see section 3.5.6.

- We attempt to simulate the showering that occurs within the ECal. We distribute the energy of each particle that is absorbed in the ECal into a (3×3) grid of cells (centered on the direction of the original particle) according to a precomputed Molière matrix corresponding to the Molière radius of lead. For details on this transverse smearing see section 3.5.6. The structure induced by this shower simulation is observable in our final results.

- We implement calorimeter energy smearing for both the ECal and the HCal. The calorimetric response is parametrized through a Gaussian smearing of the accumulated cell energy E with a variance σ:

$$\frac{\sigma}{E} \;=\; \frac{S}{\sqrt{E}} + C \;, \tag{3.5}$$

[4] We do not simulate the magnetic field in the detector. Consequently the e^+e^- pairs from photon conversion continue in the direction of the photon. So for every converted photon we obtain effectively a single track, if the photon passes the p_T threshold.

where S and C are the stochastic and constant terms. For the ECal and the HCal, we use (S, C) to be $(0.1, 0.01)$ and $(0.5, 0.03)$, respectively, in order to approximately match the reported calorimeter response from ATLAS [90].

- Each calorimeter cell that passes an energy threshold becomes an input for our jet clustering algorithm. For the ECal cells we require $E_T > 0.1$ GeV, while for the HCal cells we use the somewhat harder cut $E_T > 0.5$ GeV. [5] We sum all the energy deposited in a given calorimeter cell and construct a massless 4-vector with the 3-vector direction corresponding to the location of that cell.

- As the final step we cluster the 4-vectors corresponding to the calorimeter cells into jets using Fastjet 3.0.3 [91, 92]. In particular, we use the anti-k_T jet clustering algorithm [50] with $R = 0.4$ and and require $p_T > 50$ GeV for every jet. Only the leading jet from each event is retained for further analysis in order to maintain independence among the jets in the sample.

3.5.4 Analysis

In this section we describe the analysis of 10 samples of jets generated according to the prescription of the previous sections. The first sample contains QCD jets derived from QCD dijet events. The second sample consists of jets from $h \to \gamma\gamma$ events where each jet typically contains one of the photons from the Higgs decays, plus contributions from the rest of the event (ISR, FSR, UE). We refer to the jets in this sample as single photon jets, or simply single photons. The remaining 8 samples of jets are the photon-jet samples and correspond to the 8 study points in Table 3.1. As noted above, in these events the Higgs particle decays into 4 or 8 photons and the corresponding photon-jets typically contain either 2 or 4 photons. The resulting p_T distributions for QCD-jets (red), photon-jets (blue) (PJSP **8**) and single photons (green) are indicated in figure 3.10.

As expected, the p_T distribution for QCD-jets is a falling distribution, while both the

[5] The specific values are chosen to mimic the choices for real detectors and the difference between the two accounts for the differing noise levels in calorimeter cells of different sizes.

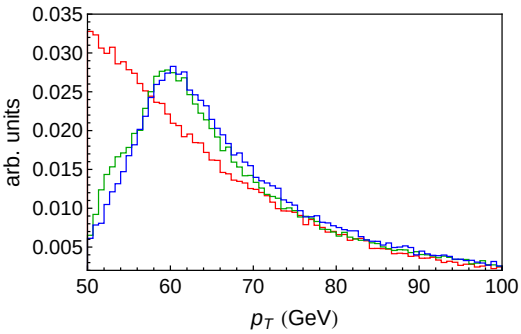

Figure 3.10: The p_T distribution of jets for QCD-jets (red), single photons (green), and for photon-jets (blue) from the study point PJSP **8**. Jets are constructed as described in the text (the anti-k_T algorithm with $R = 0.4$).

single photon and photon-jet distributions exhibit a peak near $m_h/2(= 60$ GeV). We understand this last point as arising from the production of Higgs particles with zero transverse momentum followed by 2-body decays (either 2 photons or 2 n_1's). It is the remnants of these two bodies that are typically captured in the jets yielding the indicated peaks near $p_T \sim m_h/2$. For the photon-jet sample we only show the p_T spectrum for the study point PJSP **8**, but note that the p_T distributions are almost identical for all other benchmark points. As indicated in figure 3.10, the jets in all of these samples of events have crudely comparable transverse momentum distributions in the range $50 - 100$ GeV, although the QCD sample is more strongly peaked at the low end. Thus studying the jets in these samples should provide a useful laboratory in which to study photon-jets, QCD jets and single photons.

The remainder of this section describes a systematic analysis aimed at distinguishing photon-jets from QCD-jets as well as from single photons. We begin with brief descriptions of the variables that provide the discriminating power. The variables are organized into two groups: (i) conventional variables and (ii) substructure variables. We demonstrate how each of these variables individually discriminates photons-jets form the jet samples. Later in this section, we combine these variables in a multivariate analysis in order to maximize the separation of photon-jets from QCD-jets as well as from single photons.

Conventional Variables

The conventional variables we describe below are well known, well understood, and play essential roles in the identification of single photons, i.e., the separation from QCD-jets. We expect these variables to play a similar role in separating photon-jets from QCD-jets, since the probability distributions as functions of these variables are similar for photon-jets and for single photons. On the other hand, they cannot be expected to efficiently discriminate photon-jets from single photons.

Hadronic Energy Fraction, θ_J

We define the hadronic energy fraction θ_J for a jet to be the fraction of its energy deposited in the hadronic calorimeter:

$$\theta_J \;=\; \frac{1}{E_J} \sum_{i \in \mathrm{HCal} \in J} E_i \tag{3.6}$$

where E_J is the total energy of the jet, and E_i is the energy of the i-th HCal cell that is a constituent of the jet. This is the most powerful variable for discriminating a single photon or a photon-jet (objects that deposit most of their energy in the ECal) from QCD-jets. Since a QCD-jet typically contains 2/3 charged pions and 1/3 neutral pions, we expect to see a peak at $\theta_J \sim 2/3$ ($\log \theta_J \sim -0.2$) for QCD-jets. Isolated single photons and photon-jets, on the other hand, should exhibit very small θ_J values. However, we start with objects identified by a jet algorithm so there will be contributions from the rest of the event and pile-up, and from leakage from the ECal into the HCal. Thus the precise value of θ_J for single photons and photon-jets will depend on detailed detector properties and on the contribution from the underlying event and pile-up. Nevertheless, we expect single photons/photon-jets to exhibit very small values of θ_j.

Figure 3.11 shows the probability distribution versus $\log \theta_J$ for QCD-jets (red), single photons (green), and for photon-jets (blue) in our simulated data. For the photon-jets we only show the study point PJSP **8**, since the distribution is essentially identical for the other benchmark points. As expected the QCD-jet distribution peaks near $\log \theta_J = -0.2$ ($\theta_J = 2/3$), while the single photon and photon-jet distributions are very similar with a peak near $\log \theta_J = -1.9$ and an implied tail to very small θ_J values. The clear separation

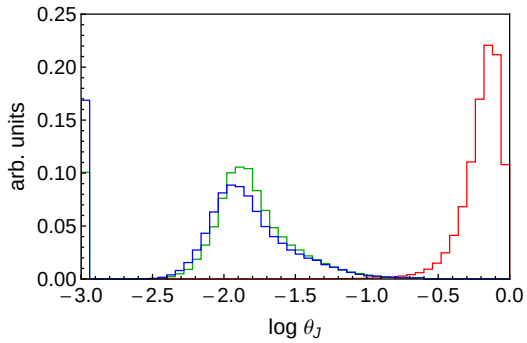

Figure 3.11: The probability distributions for jets as functions of $\log \theta_J$ for QCD-jets (red), single photons (green) and photon-jets from PJSP **8** (blue). The first bin of the plot (at $\theta_J = 10^{-3}$) has an open lower boundary, i.e., it includes all jets with $\log \theta_J < -3.0$.

of the single photon/photon-jet distributions from the QCD-jet distribution indicates why this variable plays such an important role in the separation of QCD-jets from photons.

Any reasonable cut on θ_J ($\theta_J \sim 0.1$) will reduce the QCD-jet contribution by factors of 10^{-2}–10^{-3}, while barely changing the photon/photon-jet contribution. We impose a preliminary cut by keeping only $\theta_J \leq 0.25$ ($\log \theta_J \leq -0.6$). About 2% of the original QCD-jets survive this cut, while approximately 94% of the single photons/photon-jets survive. We use the modified jet samples that pass this preliminary θ_J cut for the remainder of this paper.

Number of Charged Tracks, ν_J

In conventional collider phenomenology, the number of charged particles (tracks) associated with an object is often used to distinguish objects from each other. Although photons and electrons generate similar signatures in the ECal, the latter are typically associated with a track while the former are not. Tracks also play an important role in rejecting QCD-jets since, as mentioned before, a QCD-jet typically contains several charged pions.

In our simulated data we keep all charged particles with $p_T > 2$ GeV and assume that all of these correspond to tracks in a real detector. In order to associate these tracks with the jets, which are constructed entirely from calorimeter cells, we perform the following

analysis. First replace each track by an arbitrarily soft light-like four vector with the same (η-ϕ) direction as the track, and then include these soft four-vectors in the jet clustering process along with the calorimeter cells. (We explicitly check that the inclusion of these soft four-vectors does not affect the outcome of the clustering procedure.) A track is associated with a jet if the soft four vector corresponding to that track is clustered into that jet [6]. The resulting total number of tracks associated with a jet yields the value of ν_J for that jet. Figure 3.12 shows the relative probability distribution versus the number of tracks per

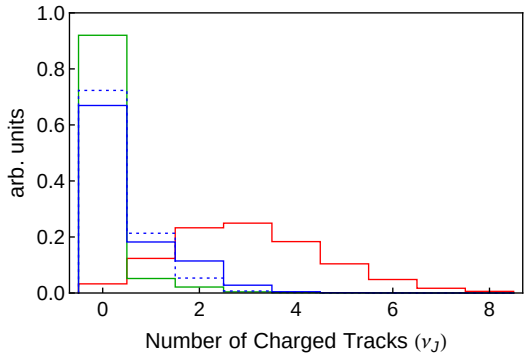

Figure 3.12: The relative probability distribution for QCD jets (red), single photons (green) and photon-jets (blue) versus the number of charged tracks associated with a jet. The algorithm for associating tracks with jets is given in the text. For photon-jets we show the distribution for jets from the study points PJSP **1** (dotted) and PJSP **8** (solid).

jet (ν_J) for QCD-jets (red), single photons (green) and photon-jets (blue). As expected, the number of tracks associated with QCD-jets varies over a broad range and only a tiny fraction of QCD-jets have no associated tracks. The single photon/photon-jet samples, on the other hand, are dominated by jets with no associated tracks. Photons that convert yield tracks associated with the corresponding jets. Since the probability of conversion increases with the number of photons per jet, the probability of obtaining one of more associated

[6] As a check we also consider the more traditional construction where a track is associated with a jet if it is within an angular distance R or less from the given jet's direction, where R is the size-parameter used in the clustering algorithm. For anti-k_T jets both methods yield identical associations of tracks and jets. For the k_T or C/A algorithms, where jets are not exactly circular, the method described in the text is a more natural definition of whether a track is associated with a jet or not.

tracks increases from single photon jets (single photons) to jets with two photons (typical for PJSP **1**, the dotted blue curve) to jets with four photons (typical for PJSP **8**, the solid blue curve). As with the variable θ_J, ν_J offers some separation between QCD-jets and single photons, but much less between single photons and photon-jets (and even less between the different types of photon-jets).

Jet Substructure

Next we want to focus on variables that explicitly characterize the internal structure of jets, i.e., characterize the energetic subjet components of the jet. Recall that in this analysis we have identified jets using the the anti-k_T jet algorithm with $R = 0.4$, but we do not expect the general features of our analysis to depend on this specific choice. The next step is to determine a 'recombination tree' for the jets we want to study (here the leading jet in each event). To this end we apply the k_T algorithm [48, 93] to the calorimeter cells identified as constituents of the jet in the first step. (We could as well use the Cambridge/Aachen (C/A) algorithm [49, 94, 95], but not the anti-k_T algorithm in this step as anti-k_T does not tend to produce a physically relevant recombination tree.) This recombination tree specifies the subjets at each level of recombination N from $N = 1$ (the full jet) to $N =$ the number of constituent calorimeter cells in the jet (no recombination). At the next step the subjet variables we study fall into two classes. In the first class we attempt to count the effective number of relevant subjets without using any properties of the subjets in the tree except their directions in η-ϕ. In this case the useful variable (defined in detail below) is called N-subjettiness. The N-subjettiness variable for a given jet becomes numerically small when the parameter N is large enough to describe all of the relevant substructure, i.e., this value of N provides a measure of the number of subjets without explicitly identifying the subjets. N-subjettiness involves *all* components of the original jet for all values of N.

The rest of the substructure variables we study more explicitly resolve a jet into a set of subjets. We define both the level in the recombination tree at which we choose to work, i.e., the number of subjets we have split the jet into and how many of these subjets to use in the subsequent analysis. We use $N_{\text{pre-filter}}$ (this notation should become clear shortly)

and N_{hard} to label these two parameters. Thus we start with the 4-vectors corresponding to the (calorimeter cell) constituents of a given jet, and then (re)cluster these constituents using the chosen subjet algorithm (which is not necessarily the algorithm used to originally identify the jet) in *exclusive* mode, i.e. we continue (re)clustering until there are precisely $N_{\text{pre-filter}}$ 4-vectors left – the $N_{\text{pre-filter}}$ exclusive subjets. Out of these $N_{\text{pre-filter}}$ subjets we pick the N_{hard} largest p_T subjets and discard the rest. All the substructure variables discussed below (except N-subjettiness) are constructed using these N_{hard} subjets. Note that by choosing $N_{\text{pre-filter}} > N_{\text{hard}}$, we have performed a version of jet 'grooming' typically labeled filtering [53, 68, 69]. This will ensure that our results are relatively insensitive to the effects of the underlying event and pile-up. Ideally, the integers $(N_{\text{hard}}, N_{\text{pre-filter}})$ should be chosen based on the topology of the object we are looking for. However, the naive topology will be influenced by the interaction with the detector and the details of the jet clustering algorithm. For example, a 4 photon photon-jet will often appear in the detector to have fewer than 4 distinct lobes of energy, i.e., one or more photons often merge inside a single lobe of energy. In our simulation, we find that the choice $N_{\text{hard}} = 3$ and $N_{\text{pre-filter}} = 5$ is an acceptable compromise, working reasonably well for single photons and photon-jets from all the study points. Further optimization will be possible in the context of real detectors and searches for specific photon-jet scenarios.

N-Subjettiness, τ_N

"N-subjettiness", introduced in Ref. [55, 56], is a modified version of "N-jettiness" from Ref. [96]. It is adapted in a way such that it becomes a property of a jet rather than of an event. N-subjettiness provides a simple way to effectively count the number of subjets inside a given jet. It captures whether the energy flow inside a jet deviates from the one-lobe configuration expected to characterize a typical QCD-jet. We use the definition of N-subjettiness proposed in Ref. [55]. The starting point is a jet, the full set of 4-vectors corresponding to the (calorimeter cell) constituents of the jet (here found with the anti-k_T algorithm for $R = 0.4$), and the recombination tree found with the k_T algorithm as outlined above. From this tree we know the 4-vectors describing the exclusive subjets for any level

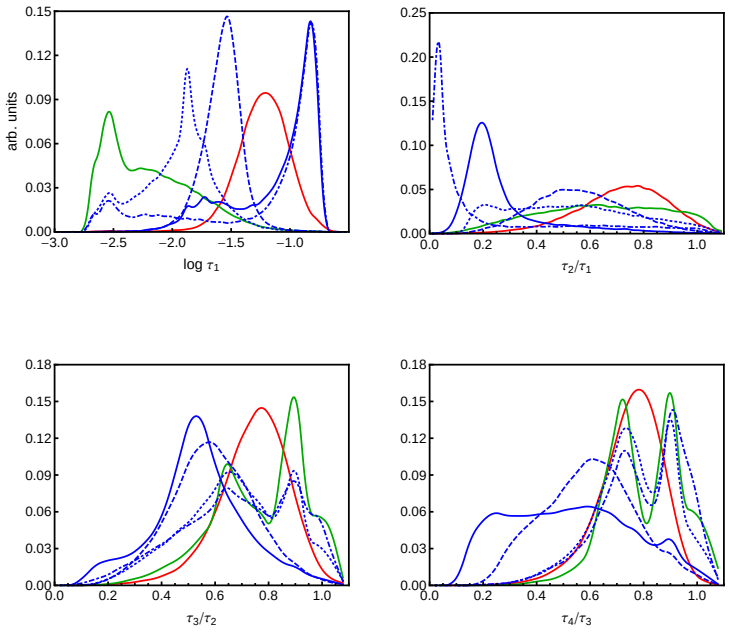

Figure 3.13: Probability distributions versus various N-subjettiness variables. The solid red and green curves show, as usual, the distributions for QCD-jets and single photons respectively. Various blue curves are for photon-jets from different study points. The solid, dashed, dotted and dash-dotted curves in all these figures are for PJSP **8**, PJSP **4**, PJSP **1** and PJSP **3** respectively.

N, i.e., the level where there are exactly N subjets. With this information we can define N-subjettiness to be

$$\tau_N = \frac{\sum_k p_{T_k} \times \min\{\Delta R_{1,k}, \Delta R_{1,k}, \cdots, \Delta R_{N,k}\}}{\sum_k p_{T_k} \times R} \,, \tag{3.7}$$

where k runs over all the (calorimeter cell) constituents of the jet, p_{T_k} is the transverse momentum for the k-th constituent, $\Delta R_{l,k} = \sqrt{(\Delta\eta_{l,k})^2 + (\Delta\phi_{l,k})^2}$ is the angular distance between the l-th subjet (at the level when there are N subjets) and the k-th constituent of the jet, and R is the characteristic jet radius used in the original jet clustering algorithm.

In the context of single photons, photon-jets and QCD-jets, we use N-subjettiness in two different ways. The first application is to use the *ratios* τ_{N+1}/τ_N in the same way N-subjettiness is used to tag boosted massive particles such as a W boson or a hadronic

decaying top [55,56]. In particular, for a jet with N_0 distinct lobes of energy, τ_{N_0} is expected to be much smaller than τ_{N_0-1} (of course, we are assuming $N_0 > 1$), whereas for $N > N_0$, τ_{N+1} is expected to be comparable to τ_N. Thus a two photon photon-jet is expected to be characterized by $\tau_2/\tau_1 \ll 1$. On the other hand, one lobed QCD-jets and single photons should exhibit comparable values for τ_2 and τ_1, and consequently $\tau_2/\tau_1 \sim 1$.

The second way in which we use N-subjettiness consists of using the magnitude of τ_1 itself. Even for a jet with one lobe of energy the exact magnitude of τ_1 represents a measure of how widely the energy is spread. A pencil-like energy profile, like that of a single photon or a narrow photon-jet, should yield a much smaller τ_1 compared to QCD-jets with a much broader profile. In fact, τ_1 is an indicator of jet mass, and, for jets with identical energy, τ_1 is proportional to the square of the jet mass.

Figure 3.13 shows the probability distributions versus $\log \tau_1$ and τ_{N+1}/τ_N for $N = 1, 2, 3$ corresponding to single photons, QCD-jets and photon-jets from different study points. Note that for photon-jets, the jet mass is almost always given by the mass parameter m_1 in Table 3.1. Thus for PJSP **8** and PJSP **3**, where m_1 has the same value, the probability distributions versus $\log \tau_1$ are almost identical. For study points PJSP **8**, PJSP **4** and PJSP **1** the peak in $\log \tau_1$ shifts to the left as the value of m_1 decreases (from 10 GeV to 2 GeV to 0.5 GeV). Note also that the PJSP **1** and PJSP **3** distributions exhibit a small τ_1 (small mass) enhancement at essentially the same τ_1 value as the primary peak in the single photon (green curve) distribution. This presumably corresponds to those kinematic configurations where only one of the (two) photons from the n_1 decay is included in the jet. Thus we expect that a (small) fraction of the time these scenarios will look very single photon-like.

Clearly the ratio τ_2/τ_1 gives significant separation for the different photons-jet scenarios. The study points PJSP **8** and PJSP **3** are now separated, although both exhibit peaks at small values of the ratio. This suggests an intrinsic 2-lobe structure corresponding to 2 photons for PJSP **3** and 4 photons in two relatively tight pairs ($m_2 \ll m_1$) for PJSP **8**. PJSP **4** with presumably a more distinctive 4 photon structure exhibits a broader peak at a larger value of τ_2/τ_1. Single photons and PJSP **1** exhibit even broader distributions presumably corresponding to an intrinsically 1-lobe structure. The QCD-jet distribution is also broad but with an enhancement around $\tau_2/\tau_1 = 0.8$, presumably arising from a

typical 1-lobe structure but some contribution from showers with more structure and from the underlying event. The ratios τ_3/τ_2 or τ_4/τ_3 seem to be less effective in discriminating photon-jets from single photons and QCD-jets. This can be understood by noting that quite often the hard photons inside a photon-jet become collinear at the scale of the size of the cell. So even for photon-jets with 4 hard photons, we rarely find jets with 4 distinct centers of energy. In general we expect the ratio τ_{N+1}/τ_N becomes less and less useful with increasing N.

Note that the distributions for single photons and photon-like photon-jets tend to exhibit a double peak structure in τ_3/τ_2 or τ_4/τ_3. We believe that this feature arises from both the contributions due to the underlying event and due to our implementation of transverse smearing in the ECal (see section 3.5.6).

Transverse momentum of the Leading Subjet

Now we proceed to discuss the second class of subjet variables constructed from the 3 hardest subjets out of the 5 exclusive subjets. As the first such variable consider the fraction of the jet transverse momentum carried by the leading subjet, which provides significant information about the jet itself. In particular, it indicates the fraction of the jet's total p_T carried by the leading subjet only. Since photon-jets result from the decay of massive particles into hard and often widely separated photons inside the jet, the subjets are usually of comparable hardness. The leading subjet for single photons and for QCD-jets, on the other hand, typically carry nearly the entire p_T of the jet. So for the majority of these jets, the p_T of the leading subjet (label it p_{T_L}) is of the order of the p_T of the entire jet (p_{T_J}). Instead of using the ratio p_{T_L}/p_{T_J} directly we find that it is more instructive to define the variable

$$\lambda_J \;=\; \log\Big(1 - \frac{p_{T_L}}{p_{T_J}}\Big)\,. \tag{3.8}$$

The advantage of using the definition in equation (3.8) is that it focuses on the behavior near $p_{T_L} \sim p_{T_J}$.

The discussion above depends crucially on how the subjets are constructed, especially for QCD-jets. QCD partons typically shower into many soft partons/hadrons. After showering

and hadronization, single hard partons yield many soft hadrons distributed throughout the jet. The way in which these jets are clustered into subjets dictates the p_T distribution of subjets. For example, for anti-k_T subjets, the hardest subjet will always have $p_{T_L} \simeq p_{T_J}$. The k_T algorithm, on the other hand, clusters the softer elements first and results in more evenly distributed subjets. The C/A jet algorithm clusters taking into consideration only the geometric separations of the elements, and produces qualitatively different results. Single photons, on the other hand, shower very little (no QCD Shower) and deposit energy in only a handful of cells (per hard photon). Therefore we expect that our results for single photons or photon-jets will be less sensitive to the details of the clustering algorithm. To versify this point we use both k_T and C/A subjets to evaluate λ_J from equation (3.8). The simultaneous use of different clustering algorithms to extract information from the same jet should not come as a surprise. As shown in Ref. [97], substantial further information can be extracted if one employs a broad sampling out of *all* of the physically sensible clustering histories (trees) for a given jet. In this sense the current analysis is modest in that we only use two specific clustering procedures.

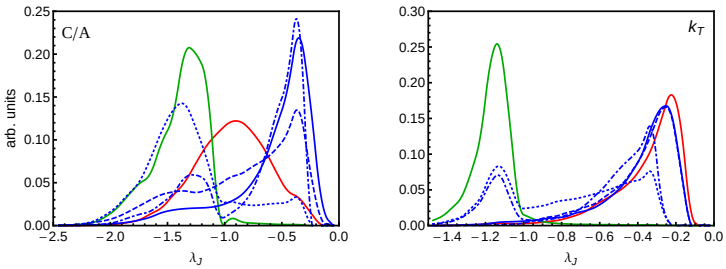

Figure 3.14: Probability distribution for λ_J from equation (3.8). As in figure 3.13 the solid red is for QCD-jets, the solid green for single photons, dotted blue for PJSP **1**, dash-dotted blue for PJSP **3**, dashed blue for PJSP **4** and solid blue for PJSP **8**. The left (right) figure shows the distribution when λ is calculated using C/A (k_T) subjets.

In figure 3.14 we plot the probability distribution of jets as a function of λ_J for QCD-jets, single photons, and photon-jets. The left (right) panel shows the distribution when we use the C/A (k_T) algorithm to find the subjets. Note how the distribution for QCD-jets

(the red curve) moves more to the right (i.e., the p_T of the jet gets more evenly distributed among its subjets) as we go from C/A subjets to k_T subjets. The various photon-jet study points also look more similar when using the k_T algorithm. In this case the PJSP **1** and PJSP **3** distributions exhibit enhancements suggesting the presence of both single photon-like behavior ($\lambda_J \sim -1.2$) and QCD-like behavior ($\lambda_J \sim -0.2$ to -0.3). The more complex structure of the PJSP **4** and PJSP **8** jets exhibit a distribution closer to QCD alone. Finally note that the C/A subjets display the jet substructure information differently from the k_T case with the peak in the QCD-jet distribution at least somewhat separated from the peaks in the photon-jet distributions. Also for C/A all of the photon-jet scenarios exhibit at least a little single photon-like enhancement (for k_T this is only true for PJSP **1** and PJSP **3**). There is clearly some discrimination to be gained from using more than one definition of the subjets.

Energy-Energy Correlation, ϵ_J

Another useful variable is the "energy-energy correlation". We define it as:

$$\epsilon_J \;=\; \frac{1}{E_J^2} \sum_{(i>j)\in N_{\text{hard}}} E_i E_j \,, \tag{3.9}$$

where E_J is the total energy of a given jet, and the indices i, j run over the (3 hardest) subjets of the jet. From the definition, it should be clear that ϵ_J is sensitive to the energy of the subleading jets. In particular, the energy-energy correlation can be expressed as

$$\begin{aligned} \epsilon_J &= \tfrac{E_L(E_{NL}+E_{NNL})+E_{NL}E_{NNL}}{E_J^2} \\ &\approx \tfrac{E_L(E_J-E_L)+E_{NL}E_{NNL}}{E_J^2} \,, \end{aligned} \tag{3.10}$$

where E_L, E_{NL}, and E_{NNL} are the energies of the leading subjet, the next-to-leading subjet, and the next-to-next-to-leading subjet.

We show the probability distribution of jets as a function of ϵ_J for QCD-jets, single photons and photon-jets in figure 3.15. Note that for single photons (the green curve), E_{NL} and E_{NNL} are negligible and hence we expect ϵ_J for single photons to be well approximated by $E_L\left(E_J - E_L\right)/E_J^2$. In fact, the sharp peak for single photons in figure 3.14

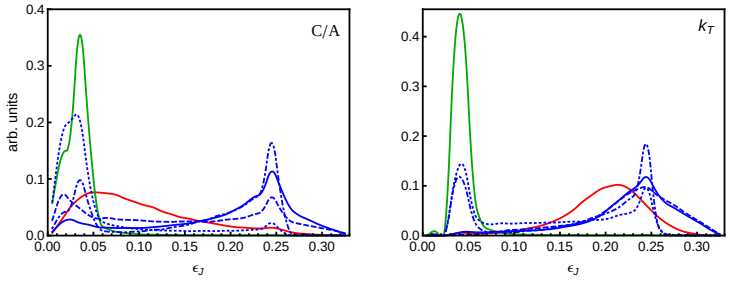

Figure 3.15: Probability distribution versus ϵ_J from equation (3.9). As in figure 3.13 the solid red is for QCD-jets, the solid green for single photons, dotted blue for PJSP **1**, dash-dotted blue for PJSP **3**, dashed blue for PJSP **4** and solid blue for PJSP **8**. The left (right) figure shows the distribution when ϵ_J is evaluated using C/A (k_T) subjets.

at -1.2 (k_T algorithm) corresponds to the sharp peak at about 0.04 in figure 3.15. More generally the qualitative features in figure 3.14 are repeated in figure 3.15. For C/A subjets the distributions for all of the photon-jet study points exhibit two peaks, the large ϵ_J value enhancement presumably corresponding to the energy being shared approximately equally among several final photons, while the small value enhancement arises from the case when one photon dominates (perhaps because some of the photons are not in the jet). For k_T subjets only the PJSP **1** and PJSP **3** distributions exhibit the small ϵ_J single photon-like enhancement. We also see that again the two algorithms yield distinctly different distributions for QCD-jets.

Subjet Spread, ρ_J

We define "subjet spread" as a measure of the geometric distribution of the subjets.

$$\rho_J = \frac{1}{R} \sum_{(i>j)\in N_{\rm hard}} \Delta R_{i,j} \ , \tag{3.11}$$

where $\Delta R_{i,j}$ is the angular distance between the i-th and j-th (hard) subjets, and R is the size parameter of the jet algorithm.

The left (right) panel of figure 3.16 shows the probability distribution of jets as a function of ρ_J for QCD-jets, single photons and photon-jets when the C/A (k_T) subjets are

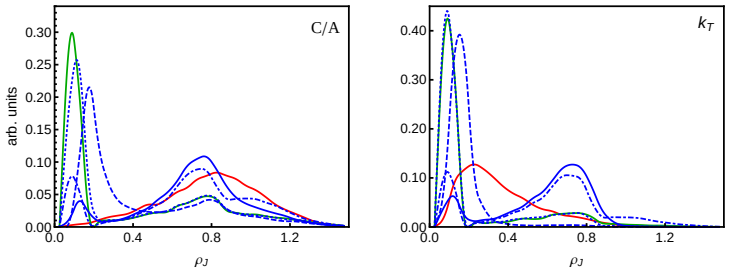

Figure 3.16: Probability distribution for subjet-spread ρ_J from equation (3.11). As in figure 3.13 the solid red is for QCD-jets, the solid green for single photons, dotted blue for PJSP **1**, dash-dotted blue for PJSP **3**, dashed blue for PJSP **4** and solid blue for PJSP **8**. The left (right) figure shows the distribution when ρ_J is calculated using C/A (k_T) subjets.

used to evaluate equation (3.11). For this variable only the QCD-jet distribution changes dramatically when changing the choice of subjet algorithm from C/A to k_T. By using both algorithms this feature will provide some ability to discriminate between QCD-jets and single photons or photon-jets. For the single photon case the the strong peak at small ρ_J confirms that all of the subjets are close to each other, forming a hard core. Subjet spread is quite sensitive to the mass m_1 as can be seen from the different photon-jet distributions. In particular, the position of the peaks for photon-jets with different m_1 simply follow the m_1 value. The PJSP **3** and PJSP **8** distributions are nearly the same (with the same m_1 value), while the PJSP **1** and PJSP **4** distributions are just similar (with somewhat different m_1 values), but distinct from PJSP **3** and PJSP **8**. The m_1 dependence is not surprising since the opening angle between the decay products of the n_1 particle depends on m_1. Finally we note that the PJSP **3** and PJSP **8** distributions do have an enhancement at small ρ_J values presumably corresponding to configurations where the extra photons are not captured in the jet.

Subjet Area of the Jet

As defined in Ref. [98], the "area" associated with a jet is an unambiguous concept that represents quantitatively the amount of surface in the (η-ϕ) plane included in a jet. In

this analysis, we use the "active area" definition for the area of the jet. The active area of a jet is calculated by adding a *uniform* background of arbitrarily soft 'ghost' particles to the event (so that each ghost represents a fixed area) and then counting the number of ghosts clustered into the given jet. The area of a jet is often used to provide a quantitative understanding of the largely uncorrelated contributions to a jet from the underlying event and pile-up. However, it is rarely used in phenomenology for the purpose of discovering new particles or tagging jets. We use 'subjet area' as a measure of the 'cleanliness' of the jet. We show that it can be a useful tool for distinguishing a single photon or a photon-jet from noisier QCD-jets. We define the subjet area fraction as

$$\delta_J = \frac{1}{A_J} \sum_{i \in N_{\text{hard}}} A_i \ , \tag{3.12}$$

where A_i is the area of the i-th subjet and A_J is the area of the entire jet. Note that this definition of δ_J is only useful when the subjets are constructed geometrically by merging the nearest neighbors first (i.e., using the C/A algorithm). In figure 3.17, we show the

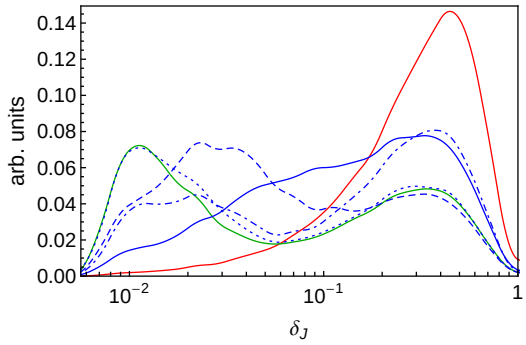

Figure 3.17: Probability distribution versus fractional area δ_J from equation (3.12). As in figure 3.13 the solid red is for QCD-jets, the solid green for single photons, dotted blue for PJSP **1**, dash-dotted blue for PJSP **3**, dashed blue for PJSP **4** and solid blue for PJSP **8**. We use C/A subjets to calculate δ_J.

probability distribution for jets as a function of δ_J for QCD-jets, single photons, and photon-jets. As expected, the figure shows that single photons (the green curve) are significantly cleaner (exhibit smaller δ_J values) than QCD-jets (the red curve) and that photon-jets (the

blue curves) tend to lie in between. Fixing m_1 such that the first splitting is fairly wide, we can investigate the effects of m_2. If m_2 is small, then the two photons coming from the n_2 decays will be very close together, and the subjet that contains them will not collect many ghosts. On the other hand, a large m_2 will split the two photons further apart and, if still contained in the same subjet, that subjet will collect substantially more ghosts resulting in a subjet with a larger active area. QCD-jets contain many soft particles and so the subjets in QCD jets have larger areas. Thus we see that the QCD distribution peaks for δ_j near 0.5, while the single photon distribution exhibits both a large peak at small ($\sim 10^{-2}$) δ_J and a smaller peak at larger (~ 0.4) δ_J values. The photon-jet cases interpolate between these two behaviors and this variable can clearly provide some discriminating power.

Multivariate Analysis

We have, so far, introduced a set of well-understood variables. In this subsection, we will employ these variables in a multivariate discriminant, specifically in a Boosted Decision Tree (BDT) [99]. A decision tree is a hierarchical set of one-sided cuts used to discriminate signal versus background. The 'boosting' of a decision tree extends this concept from one tree to several trees which form a forest. The trees are derived from the same training ensemble by reweighing events, and are finally combined into a single classifier.

In the current discussion we are treating photon-jets as the signal and both single photons and QCD-jets as background. We construct multiple BDT analyses in order to estimate how well the photon-jets can be separated from single photons *and* from QCD-jets. This will allow us to demonstrate the power of the new jet substructure variables when these are combined with the conventional variables. In practice, we employ the Toolkit for Multivariate Analysis (TMVA) [100] package and use the "BDTD" option to book BDTs, where the input variables are decorrelated first.

For every study point in Table 3.1 we optimize two separate BDTs, one for discriminating photon-jets form QCD-jets and the other for separating photon-jets from single photons. We make use of all the variables discussed earlier in order to minimize the background fake rate ($\mathcal{F}$ = the fraction of the background jets that pass the cuts) for a given signal

acceptance rate ($\mathcal{A}$ = the fraction of the signal jets that pass the cuts). For demonstration purposes we also consider BDTs made with a subset of the full set of variables. To be specific, we consider three different sets of variables:

$$\begin{aligned} D \equiv \Big\{ & \log\theta_J, \nu_J, \log\tau_1, \frac{\tau_2}{\tau_1}, \frac{\tau_3}{\tau_2}, \frac{\tau_4}{\tau_3}, \\ & \big(\lambda_J, \epsilon_J, \rho_J, \delta_J\big)\big|_{\mathrm{C/A}}, \big(\lambda_J, \epsilon_J, \rho_J\big)\big|_{k_T} \Big\} \end{aligned} \tag{3.13}$$

$$D_{\mathrm{C}} \equiv \Big\{ \log\theta_J, \nu_J \Big\} \tag{3.14}$$

$$\begin{aligned} D_{\mathrm{S}} \equiv \Big\{ & \log\tau_1, \frac{\tau_2}{\tau_1}, \frac{\tau_3}{\tau_2}, \frac{\tau_4}{\tau_3}, \\ & \big(\lambda_J, \epsilon_J, \rho_J, \delta_J\big)\big|_{\mathrm{C/A}}, \big(\lambda_J, \epsilon_J, \rho_J\big)\big|_{k_T} \Big\} , \end{aligned} \tag{3.15}$$

where the subscripts C/A or k_T in Eqs. (3.13) and (3.15) imply that the observables are calculated using C/A or k_T subjets. The sets D_{C} and D_{S} consist of the conventional and the jet substructure variables respectively, whereas D is the set of all variables.

In a previous paper [101] we described the more conventional separation of single photons from QCD-jets along with an initial introduction to the separation of single photons from photon-jets. In both cases the single photons were treated as the signal. Here we extend that discussion and focus on the photon-jets as the signal. We organize the results of our analysis into three subsections. First, we show the results of BDTs optimized to discriminate photon-jets from QCD-jets, the analogue of the seperation of single photons from QCD-jets. In the following subsection, we repeat the same study, but optimize it for treating single photons as the background to photon-jets. Finally, we demonstrate how the BDTs might be used for an effective three-way separation of single photons from photon-jets from QCD-jets.

QCD-Jets as Background for Photon-jets

We use all of the variables in the set of discriminants D in the BDTs in order to maximize the extraction of signal jets (photon-jets) from background (QCD-jets). This is similar to the separation of single photons from QCD-jets performed in Ref. [101]. The BDTs are trained individually for each study point. The results for fake rate versus acceptance are shown in figure 3.18 for all of the study points. In this plot the lower right is desirable and the upper left is undesirable. Note that the acceptance rate for photon-jets is bounded

above by about 0.94 due to our preselection cut $\theta_J \geq 0.25$ (see Section 3.5.4). The same cut eliminates approximately 98% of the QCD-jets yielding a fake rate below 10^{-2} except at the largest acceptance.

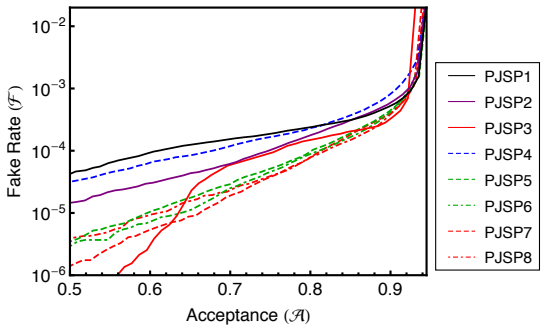

Figure 3.18: The background fake rate versus signal acceptance where photon-jets from the different study points are the signal and QCD-jets are the background. All variables in the set of discriminant D are used in the analysis.

For 2 photon photon-jets (study points 1 to 3) the separation becomes easier as m_1 increases yielding increasing separation between the photons inside the jet. The other physics scenarios tend to have even more structure within the photon-jets that the jet substructure variables allow us to use to suppress the QCD background. The more structure a jet possesses, the easier it becomes to discriminate it from (largely feature-less) QCD-jets. The conclusion from figure 3.18 is that, for photon-jets of varied kinematic features, we can achieve a very small QCD fake rate for a reasonably large acceptance rate. In more detail, for all of our study points a tagging efficiency (acceptance) of $\sim 70\%$ for photon-jets is accompanied by a fake rate for QCD-jets of only 1 in 10^4 to 1 in 10^5.

It is instructive to quantify the improvements made possible by including the jet substructure variables as discriminants. To achieve this comparison we consider BDTs using only the conventional variables (i.e., we use the set $D_{\rm C}$ of discriminants to train the BDTs). For a given acceptance of signal we thus obtain two different fake rates – one when we use only the conventional variables (labeled $\mathcal{F}_{\rm C}$), and another when we use conventional+jet

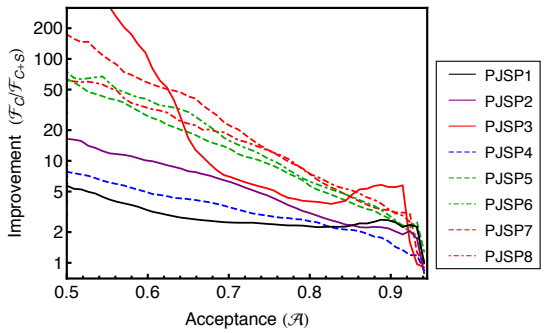

Figure 3.19: The improvement brought in because of the use of substructure variables are shown in the figure. For a quantitative definition of improvement see the text.

substructure variables (labeled $\mathcal{F}_{\mathrm{C+S}}$). For a given acceptance, the ratio $\mathcal{F}_{\mathrm{C}}/\mathcal{F}_{\mathrm{C+S}}$ quantifies the improvement due to using jet substructure variables in this analysis. The improvement rates for conventional plus jet substructure variables over only conventional variables versus acceptance for discriminating photon-jets from QCD-jets is shown in figure 3.19 for the different study points. While Figs. 3.11 and 3.12 indicate that the conventional variables provide some discrimination between photon-jets and QCD-jets, Figs. 3.13 to 3.17 indicate that the jet substructure variables provide a substantial number of new distinguishing features. Figure 3.19 shows that these new features in the jet substructure variables can provide substantial improvement. Factors of 4 to 50 improvement in the discrimination of photon-jets from QCD-jets are possible at an acceptance of about 70%. As expected more improvement is possible in those physics scenarios where the photon-jets have more structure. Further, our results demonstrate that the use of jet substructure variables provides a tool to distinguish the different physics scenarios, i.e., the different study points, which is not possible with conventional variables alone.

Single Photons as Background to Photon-Jets

Now consider the same analysis as in the previous section but with single photons treated as the background. This new sort of separation is essential if we want to consider physics scenarios with photon-jets. Again we use all of the variables in the set of discriminants D in

the BDTs in order to maximize the extraction of signal jets (photon-jets) from background (single photons). The BDTs are trained individually for each study point. The results for fake rate versus acceptance are shown in figure 3.20. As in figure 3.18 the lower right is desirable and the upper left is undesirable. Again the acceptance rate for photon-jets is bounded above by about 0.94 due to our preselection cut $\theta_J > 0.25$ (see Section 3.5.4). For the same reason a similar limit (0.94) holds also for the fake rate from single photons (although this is difficult to see on the logarithmic scale).

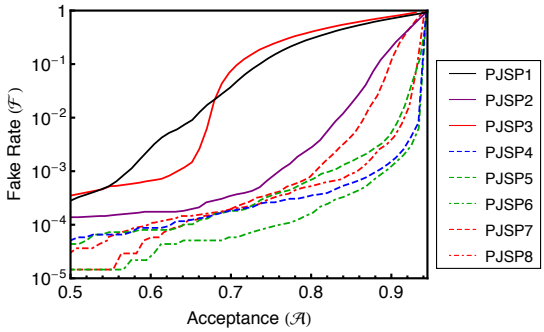

Figure 3.20: The background fake rate versus signal acceptance curves are shown for all study points. Here the photon-jets from the different study points are treated as the signal and single photons are the background. These curves employ all variables in the set of discriminants D.

The results in figure 3.20 teach us several lessons. A photon-jet from PJSP **1** consists of a pair of highly collinear photons. Such a jet is quite photon-like and thus difficult to separate from single photons. Hence the corresponding (solid black) curve is most towards the upper left. One needs to cut away almost half of the signal sample ($\mathcal{A} \sim 0.55$) in order to reduce the fake rate to 1 in 10^3. We also see that it is a challenge to separate the photon-jets for PJSP **3** from single photons (the solid red curve). In this scenario $m_1 = 10$ GeV and the n_1 decays directly to two photons. Because of the large m_1 value, almost 30% of these ($R = 0, 4$) jets do not contain both of the photons from the n_1 decay, i.e., about 30% of this jet sample are actually single photons (in the jet), and not photon-jets. We saw this point earlier in essentially all of the individual jet substructure variable plots, Figs. 3.13

to 3.17, where the PJSP **3** distribution exhibited an enhancement that overlapped with the corresponding peak in the single photon distribution. A larger separation of PJSP **3** from single photons can be obtained at an acceptance just below 0.7, where these single photons configurations are cut away and the fake rate drops below 1 in 10^3. The photon-jets of PJSP **2** represent a 'sweet' spot between PJSP **1** and PJSP **3** where the 2 photons are typically well enough separated to be resolved but close enough to be in the same jet. Thus the PJSP **2** (solid purple) curve is well below and to the right compared to the PJSP **1** (solid black) and PJSP **3** (solid red) curves. Similarly the photon-jets at the other study points can be well separated at even larger acceptance rates using the combination of jet substructure and conventional discriminants. For example, for the study points PJSP **4** and PJSP **6**, even at 85% acceptance, one obtains a fake rate *smaller* than 1 in 10^3.

Again it is instructive to determine the impact of the jet substructure variables for this analysis. As in the previous subsection we consider BDTs using only the conventional variables (i.e., we use the set $D_{\rm C}$ of discriminants to train the BDTs) to compare to the results from the full set D of variables. We plot the ratio of fake rates at fixed acceptance for these two analyses in figure 3.21 versus the acceptance. A comparison of figure 3.21 and

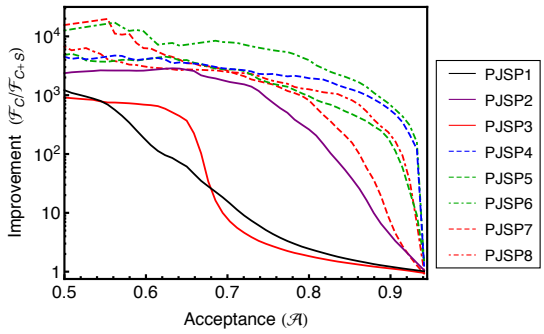

Figure 3.21: The improvement brought in because of the use of substructure variables are shown in the figure. For a quantitative definition of improvement see the text.

figure 3.20 indicates that the bulk of the separation of photon-jets from single photons is provided by the jet substructure variables, i.e., the improvement factor typically differs by less than a factor of 10 from one over the fake rate. Further, the improvement factor ranges

from 10 to more that 10^3 even at acceptances as large as 90% for all physics scenarios except PJSP **1** and PJSP **3**. Even in these challenging cases substantial improvement is possible at lower acceptance rates. This is not a surprise since the conventional variables are ineffective at distinguishing between photon-jets and single photons. Recall from figure 3.11 that the hadronic energy fraction distributions are nearly identical for photon-jets and single photons. The distribution of the number of charge tracks associated with a jet, shown in figure 3.12, also indicates only slight differences, arising from the somewhat different conversion rates for photon-jets versus single photons. So it is clear that, if we want to be able to discriminate between photon-jets and single photons (and we do), the jet substructure variables provide the necessary tool.

Three-way Separation

Finally we come to the really interesting challenge: the *simultaneous* separation all three samples: single photons, photon-jets, and QCD-jets. In principle, one could perform three BDT training exercises, separating photon-jets from single photons, separating photon-jets from QCD-jets and separating single photons from QCD-jets, using one of the variable sets of Eqs. 3.13 - 3.15 in each case. Then the responses from each of these BDTs for each jet could be used to separate the experimentally identified jets in the corresponding 3-dimensional 'physics object' space. In order to illustrate these ideas in a fairly simple analysis here we will focus on a two-dimensional analysis employing the two BDTs we have been discussing, separating photon-jets from single photons and separating photon-jets from QCD-jets. There are still the related questions of which set of variables to use for each BDT and, in fact, how to characterize the 'best separation'.[7] Qualitatively at least, we find good 2-dimensional separation for the following definitions of the BDTs. One is trained to separate QCD-jets and photon-jets based only on the conventional discriminants ($D_{\rm C}$) and is plotted on the vertical axis in the following plots, while the other BDT is trained to separate photon-jets from single photons with the substructure discriminants ($D_{\rm S}$) alone

[7]With three BDTs and the three BDT response numbers for each jet, the 'best separation' presumably corresponds to the three distinct physics objects being sent to three diagonally opposite vertices of the BDT response cube (on a equilateral triangle with side of length $\sqrt{2}$ times the length of the edge of the cube).

and is plotted along the horizontal axis. We present the results in terms of two-dimensional contour plots where the numerical values associated with a given contour corresponds to the relative probability to find a calorimeter object of the given kind (indicated by the color) in a cell of size 0.1×0.1 in BDT response units. (Note that, by construction, the BDT responses have values in the range -1 to $+1$, where $+1$ means 'signal-like' and -1 means 'background-like'.) The color coding in these figures matches the previous choices. Red is for QCD-jets, blue for photon-jets and green is for single photons.

As a first example, figure 3.22 indicates the 2-dimensional distributions resulting from the BDTs for PJSP **2**, a scenario with typically two photons in the photon-jet with small angular separation due to the small value of m_1. When interpreting the following figures it is important to recall that the jet samples indicated in these figures are constrained to satisfy $\theta_J \leq 0.25$, which means that we are only keeping the approximately 2% of QCD-jets that are most 'photon-like'. However, figure 3.22 indicates a pretty clear separation between the

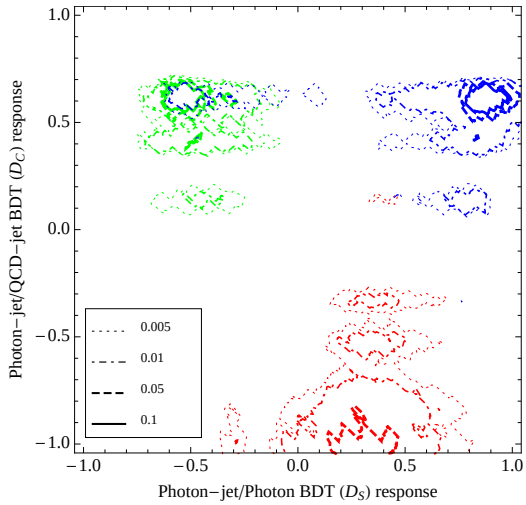

Figure 3.22: The BDT responses of QCD-jets(red), single photons(green) and photon-jets(blue) for photon-jets at PJSP **2**. The D_S variables are used on the horizontal axis and the D_C variables on the vertical axis.

QCD-jets and the true photon objects (little red above 0.0 in the vertical direction). On the

other hand, as we expect from our previous one-dimensional discussions in Subsection 3.5.4, the blue (photon-jet) contours in the upper-left green (single photon) region indicate that it is a challenge to completely separate (PJSP **2**) photon-jets from single photons.

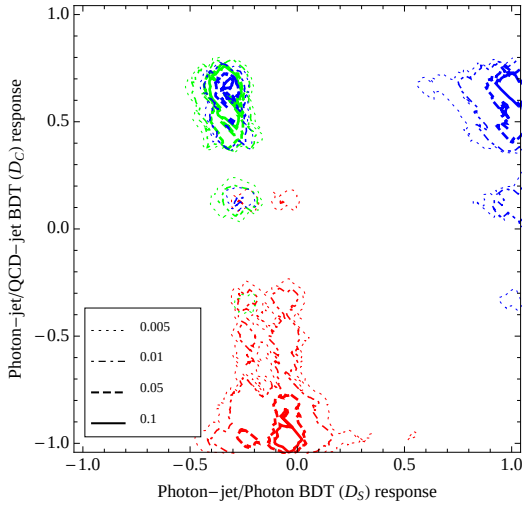

Figure 3.23: The BDT responses of QCD-jets(red), single photons(green) and photon-jets(blue) for photon-jets at PJSP **3**.

In the case of PJSP **3** photon-jets, as indicated in figure 3.23, the photon-jet versus single photon separation challenge is even larger, as we have already discussed. Again we have photon-jets with potentially two photons but, due to the relatively large m_1 value, one of those photons is sometimes outside of the identified jet. This explains the small region with a solid blue (probability 0.1) contour inside the green (single photon) region.

The corresponding results for the more complex (and more easily separated) photon-jets of PJSP **4** and PJSP **8**, typically with 4 photons in a photon-jet, are displayed in Figs. 3.24 and 3.25. In these scenarios the three-way photon-jet versus single photon versus QCD-jet separation is fairly cleanly achieved using just the D_S (horizontal) and D_C (vertical) variable sets. At the 0.005 level there is only a tiny overlap of photon-jets with QCD-jets for PJSP **4** (near the location (0.5,0.0) in figure 3.24) and no overlap for PJSP **8** (figure 3.25).

Before ending this section we should discuss one other point. From our previous discus-

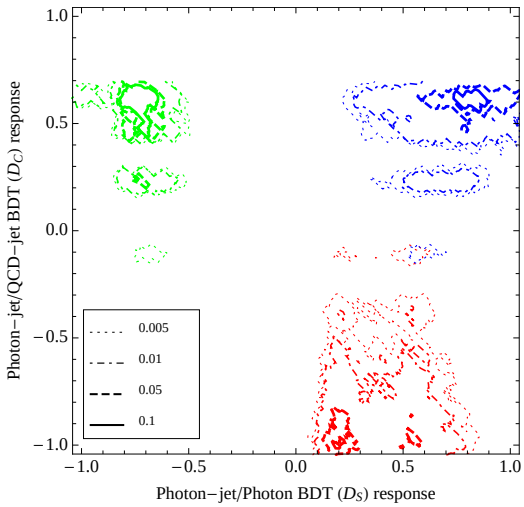

Figure 3.24: The BDT responses of QCD-jets(red), single photons(green) and photon-jets(blue) for photon-jets at PJSP **4**.

sion, one would expect to improve the photon-jet versus single photon separation by using the full D set of variables (instead of the D_S variables alone), and this expectation raises one of the interesting, and challenging, features of *simultaneous* separations. Since we are currently training the BDTs so that each BDT separates one type of signal from one type of background, while, at the same time, trying to perform a three-way separation, it can happen that an improvement in one separation corresponds to a degradation in another of the separations. To illustrate this point we first reproduce the results in figure 3.23, but now include a contour at relative probability 0.001, which we did not include earlier to avoid plots that are too busy. The resulting plot is shown in figure 3.26. Now we perform the same analysis but using the full variable set D in both BDTs. The resulting contour plot is displayed in figure 3.27, which illustrates the relevant points. The 0.001 level boundaries for single photons (green) and photon-jets (blue) are now somewhat better separated, although the effectively one-photon-jets from PJSP **3** (when one of the photons is very soft or is outside of the jet) still lie within the single photon boundary. At the same time, however, the separation between single photons (green) and the (typically more numerous) QCD-jets

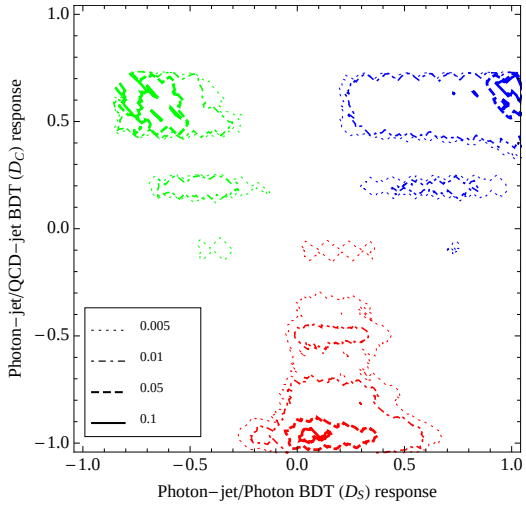

Figure 3.25: The separation of QCD-jets (red), single photons (green) and photon-jets(blue) for photon-jets at PJSP **8**.

(red) is somewhat degraded (the green and red regions have moved towards each other). Due to the coupling between the different pairwise separations, optimizing such a three-way separation takes careful work and likely depends on the details of the actual analysis and detector.

These results clearly suggest that a three-way separation is possible, including the ability to distinguish different photon-jet scenarios. Further enhancement will arise from using the full 3-dimensional structure and from using a realistic detector simulation in the training. A thorough optimization in the context of a real detector and actual data may select different, more effective choices of the discriminating variables.

3.5.5 Conclusion

In this paper we have attempted to link several concepts, some conventional and some less so, with the goal of enhancing the searches for and the analyses of both Standard Model and Beyond the Standard Model physics. We advocate employing general techniques for analyzing and interpreting the detector objects identified by applying standard jet algorithms

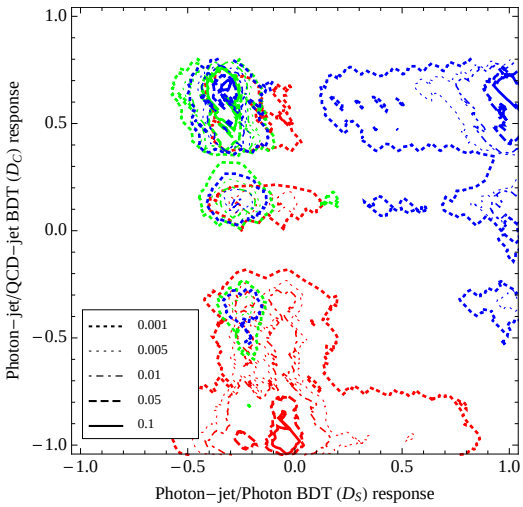

Figure 3.26: The BDT responses of QCD-jets(red), single photons(green) and photon-jets(blue) for photon-jets at PJSP **3** including a contour at 0.001.

to the calorimeter cells of typical hadron collider detectors, allowing a universal language for such objects. We have demonstrated the efficacy of employing the recent developments in jet substructure techniques to separate and identify these detector objects in terms of physics objects. Continuing the efforts begun in Ref. [101], we have focused on identifying three specific physics objects, the familiar single photons, QCD-jets and the Beyond the Standard Model (and LHC) relevant photon-jets. In particular, we have demonstrated that it is possible to achieve significant separation between photon-jets and their dominant backgrounds, i.e., single photons and QCD-jets. We expect that both the ATLAS and CMS groups could enhance their searches for signatures of New Physics by adopting the methods described. These methods should allow the separation of photon-jets from single photons from QCD-jets, and also provide some identification of the specific dynamics yielding the photon-jets.

We note that our simulation does not take into account the impact of magnetic fields inside the detectors. On the other hand, one might interpret this absence of a magnetic field as making our results more conservative. When the magnetic field bends the electrons

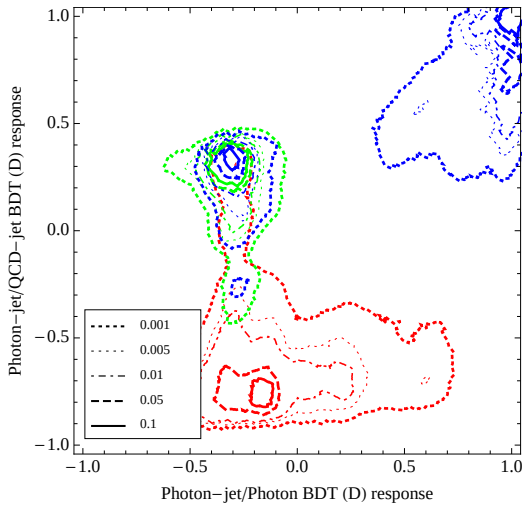

Figure 3.27: The BDT responses of QCD-jets(red), single photons(green) and photon-jets(blue) for photon-jets at PJSP **3** using the full set D of variables on the horizontal axis.

and positrons from converted photons, this serves to generate more structure inside the jet. The substructure variables, as we have described, tend to become more powerful with more structure. A more detailed analysis is, however, beyond the scope of this paper.

Finally, it is worth mentioning that the formalism and techniques developed in this paper for photon-jets should work in a similar way for the case of collinear electrons, often labeled 'electron-jets' [102–105]. An electron-jet is characterized by a large number of charged tracks along with a small hadronic energy fraction. Also, we expect the electrons inside these jets to bend in a magnetic field, creating more substructure. Therefore we anticipate that multivariate analyses similar to those described here will be correspondingly effective at separating electron-jets from QCD-jets (and photon-jets).

3.5.6 Technical Details

Conversions

In the material of the detector photons convert into electron-positron pairs. Our implementation of photon conversion is based on the properties of the ATLAS detector [45]. We associate an η dependent probability of conversion with every photon. This probability is a function of the number of radiation lengths a photon passes through (labeled $n(\eta)$) in order to escape the first layer of the pixels. We model the probability to convert using the expression:

$$P(\eta) = 1 - \exp\left(-\frac{7}{9}n(\eta)\right) , \tag{3.16}$$

where the factor of $7/9$ comes from conversion between radiation length and mean free path. A plot of the extracted radiation length profile of the inner pixel detector in the ATLAS detector that we use to determine $n(\eta)$ is displayed in figure 3.28. The yellow-black dashed

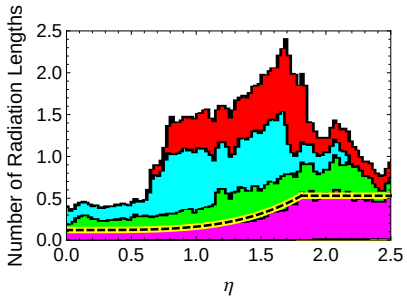

Figure 3.28: Number of radiation length up to and through the layer of pixel detectors in the ATLAS detector.

line shows the extracted η-dependent number-of-radiation-lengths a photon needs to travel before it exits the pixel layer. If the photon converts before the dashed line, it is treated as a charged track, otherwise no charged track is included in our simulation.

Details of the Calorimeters

Our simulation of calorimeters closely resembles the calorimeters implemented in the widely used simulation tool PGS [106]. The electromagnetic calorimeter ECal covers $|\eta| \leq 2.5$ in the

pseudorapidity direction, whereas the hadronic calorimeter HCal covers the range $|\eta| \leq 5.0$. Both of the calorimeters provide a full 2π coverage in ϕ, the azimuthal direction. The ECal has granularity of 0.025×0.025 in the η-ϕ plane. The HCal, on the other hand, has a coarser granularity with cells of size 0.1×0.1.

We assume that all particles generated at the interaction point (i.e., the Pythia output), except charged particles with energy less than 0.1 GeV, reach the ECal. Photon/electrons within $|\eta| \leq 2.5$ deposit 99% of their energy in the ECal and the rest in the HCal. The ECal also fully absorbs hadrons with energy less than 0.5 GeV. For more energetic hadrons, 0.5 GeV is deposited in the ECal and the rest in the HCal. Photon/electron/hadrons that lie outside the pseudorapidity range of the ECal but within the range of the HCal (i.e., $5.0 \geq |\eta| > 2.5$) are completely absorbed in the HCal.

In our simulation, muons also deposit energy in the calorimeters. Within the range $|\eta| \leq 2.5$, muons with $E < 0.5$ GeV deposit all of their energy in the ECal; muons with 0.5 GeV $< E <$ 2.5 GeV deposit 0.5 GeV in the ECal and the rest in the HCal; muons with $E >$ 2.5 GeV deposit 0.5 GeV in the ECal and 2.0 GeV in the HCal. For muons within the rapidity range $5.0 \geq |\eta| > 2.5$, those with $E <$ 2.0 GeV are fully absorbed in the HCal, while muons with $E >$ 2.0 GeV deposit 2.0 GeV in the HCal.

Moliere Matrix

In order to simulate the transverse smearing in the ECal, we deposit the energy of each particle not just into the specific cell through which it passes, but also into the surrounding cells. The (η-ϕ) coordinates of a particle determine the cell in which it deposits most of its energy (call it the (i, j)-th cell in the grid). We distribute its energy in the neighboring cells according to the following table:

	i-1	i	i+1
j-1	0.00(4)	0.01(4)	0.00(4)
j	0.01(4)	0.92(4)	0.01(4)
j+1	0.00(4)	0.01(4)	0.00(4)

We estimate these numbers by integrating the energy deposited in an electromagnetic shower in a cell of size (0.025×0.025) and situated 1.5 m from the origin of the shower. We assume that the cell is made of lead ($R_M(\text{Pb}) = 1.6$ cm) .

3.6 Future Directions

This projects has several possible future directions. Since both photons and electrons are massless in the collider environment the analysis of multi-photon final state is easily translated into analysis of multi-electron final state (Lepton Jets). Doing so would require to investigate the dominant multielectron backgrounds as well as re-evaluate the only variable that changes significantly: the number of charged tracks inside the jet. The hadronic fraction θ_J and the number of charged tracks ν_J are correlated for the QCD dijet sample because a QCD jet achieves a large electromagnetic fraction by increasing its π^0 content, therefore decreasing the number of its charged tracks. This means that the QCD jet background should be easier to separate from Lepton Jets.

From the different substructure variable plots it is evident that the signal is less sensitive to the jet-algorithm that was used to identify its substructure. This should not be a surprise since Photon Jets have a clear hierarchy of scales while QCD has a more complex showering structure. The idea of algorithm dependence has already been explored in other contexts in Q-Jets [97]. However, it is possible that a single variable could be more practical. One such variable, κ, has a simple structure: each constituent four-vector has $\kappa = 0$ at the beginning of the clustering. As four-vectors v_i, v_j get merged, the resulting four-vector has $\kappa = \kappa_i + \kappa_j + d_{ij}^{kt}$, where d_{ij}^{kt} is the k_T distance measure between v_i and v_j. This variable is IR safe. Whether this variable κ can be used to separate signal with hard splitting structure and fuzzy QCD background is a question that warrants future research.

Chapter 4

INTENSITY FRONTIER: HIDDEN SECTOR & HEAVY FLAVOR

4.1 Introduction

This project is based on a Hidden Sector that is nearly identical to the Hidden Sector from the previous chapter. It contains two scalars with masses on the order GeV or smaller, both of which mix with the Higgs boson. As a result, these scalars, n_1 and n_2, can decay into pairs of leptons as well as Standard Model mesons such as pions and kaons. One could be tempted to follow the reasoning of the previous chapter and look at multi-muon, multi-electron or multi-pion decays of the Higgs boson. Indeed, collimated multi-muon and multi-electron decays are muon-jets, electron-jets, or collectively, lepton-jets and some amount of research has already been invested in this field [4, 103, 107]. However, the Higgs portal does not influence only the decays of the Higgs particle. There are many other particles whose decays could proceed through a spin-0 singlet, one such example would be B mesons.

4.2 B quarks and B mesons

Quarks, the building blocks of mesons and baryons, come in three generations. Each generation has two flavors. Table 4.2 summarizes the flavors, generations and properties of these quarks. The unstable quarks decay through weak interactions via $q_i \to q_j W^{\pm}$. This vertex is proportional to the weak coupling and the corresponding element of the Cabibbo-Kobayashi-Maskawa (CKM) matrix V_i^j. Surprisingly this matrix is very close to a unit matrix – the couplings for transition within the same generation are nearly one, the transi-

Generation	Flavor	Quark	Charge	Mass ($\bar{MS}$)
I	up	u	$+2/3$	~ 2 MeV
	down	d	$-1/3$	~ 5 MeV
II	charm	c	$+2/3$	1.3 GeV
	strange	s	$-1/3$	~ 95 MeV
III	top	t	$+2/3$	173 GeV
	bottom	b	$-1/3$	4.2 GeV

Table 4.1: Standard Model quarks

tions between generations are small:

$$|V_{CKM}| = \begin{pmatrix} |V_{ud}| & |V_{us}| & |V_{ub}| \\ |V_{cd}| & |V_{cs}| & |V_{cb}| \\ |V_{td}| & |V_{ts}| & |V_{tb}| \end{pmatrix} \sim \begin{pmatrix} 0.974 & 0.225 & 0.0035 \\ 0.225 & 0.973 & 0.041 \\ 0.0087 & 0.04 & 0.999 \end{pmatrix} \tag{4.1}$$

As a result, the lighter quark in each generation are relatively long lived compared to their heavier partner. Subsequently, the mesons built out of these quarks can also have a relatively long lifetime. For example the neutral B meson $B^0 = B_d$, which corresponds to a bound state of $\bar{b}d$, has a lifetime of $\tau = 1.4 \times 10^{-12}$ s. This is comparable to the lifetime of its lighter cousin, the D_0 (a bound state of $\bar{c}u$). In order to appreciate the length of this lifetime, it is useful to compute the average distance a B meson can travel before it decays. Even moderately boosted[1] B_d has $v\gamma\tau = c\tau = 0.4$ mm, which is an achievable detector resolution. As a result, a B meson can be identified by a set of tracks that do not point towards the original IP, but towards the point where the B meson decayed. Such a vertex is called a displaced vertex.

4.3 Flavor Structure of the Standard Model

Where does the flavor structure of the CKM matrix come from? After the Electro-Weak symmetry breaking the Standard Model interactions between the Weak bosons, the Higgs

[1]By moderate boost I mean $v = c\sqrt{2}$ so that $v\gamma \sim c$.

boson and the quarks look simple:

$$\mathcal{L} = \ldots + y^u_{ij}(h+v)\bar{u}^i_R u^j_L + y^d_{ij}(h+v)\bar{d}^i_R d^j_L + W^+_\mu \bar{u}_L \gamma^\mu d_L + Z_\mu \bar{u}_L \gamma^\mu u_L + Z_\mu \bar{d}_L \gamma^\mu d_L + \ldots + h.c. \tag{4.2}$$

From our perspective, the matrices y^u_{ij} and y^d_{ij} are unconstrained and determined by some unknown UV physics. Since the terms $y_{ij} v q^i_R q^j_L$ are the sole sources of mass for quarks, finding a basis in which y^u_{ij} and y^d_{ij} are diagonal is equivalent to finding the quark mass eigenstates. Note that y^u_{ij} and y^d_{ij} are linear transformations between two non-identical spaces. The y^u_{ij} is a map between the space of the left handed up-quarks and the space of the right-handed up-quarks. By choosing four change of basis matrices $V^u_L, V^d_L, V^u_R, V^d_R$, we can diagonalize y_{ij}'s:

$$u^i_L \to (V^u_L)^i_j u^j_L \tag{4.3}$$

$$d^i_L \to (V^d_L)^i_j d^j_L \tag{4.4}$$

$$u^i_R \to (V^u_R)^i_j u^j_R \tag{4.5}$$

$$d^i_R \to (V^d_R)^i_j d^j_R \tag{4.6}$$

$$y^u \to (V^u_R)^\dagger y^u (V^u_L) = \mathrm{diag}(y_u, y_c, y_t) \tag{4.7}$$

$$y^d \to (V^d_R)^\dagger y^d (V^d_L) = \mathrm{diag}(y_d, y_s, y_b) \tag{4.8}$$

This turns the Lagrangian from equation 4.2 into:

$$\mathcal{L} = \ldots + \sum_i y_i (h+v)\bar{u}^i_R u^i_L + \sum_j y_j (h+v)\bar{d}^j_R d^j_L + W^+_\mu (V^u_L)^\dagger V^d_L \bar{u}_L \gamma^\mu d_L + \\ + Z_\mu \bar{u}_L \gamma^\mu u_L + Z_\mu \bar{d}_L \gamma^\mu d_L + \ldots + h.c. \tag{4.9}$$

Notice that in the quark mass eigenbasis the neutral Higgs bosons, the Z bosons, photons and gluons couple to each generation of quarks independently. This is the source of the statement that there are no flavor changing neutral currents (FCNCs) in the Standard Model at the tree-level. You can see that charged W bosons interact with two different flavors and are responsible for decays of heavier quarks into lighter quarks. We can also see the origin of the CMK matrix from equation 4.9:

$$V_{CKM} = (V^u_L)^\dagger V^d_L \tag{4.10}$$

This does not explain why the CKM matrix is so close to a unit matrix. It may be that both V_L^u and V_L^d are not far from a unit matrix (replacing one almost identity matrix by two almost identity matrices). or it may imply that neither V_L^u and V_L^d are close to an identity matrix but when combined they nearly undo each other (which calls for some link between the up and down sector). Since we did not introduce any new UV physics yet and so there is no reason to gain any insight into the form of y_{ij}^u and y_{ij}^d.

4.3.1 Loop Corrections

Just because there are no tree-level FCNCs in the Standard Model does not mean there are no FCNCs at all. Consider the following loop diagram the likes of which were first studied by authors of [108]:

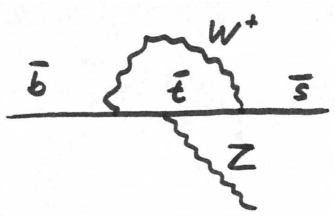

This diagram gives rise to flavor changing operators that couple to the neutral current $O(q^2) = c_1\Lambda_1^{-1}\bar{b}\sigma_{\mu\nu}sZ^{\mu\nu}$. We can choose to set the renormalization condition such that $O(q^2) = 0$ for a particular scale $q^2 = \Lambda^2$, but we cannot suppress this operator to be zero at every scale. Similarly, we can also construct another diagram:

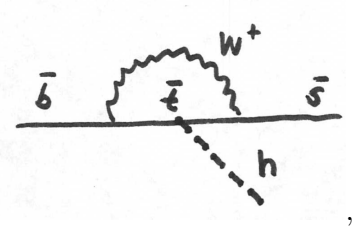

,

which couples the neutral Higgs boson to a flavor changing combination of quarks through $O = c_2\Lambda_2^{-1}(\partial_\mu h)\bar{b}\gamma^\mu s$. All these loop diagrams are called the Penguin diagrams[2] because of how they look when the Z boson couples to another quark line:

[2]Supposedly the term was used by John Ellis after he lost a bet in a darts game with Melissa Franklin. [109]

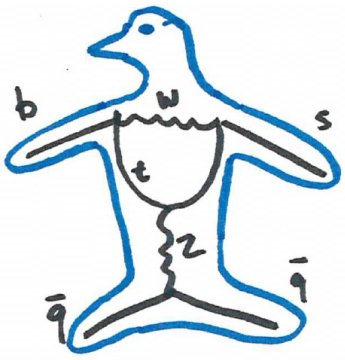

4.3.2 Rare Decays

As we have seen, some processes (such as $b \to s$) do not occur at the tree-level in the Standard Model. This implies that they are suppressed by the usual suppression factors that come with one-loop diagrams. As a result, effects of New Physics particles that enable such processes, either by allowing direct tree-level transitions or by interfering with the Standard model process in the loop, would be far more visible in comparison to tree-level Standard Model processes. We seek out Standard Model processes with low partial widths in hopes that New Physics would be most visible in these channels. In B physics such decays are called rare decays. One of the most famous rare decays of this season are $B_d \to \mu\mu$ and $B_s \to \mu\mu$. Their branching rations are predicted at $\sim 10^{-10}$ and 3.23×10^{-9} levels. At this point in time $B_s \to \mu\mu$ is observed at 4σ, while $\mathcal{B}(B_d \to \mu\mu)$ is constrained below 7.4×10^{-10} [110]. You will see that our paper focuses on rare decays of B_d and B_s and uses them to constrain several parameters of our model.

4.4 Neutral Meson Oscillations

The neutral mesons such as B_d^0 and $\bar{B}_d^0$ or B_s^0 and $\bar{B}_s^0$ have the same quantum numbers, so a B_q^0 can oscillate into $\bar{B}_q^0$ and vice-versa (for $q = (d, s)$). There are several one-loop Standard Model processes (shown in figure 4.1) that are responsible for these transitions. These processes are an ideal place to observe contributions from New Physics because they are suppressed by loop factors just as the rare processes in the previous paragraph.

The Ws can be integrated out and the resultant four-quark operators $\bar{b}\bar{b}qq$ and $\bar{q}\bar{q}bb$ can

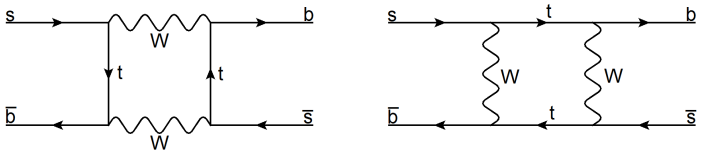

Figure 4.1: Lowest order Standard Model processes responsible for $B_s - \bar{B}_s$ mixing.

be interpreted as contributions to the mass terms $\bar{B}_q\bar{B}_q$ and B_qB_q. Together with the usual mass operator $\bar{B}_qB_q$ these contribute to the effective Hamiltonian:

$$H_{eff} = \begin{pmatrix} B_q^0 & \bar{B}_q^0 \end{pmatrix} \begin{pmatrix} M_{11} i\frac{\Gamma_{11}}{2} & M_{12} - i\frac{\Gamma_{12}}{2} \\ M_{21} - i\frac{\Gamma_{21}}{2} & M_{22} - i\frac{\Gamma_{22}}{2} \end{pmatrix} \begin{pmatrix} B_q^0 \\ \bar{B}_q^0 \end{pmatrix}, \tag{4.11}$$

where both M_{ij} and Γ_{ij} are hermitian. This makes $i\Gamma_{ij}$ an anti-hermitian operator responsible for decays of both B_q^0 and $\bar{B}_q^0$. The CPT invariance enforces $M_{11} = M_{22}$ and $\Gamma_{11} = \Gamma_{22}$. Further more by definition $\Gamma_{12} = \Gamma_{21}^*$ and $M_{12} = M_{21}^*$.

As long as $M_{12} \neq 0$ or $M\Gamma_{12} \neq 0$ the states B_q^0 and $\bar{B}_q^0$ are not the eigenstates of this Hamiltonian. The heavier eigenstate is called $|M_H\rangle$ while the lighter is $|M_L\rangle$:

$$|M_H\rangle = p|B_q^0\rangle + q|\bar{B}_q^0\rangle \tag{4.12}$$

$$|M_L\rangle = -q|B_q^0\rangle + p|\bar{B}_q^0\rangle \tag{4.13}$$

Since $M - i\Gamma/2$ is not a Hermitian matrix, the eigenstates are not necessarily orthogonal. Inverting this relation tells us that each flavor eigenstate is a linear combination of mass eigenstates and just like neutrinos, these oscillate. As a result, it is possible to produce a B_q^0 state and at later time observe a $\bar{B}_q^0$ state. One can solve for the ratio of q/p as it was done in [111]:

$$\left(\frac{q}{p}\right)^2 = \frac{M_{12}^* - (i/2)\Gamma_{12}^*}{M_{12} - (i/2)\Gamma_{12}} \tag{4.14}$$

In the Standard Model, the phases of Γ_{12} and M_{12} are very similar, which implies that $|q/p| \sim 1$. Therefore the oscillations are maximal – in other words if one can wait long enough the chance to observe $\bar{B}_q^0$ after producing B_q^0 is 100%.

Can one really wait long enough? The oscillation time is determined $\Delta m_q = m_H - m_L \sim$

$2M_{12}$, while the B mesons decay in Γ_q^{-1}. The ratio of these scales is called

$$x_q = \frac{\Delta m_q}{\Gamma_q}. \tag{4.15}$$

In the B_d system this ratio is relatively small: $x_d = 0.77$, which means that the B_d system barely oscillates once before it likely decays. However, the for the B_s system $x_s \sim 26.5$, which means that it is possible to observe many oscillations of a B_s system before it decays. Moreover, not only is there difference Δm_q but also the difference $\Delta\Gamma_q$, which allows the contributes towards different lifetime of the eigenstates. This means that B_q systems offer additional wealth of measurements that are sensitive to New Physics contributions. A reader interested in learning more about neutral meson oscillation can find an accessible and broad introduction in the section "CP violation in meson decays" of [111]. In order to measure all of these properties it is necessary to achieve great spatial and temporal resolution in order to be able to detect all of these oscillations. I will describe how this is done in the next section.

4.5 B factories

In order to study $B - \bar{B}$ oscillations as well as rare decays of B mesons, we need a large sample of B mesons. Although we produce some b quarks at high energy accelerators this is not always sufficient to probe the very rare decays or significantly constrain CP violation. These tasks call for specialized high luminosity machines: the B factories.

The latest generation of B factories are represented by BaBar [112] and Belle [113]. Both of these experiments work on very similar principle. This thesis will describe the BaBar experiment. A reader who would like to learn more can review the collaboration detector paper [114]. There is also a newer machine in the LHC facility called the LHCb [115]. Since it is based on a proton-proton beam with $\sqrt{s}7$ TeV, its physics is slightly different and will not be covered in this gentle introduction.

The BaBar collider supplies two beams. The first, High Energy Ring, contains 9.0 GeV electrons and the second, Low Energy Ring, contains 3.1 GeV positrons. These energies are tuned so that the center-of-mass energy $\sqrt{s} = 10.58$ GeV corresponds to the mass of the $\Upsilon(4s)$ meson. This unstable meson decays into a pair of B mesons almost immediately.

Since the Υ is on resonance, the cross-section for $e^+e^- \to \Upsilon(4s) \to B\bar{B}$ is greatly enhanced. This is what allows B factories to produce such large samples of B mesons.

Why should the two beams have asymmetric energies? For one it is easier to produce a high energy electron beam and lower energy positron beam. However, there is a much more important reason. If the two beams had the same energy the Υ would be produced at rest in the detector frame. The mesons would then also be nearly at rest, because the $\Upsilon(4s)$ mass is just slightly more than twice the mass of the B meson. In order to measure the lifetime of B mesons, the detector would have to achieve a fantastic time resolution on the order of picoseconds. On the other hand, with the momentum imbalance in the beams the Υ is moving with $\beta\gamma = 0.56$, which means that the average B decays after traveling about 0.2 mm. Even this slow drift allows turning delicate timing information into a more robust spatial difference. This is what allows the fantastic resolution that is necessary to measure B meson oscillations.

Since the B mesons are produced at moderate boosts, the total available energy for the decay products of the B mesons is not large; less than a couple GeV. As a result, B factory detectors must excel at resolving low momentum tracks with exceptional accuracy. The guiding principles in building such detectors are similar to those behind more general purpose experiments such as ATLAS, but with added stress on low energy precise measurements.

Due to the asymmetry in the beam setup, the detector does not have to be symmetric. The coverage in the direction of the slower (positron) beam is not as extensive as in the direction of the higher energy (electron) beam. Nevertheless, the coverage is still fairly close to 4π. As in the ATLAS machine, the detector is subdivided into subdetectors. In BaBar these subdetectors are: Silicon Vertex Tracker, Drift Chamber, Detector of Internally Reflected Cerenkov radiation, Electromagnetic Calorimeter and Instrumented Flux Return.

The Silicon Vertex Tracker (SVT) works on the same principle as the Silicon Tracker in the ATLAS detector. It is designed to detect charged tracks with as little material as possible, because low energy particle tracks are particularly vulnerable to scattering in the material of the detector. Moreover, the information from the SVT is used to determine not only the momentum of the particle, but also the rate at which it is losing energy (dE/dx),

which further improves particle identification.

The Drift Chamber (DCH) consists of many gas filled tubes with an electrode running in the middle. As a charged particle flies through the gas it ionizes some of its molecules. These ions are then pulled towards an electrode. The timing and amount of ions can be translated into a detailed position and type of particle passing through the gas. Not surprisingly a similar device is also a part of the ATLAS detector.

The Detector of Internally Reflected Cerenkov radiation (DIRC) consists of a set of thin quartz bars. As a particle passes through these plates it radiates Cerenkov radiation with the angle between the particle direction and the radiated photons dependent on the particle's speed in the quartz. These photons are totally internally reflected towards the end of the bar, which is optically coupled to a water tank with photomultipliers. Since internal reflection preserves the angle of the initial radiation, our experimental colleagues can measure the speed of the particle. Knowing both speed and momentum pins down the mass of a particle, which greatly improves particle identification.

The Electromagnetic Calorimeter (EMC) is mainly used to identify neutral particles such as photons and neutral pions that are invisible to all the previously mentioned subdetectors. as well as precisely measure the energy of incoming electrons. Hadrons are likely to pass through the detector without depositing much energy. But most of these hadrons are charged or decayed into charged remnants and therefore visible.

The Instrumented Flux Return (IFR) fulfills two purposes. It acts as a magnetic field line return yoke, concentrating the magnetic field lines throughout the detector. Since it consists of big slabs of iron it can be used as a muon detector by inserting smaller detectors that detect radiation caused by muons and charged pions striking the iron in the return yoke. Muons produce less radiation than charged pions and therefore can be separated by the IFR.

Now that the reader has had a short introduction into experimental and theoretical B physics and has obtained basic appreciation for the challenges of the field I introduce a project that is yet to be published. Although this work is in its final stages of preparation, it is possible that its printed form will undergo some (hopefully) minor changes.

4.6 Hidden Sector & Heavy Flavor

4.6.1 Introduction

The last decade has seen an explosion of available measurements performed on the B_d and B_s meson systems. Their masses, mass differences, lifetimes, branching ratios of common and rare decays, asymmetries in their decays are all well measured. Unfortunately, there are very few deviations from the predictions put forth by the Standard Model of Particle Physics, despite the effort poured into new sophisticated calculational methods devised to interpret this data [116–118]. With so few observed deviations we are forced to wonder: Is this it? Is there any more physics we can extract out of B mesons?

In other fields, such as Cosmology, we face puzzles of a different kind: A large body of evidence points towards the existence of Dark Matter (DM) as a significant ($\sim 25\%$) component of our Universe. We know very little about Dark Matter: most of it is cold (from structure formation) and it interacts very weakly with itself (halo formation, bullet cluster) and with baryonic matter (direct detection, bullet cluster). The weakness of interaction between Dark Matter and Standard Model (SM) particles justifies a separation of these two sectors. We will call the sector containing Dark Matter the Dark Sector (DS).

Although we know very little about Dark Matter, we know even less about the Dark Sector. The principle of Occam's Razor drives us towards the simplest theories of the Dark Sector with no additional particle content beyond what is necessary to explain the Dark Matter density of our Universe. However, this directly contradicts the nature of the Standard Model – the degrees of freedom of the Standard Model far outnumber the degrees of freedom that participate in forming the 5% of the Universe populated by baryonic matter. We must conclude that minimalism is a poor description of reality.

In this paper, we abandon minimalism and propose there are other fields and particles within the Dark Sector that do not contribute to the Dark Matter density of our Universe. There are a few reasons why only some Dark Sector particles might contribute significantly to Dark Matter density: some particles may freeze out at too low density, some might be too light to form a cold enough component of Dark Matter during the epoch of structure formation and some particles might be unstable on cosmological scales.

So far, the particles that form Dark Matter remain unobserved by direct detection experiments. Therefore, we wish to focus on the unstable particles that decay too fast and do not contribute to the Dark Matter density. If their lack of stability comes from decay into pairs of Standard Model particles, we have a chance of observing their decay products in our detectors.

Luckily, we have been given a physical system that is extremely sensitive to the existence of new decay channels. The B mesons, with their relatively long lifetimes and low enough mass, are ideally suited for probing GeV scale Dark Sector. Moreover, as already mentioned, these systems are very well explored by many dedicated experiments such as Belle, BaBar and LHCb as well as general purpose such as ATLAS and CMS. It would be a shame not to use this vast amount of experimental data to constrain the possible shape of the Dark Sector.

However, there are many different realizations of possible Dark Sector models and it is impossible to rule out all, or even a fraction of these models. In fact, a complete decoupling between the Standard Model and the Dark Sector is a logical possibility that does not contradict any current experimental data yet is impossible to rule out without a positive signal from the Dark Sector. Therefore, instead of focusing on constraining every corner of the Dark Sector model space, it would be far more fruitful to focus on describing possible signals that could arise as consequences of these models. This way we can alert the experimental community to measurements that may shed some light on the nature of these models. This approach is often called exploring the signal space, as opposed to exploring the model space.

Since we explore the B meson systems, it makes sense to explore an effective field theory of the Dark Sector with a cut off on the order of B meson mass ($\sim$ 5 GeV). In order to extract some interesting signals out of our Dark Sector, we have chosen to populate it with two scalars with internal couplings approaching a strongly coupled regime. If we wish, we can interpret these scalars as bound states of a strongly interacting theory or elementary scalars. In order to allow for some coupling between the two sectors, we include operators that contain both the Higgs fields and the Dark Sector scalars – the so called Higgs Portal [1, 3, 4].

We chose to include not just one Standard Model Higgs field, but two Higgs Doublets

[119]. This allows our models to be included not only within the Minimal Supersymmetric Standard Model (MSSM) frame work, but also allows us to use the decoupling limit which corresponds to the Standard Model with one Higgs field.

We discover that within our framework it is remarkably simple to significantly change the rate of rare decays of B mesons, in particular the decays into multi-particle final states. Depending on the parameters of our model these decays may appear prompt, or with displaced vertices. Finally, irrespective of including second Higgs doublets, light Higgs-like scalars preferentially couple to mesonic final states which motivates many new searches.

This paper is organized as follows: we will set up our model and establish our conventions and notation in section 4.6.2. We will present a UV completion of this model in section 4.6.3. In section 4.6.4 we will discuss the interaction between the Standard Model and the Dark Sector. We will explore the experimental and theoretical constraints on our model in section 4.6.5 and show the allowed branching fractions for high multiplicity decay modes of B mesons in section 4.6.6. We finally conclude and suggest future directions in section 4.6.7.

4.6.2 Definitions, Notation and Setup

The Model

We will extend the Standard Model in two ways. First, we use a more complicated Higgs sector with two Higgs doublets. This is is a well known extension thanks to its presence in supersymmetric models. For the second extension, we take the simplest non-trivial low energy effective theory of the Dark Sector: two scalars both with masses on the order of GeV. We make no effort to make either of the scalars a good candidate for Dark Matter and in fact they will not be. We expect that all other dimension-full constants in this effective theory will be generated by the same processes and therefore will be roughly the same scale. The SM sector and the Dark sector will be coupled through a Higgs Portal [1, 3, 4] – a set of renormalizable operators that mix the 2HDM Higgs fields and the scalars in the Dark Sector. As a result, we split the Lagrangian into logically separate parts:

$$\mathcal{L} = \mathcal{L}_{\text{SM+2HDM}} + \mathcal{L}_{\text{DS}} + \mathcal{L}_{\text{Portal}}, \tag{4.16}$$

and discuss the individual parts in this section.

2HDM Extension of the Standard Model

Two Higgs doublet extensions of the Standard Model are part of the standard lore of particle physics [119]. As opposed to the Standard Model (which we will occasionally call 1HDM), where only one Higgs field spontaneously breaks the Electro-Weak symmetry and gives mass to fermions, these extensions contain additional Higgs doublet. In order to avoid large flavor-changing neutral currents, only one Higgs field is allowed to couple to up-type quarks, down-type quarks and leptons, respectively. We will use the type II model in which H_u couples to the up-type quarks and H_d couples to the down-type quarks and leptons called. After Electro-Weak symmetry breaking (EWSB), this extension contains two massive neutral singlets h_u and h_d. These mix and we will rotate the flavor basis $\{h_u, h_d\}$ into the mass eigenstate basis $\{h, H\}$:

$$\begin{pmatrix} h \\ H \end{pmatrix} = \begin{pmatrix} \cos\alpha & -\sin\alpha \\ \sin\alpha & \cos\alpha \end{pmatrix} \begin{pmatrix} h_u \\ h_d \end{pmatrix} \tag{4.17}$$

The ratio of the two vacuum expectation values of the two Higgs fields is called $\tan\beta = v_u/v_d$. The couplings of the light h and the heavy H to up-type and down-type fermions are then proportional to:

$$y_u^h = \frac{m_u}{v}\frac{\cos\alpha}{\sin\beta} \qquad y_{d,l}^h = -\frac{m_{d,l}}{v}\frac{\sin\alpha}{\cos\beta} \qquad y_u^H = \frac{m_u}{v}\frac{\sin\alpha}{\sin\beta} \qquad y_{d,l}^H = \frac{m_{d,l}}{v}\frac{\cos\alpha}{\cos\beta} \tag{4.18}$$

The 2HDM extension also contains a pseudoscalar neutral boson A and a charged $H^\pm$, but they do not significantly contribute to our analysis since $H^\pm$ is charged and therefore does not mix with the Dark Sector and A is typically too heavy under current experimental constraints.

The Dark Sector

As we state in the introduction, there is no reason why the Dark Sector should be simple. This view certainly complicates our ability to fully classify the effects of Dark Sector on measurable quantities. We take the view that although there is no reason Dark Sector

should be simple, it is certainly preferable to start with a simple one. However, too simple Dark Sector is unlikely to produce any new signal worth looking for. In order to avoid both problems we take what we consider a low energy effective theory of the Dark Sector with a worthwhile consequences. It contains two real scalars n_1 and n_2. We assume no symmetry properties for these scalars. This Dark Sector can be summarized by its Lagrangian:

$$\mathcal{L}_{\mathrm{DS}} = \frac{1}{2}\partial^\mu n_1 \partial_\mu n_1 + \frac{1}{2}m_1^2 n_1^2 + \frac{1}{2}\partial^\mu n_2 \partial_\mu n_2 + \frac{1}{2}m_1^2 n_2^2 + \frac{1}{3!}\sum_{ijk}\Lambda_{ijk} n_i n_j n_k + \frac{1}{4!}\sum_{ijkl}\lambda_{ijkl} n_i n_j n_k n_l \tag{4.19}$$

In the next paragraph we will choose benchmark values of m_1, m_2 as well as Λ_{ijk}. We propose several mass study points for this Dark Sector as indicated in table 4.6.2. Study points SP1 and SP4 feature a particularly wide n_1. Currently, rather large values of ϵ_1 are allowed for $m_1 = 2$ GeV, which is why we choose three of the study points along this line. For completeness we also choose SP4 because it is a good representative for the low mass Dark Sector.

Study Point	m_1 [GeV]	m_2 [GeV]
SP1	2.0	0.85
SP2	2.0	0.5
SP3	2.0	0.3
SP4	0.7	0.3

Table 4.2: List of Study Points.

In order to avoid the existence of easily detected sharp resonances we require that the decay width for the process $n_1 \to n_2 n_2$ be as large as possible. We parametrize the dimensionful

$$\Lambda_{122} = \sqrt{16\pi\lambda_{122}}m_2 \tag{4.20}$$

The $n_1(n_2)^2$ operator is also responsible for mass correction to both n_1 and n_2, which is why we express it in terms of m_2. This way it is easier to track the contribution of Λ_{122} to

renormalization of m_2. With this parametrization, the width of n_1 takes a simple form:

$$\Gamma(n_1 \to n_2 n_2) = \lambda_{122} \frac{m_2^2}{m_1} \sqrt{1 - 4\frac{m_2^2}{m_1^2}} \tag{4.21}$$

This is maximized for $m_1 = \sqrt{6} m_2$, leading to $\Gamma_1/m_1 \sim \lambda_{122}/10$. When λ_{122} is large this theory becomes strongly coupled and our perturbative approach fails to make any sense. Also, for large enough λ_{122} the cut-off needed to regulate the mass of n_2 becomes very low. We estimate that the boundary between the weakly coupled and the strongly coupled regimes sits around $\lambda_{122} \sim 1$ for $m_1 \sim m_2$, whereas the cut-off becomes too low ($\sim m_{B_s}$) at around $\lambda_{122} \sim 1/3$. Allowing a 1% fine-tuning for m_2^2, λ_{122} can be as large as 30 – far in the nonperturbative regime. Therefore as long as we stay within the perturbative regime, we do not have to be worried about fine-tuning between the cubic operators and the mass operator. For more details you can read section 4.6.8.

Higgs Portal

As already advertised we will establish interactions with the Standard Model through the 2HDM generalized Higgs Portal. We will consider the set of all 2 dimensional operators that cause mixing between 2HDM and Dark Sector scalars:

$$\mathcal{L}_{\text{Portal}} = m_{1u}^2 h_u n_1 + m_{2u}^2 h_u n_2 + m_{1d}^2 h_d n_1 + m_{2d}^2 h_d n_2 \tag{4.22}$$

In a general model we would have to find the eigenvectors of the full four dimensional ($\{h_u, h_d, n_1, n_2\}$) Hamiltonian. However, since we do not expect the cross-terms m_{ix}^2 are very large, it is sufficient to define pairwise rotations by angles

$$\theta_{ix} \sim \frac{m_{ix}^2}{m_x^2 - m_i^2}. \tag{4.23}$$

These define almost eigenstates $\tilde{n}_i$ and $\tilde{h}_x$:

$$\begin{pmatrix} \tilde{h}_u \\ \tilde{n}_1 \end{pmatrix} = \begin{pmatrix} \cos\theta_{u1} & \sin\theta_{u1} \\ -\sin\theta_{u1} & \cos\theta_{u1} \end{pmatrix} \begin{pmatrix} h_u \\ n_1 \end{pmatrix}. \tag{4.24}$$

We define θ_{2u}, θ_{1d} and θ_{2d} similarly. The rotations defined be these angles do not commute, and so any successive application of these four rotations will not lead to mass eigenstates of

the model. However, as we will see in the subsequent sections, these angles are small and so all the terms arising from commutators are going to be suppressed and the states $\tilde{n}_i$ and $\tilde{h}_x$ are going to be for all practical purpose good eigenstates of the Hamiltonian of the theory. Ignoring the $h_u h_d$ mass mixing operator for now, we can use a single matrix to rotate into the mass eigenstate basis. To the first order in θ_{ix} this matrix takes a simple form:

$$\begin{pmatrix} \tilde{h}_u \\ \tilde{h}_d \\ \tilde{n}_1 \\ \tilde{n}_2 \end{pmatrix} = \begin{pmatrix} 1 & 0 & \theta_{u1} & \theta_{u2} \\ 0 & 1 & \theta_{d1} & \theta_{d2} \\ -\theta_{u1} & -\theta_{d1} & 1 & 0 \\ -\theta_{u2} & -\theta_{d2} & 0 & 1 \end{pmatrix} \begin{pmatrix} h_u \\ h_d \\ n_1 \\ n_2 \end{pmatrix} \tag{4.25}$$

It is more convenient to express these angles by a different set of parameters:

$$\begin{aligned} \theta_{u1} &= \epsilon_1 \cos\delta_1 \\ \theta_{d1} &= \epsilon_1 \sin\delta_1 \\ \theta_{u2} &= \epsilon_2 \cos\delta_2 \\ \theta_{d2} &= \epsilon_2 \sin\delta_2. \end{aligned} \tag{4.26}$$

This way ϵ_i stand for the amount of mixing between n_i and the Standard Model Higgses, while $\tan\delta_i$ marks the ratio between n_i's couplings with up-type and down-type fermions. In this treatment we only need to require that $\epsilon_1, \epsilon_2 \ll 1$ in order to ensure that all four mixing angles are small. Rotating into the mass eigenstate basis also introduces new mixed cubic and quartic operators between the two sectors. For example, we encounter a new operator that allows Higgs decay into pairs of Dark Sector scalars:

$$\mathcal{L}_{new} = \ldots + \frac{1}{2}\epsilon_1 \cos\delta_1 \Lambda_{122} h_u n_2 n_2 + \ldots \tag{4.27}$$

We will explore how this affects the range of allowed parameters in the later sections of this paper.

4.6.3 An Example Model

In order to render our model more believable, we present an example model. We take the two Higgs Doublet Model and populate the Dark Sector with a fermion ψ that transforms

under an $SU(N)$ with a confinement scale Λ_D. We add a heavy Dark Sector higgs-like scalar X, with a vev v_X. The X and Higgses mix and the UV Langrangian for this Dark Sector takes the familiar form:

$$\mathcal{L} = \bar{\psi} \not{D} \psi + \lambda_\psi X \bar{\psi}\psi + \lambda_X \left(X^\dagger X - v_X^2 \right)^2 + \\ + \lambda_{Xu} \left(X^\dagger X - v_X^2 \right) \left(H_u^\dagger H_u - v_u^2 \right) + \lambda_{Xd} \left(X^\dagger X - v_X^2 \right) \left(H_d^\dagger H_d - v_d^2 \right) \quad (4.28)$$

After symmetry breaking in the Dark Sector, we can integrate out the heavy X:

$$\mathcal{L} = \bar{\psi} \left(\not{D} + m_\psi \right) \psi + \cdots + \lambda_{Xu} \frac{\lambda_\psi v_X \bar{\psi}\psi}{M_X^2} \left(H_u^\dagger H_u - v_u^2 \right) + (u \longleftrightarrow d) \quad (4.29)$$

Below Λ_D $\bar{\psi}\psi \to f_D^2 n_i$. Thus we get an effective field theory for a bound state of $\bar{\psi}\psi$ coupled to our Higgses:

$$\mathcal{L} = (\partial n_i)^2 + m_i^2 n_i^2 + \left(\frac{\lambda_{Xu} \lambda_\psi v_X v_u f_D^2}{M_X^2} \right) h_u n_i + (u \longleftrightarrow d), \quad (4.30)$$

which corresponds to a misalignment between the flavor and mass basis of the order:

$$\theta_i^u \sim \frac{\lambda_{Xu} \lambda_\psi v_X v_u f_D^2}{M_X^2 m_h^2} \leq \frac{\lambda_{Xu} m_i v_u f_D^2}{M_X^2 m_h^2} \sim \frac{\lambda_{Xu} m_i^3 v_u}{M_X^2 m_h^2} \frac{f_D^2}{m_i^2} \sim \frac{\lambda_{Xu} m_i^3 \cos\beta}{M_X^2 m_h} \frac{f_D^2}{m_i^2} \quad (4.31)$$

Suppose that X is not much heavier than m_h, then we expect:

$$\theta_i^u \sim 10^{-5} \cos\beta \left(\frac{\lambda_{Xu}}{0.1} \right) \left(\frac{f_D}{m_i} \right)^2 \quad (4.32)$$

However, if the $SU(N)$ coupling remains strong between M_X and m_i, the operator $\bar{\psi}\psi$ might have a large anomalous dimension $\gamma \sim \mathcal{O}(1)$ near such an infrared conformal fixed point. This means that the operator

$$\left(\frac{\lambda_{Xu} \lambda_\psi v_X v_u f_D^2}{M_X^2} \right) h_u n_i \quad (4.33)$$

would be scaled by a factor:

$$\left(\frac{M_X}{m_i} \right)^\gamma . \quad (4.34)$$

This would allow a much larger $\theta_i^u \sim 10^{-1}$. It is possible to double the Dark Higgs sector in order to allow for different couplings between the Dark Sector bound states and Standard Model up and down Higgses.

4.6.4 Interactions between the Dark Sector and the Standard Model

We would like to observe measurable effects of our model in decays of B mesons. Therefore, we need to make sure B mesons can decay into Dark Sector. Moreover, unless we want to look for events with just missing energy we also need make sure that the Dark Sector particles decay back into Standard Model particles. In the next two sections we present how this can be done.

Going from Standard Model to the Dark Sector: B decays through the Higgs Penguin

We are interested in B meson decays into Dark Sector. This happens through the Higgs Penguin operator $\bar{s}bh$ and the Higgs Portal. The Standard Model Higgs Penguin has a relatively simple form compared to its 2HDM cousin. In the 2HDM extension the total size of the matrix elements as well as the ratio between the $\bar{s}bh$ and $\bar{s}bH$ couplings are functions of the form of the 2HDM extension as well as $\tan\beta$ and α. We will parametrize this model dependence by two parameters, ξ and γ, that modify the SM operator:

$$\begin{aligned}\mathcal{L}_{bs} =& \frac{3\sqrt{2}G_F m_t^2 V_{ts}^* V_{tb}\xi(\tan\beta, m_t, m_W, \ldots)}{16\pi^2 v}\left(h\cos\gamma + H\sin\gamma\right)[\bar{s}_L b_R] \\ =& \xi\lambda_p\left(h\cos\gamma + H\sin\gamma\right)[\bar{s}_L b_R],\end{aligned} \tag{4.35}$$

where we have defined:

$$\lambda_q = \frac{3\sqrt{2}G_F m_t^2 V_{tq}^* V_{tb} m_b}{16\pi^2 v} \tag{4.36}$$

$$|\lambda_s| = 9.47\times 10^{-6} \tag{4.37}$$

$$|\lambda_d| = 1.85\times 10^{-6} \tag{4.38}$$

Notice that these parameters are degenerate with other parameters in our model. For example, take the coupling $\bar{s}bn_i$:

$$\begin{aligned}\xi\lambda_p\left(h\cos\gamma + H\sin\gamma\right)[\bar{s}_L b_R] = \xi\lambda_p\left(h_u\cos(\gamma-\alpha) + h_d\sin(\gamma-\alpha)\right)[\bar{s}_L b_R] = \\ = \lambda_p(\xi\epsilon_i)\cos(\gamma-\alpha-\delta_i)n_i[\bar{s}_L b_R] + \ldots,\end{aligned} \tag{4.39}$$

and so until we have detailed knowledge of the 2HDM Higgs sector[3] we will be content with expressing all predictions in terms of $\xi\epsilon_i$ and δ_i.

[3] A Supersymmetric 2HDM will give different penguin strength compared to a simpler 2HDM extension

Current LHC searches constrain the Higgs sector to be very Standard Model-like [120]. These studies strongly prefer $\sin(\alpha - \beta) = 1$ and allow a somewhat large range for $\tan\beta$ including $\tan\beta = 1$. This would foreshadow Standard Model-like penguin diagrams with $\xi \sim 1$ and $\gamma \sim 0$. We will, for study purposes, use these values. However, due to the above mentioned degeneracy even if these are not correct assumptions our study can be easily recast into different 2HDM scenarios.

The nature of the link between the Standard Model B mesons and the Dark Sector scalars implies correlations between different decay channels, which should be exploited when identifying this particular Dark Sector. For example, an excess of events in $B_d \to K^0\mu\mu$ should be accompanied by a similar excess in $B^\pm \to K^\pm\mu\mu$, $B_s \to \phi\mu\mu$ as well as a smaller excess (by a factor of $|V_{td}/V_{ts}|^2$) in $B_s \to K\mu\mu$. Similarly, an excess in $B_s \to 4\pi$ should come with a similar excess in $B_d \to K + 4\pi$ and $B_s \to \phi + 4\pi$.

Going from the Dark Sector back to the Standard Model: Decays of n_1 and n_2

We have already ensured that n_1 decays very quickly into two n_2s by setting λ_{122} as large as possible. However, since n_2 is the lightest Dark Sector particle, it can only decay into Standard Model particles. Its couplings through the Higgs Portal allow decays into pairs of leptons, mesons and photons. Given the nature of its couplings, the branching fractions into these modes are identical to those of a light Higgs boson and are dependent on the mass of n_2 as well as δ_2.

Ordinarily, for $m_2 < 2m_K$, we could be content with the chiral perturbation theory (χPT) prediction featured in section 4.6.9. However, Donoghue *et al.* have shown in [121] that higher order contributions generate a non-zero $\Delta_\pi = \langle\pi\pi|\bar{s}s|0\rangle$ matrix element (which violates the Zweig rule). The coefficient of this operator, m_s, is large enough to make its contribution towards $n_2 \to \pi\pi$ significant. One can think about this contribution as creating a virtual pair of kaons that rescatter into a pair of pions.

We will use data from [121] to form (what we believe to be) a more complete picture of decays of n_2. However, it is not clear how reliable the calculation is close to the $m_2 = 2m_K$ threshold where the ratio $\mathrm{Br}(\pi\pi)/\mathrm{Br}(\mu\mu)$ is significantly enhanced and the predictions in

this mass region should be taken with a grain of salt. Authors of [121] separate the transition operator into three parts:

$$\langle\pi\pi|\mathcal{O}|0\rangle = \langle\pi\pi|\theta^{\mu}_{\mu}|0\rangle + \langle\pi\pi|m_s\bar{s}s|0\rangle + \langle\pi\pi|m_u\bar{u}u + m_d\bar{d}d|0\rangle = \theta_\pi + \Delta_\pi + \Gamma_\pi \tag{4.40}$$

The contribution from Γ_π (due to smallness of m_u and m_d) is negligible and we will omit this operator in our analysis. In our model the couplings to up and down fermions are modified to:

$$m_u\bar{u}u \to \epsilon_2\frac{\cos\delta_2}{\sin\beta}m_u\bar{u}u \qquad m_d\bar{d}d \to \epsilon_2\frac{\sin\delta_2}{\cos\beta}m_d\bar{d}d \qquad m_l l^+l^- \to \epsilon_2\frac{\sin\delta_2}{\cos\beta}m_l l^+l^-, \tag{4.41}$$

which means that the relative branching fraction between pairs of pions and muons depends on β and δ_2:

$$\frac{\Gamma(n_2\to\pi\pi)}{\Gamma(n_2\to\mu\mu)} = \frac{\left|\left(\frac{2\cot\delta_2\cot\beta+1}{3}\right)\mathrm{BF}(SM,\Delta_\pi=0)^{\frac{1}{2}} + \left(\frac{25-4\cot\delta_2\cot\beta}{21}\right)\mathrm{BF}(SM,\theta_\pi=0)^{\frac{1}{2}}\right|^2}{\mathrm{BF}(n_2\to\mu\mu)_{SM}}, \tag{4.42}$$

where $\mathrm{BF}(SM,\mathcal{X}=0)$ is the branching fraction for a Standard Model Higgs with the operator $\mathcal{X}$ turned off, while $\mathrm{BF}(n_2\to\mu\mu)_{SM}$ would be the branching fraction of n_2 in a model with single Higgs boson. Since the phases of θ_π and Δ_π are identical, we can extract exact contribution of each operator [121]. Figure 4.2 shows our results for the branching ratio $\Gamma(n_2\to\pi\pi)/\Gamma(n_2\to\mu\mu)$ for a range of m_2.

4.6.5 Constraining the Model

In order to make our task manageable we will limit the range of some parameters (such as m_1 and m_2) as well as only use a set of discrete values for other parameters (δ_1 and δ_2). Using chosen values we will then derive constraints on ϵ_1 and ϵ_2. With a complete set of parameters we will then make predictions for multi-particle final states that have not been yet measured and (happily) point out that the allowed rates are large and (hopefully) observable.

How do we extract ϵ_1 and ϵ_2? First, in agreement with our initial desire to work with a

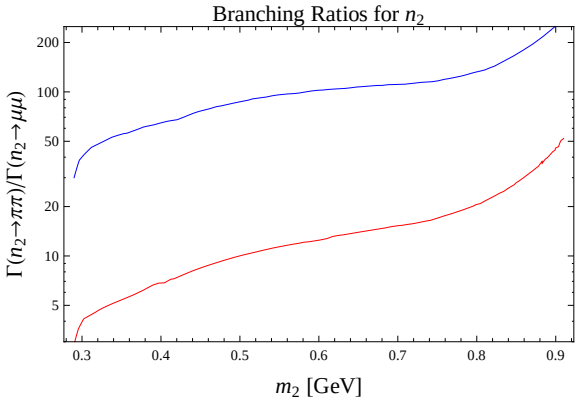

Figure 4.2: Branching ratio $\mathrm{Br}(n_2 \to \pi\pi)/\mathrm{Br}(n_2 \to \mu\mu)$ as a function of m_2. The lower, red curve corresponds to $\delta_2 = \pi/4$, the higher, blue curve represents the choice $\delta_2 = pi/16$.

almost strongly coupled Dark Sector we set all the Dark Sector scalar couplings:

$$\Lambda_{111} = \sqrt{16\pi\lambda_{111}}m_1, \quad \lambda_{111} = 1 \tag{4.43}$$

$$\Lambda_{112} = \sqrt{16\pi\lambda_{112}}m_2, \quad \lambda_{112} = 1 \tag{4.44}$$

$$\Lambda_{122} = \sqrt{16\pi\lambda_{122}}m_2, \quad \lambda_{122} = 1 \tag{4.45}$$

$$\tag{4.46}$$

Whereas operators $\Lambda_{112}n_1^2n_2$ and $\Lambda_{122}n_1n_2^2$ contribute to renormalization of m_2 we make them proportional to m_2. On the other hand Λ_{111} is proportional to m_1 since it does not renormalize m_2 at one-loop level.

The way we set things up the processes $B_q \to M\mu\mu$ and $B_q \to M\pi\pi$ are dominated by the narrow n_2 resonance and their rates are virtually independent of any of the properties of n_1. Therefore, we use these processes to constrain $\epsilon_2(m_2, \delta_2)$. The allowed $\epsilon_2(m_2, \delta_2)$ is low enough that New Physics contribution to processes such as $B_q \to \mu\mu$, $B_q \to \pi\pi$ as well as $B_q \to 4\mu$ or $B_q \to 4\pi$ is dominated by n_1 in the s-channel. This means we can constrain use the two and four body decays of B_q to constrain $\epsilon_1(\delta_1, \delta_2, m_1, m_2)$ for given δ_1, δ_2, m_1 and m_2.

But how do we choose δ_1 and δ_2? We choose $\delta_1 = \pi/4$. Although we could choose a different value, present constraints on this Dark Sector do not force us to go beyond what

the 1HDM would naturally bring.

The parameter δ_2 determines whether the final states of Dark Sector decays are hadronic or leptonic. We choose two different scenarios: the 1HDM equivalent $\delta_2 = \pi/4$ and the somewhat leptophobic $\delta_2 = \pi/16$. We believe that possibly the best motivation for the somewhat leptophobic scenario is that it represents a logical possibility that provides a motivation for exploring a large swath of experimental scenarios such as high multiplicity hadronic final states. However, note that $\cot \pi/16 \sim 5$, therefore this is not a particularly fine-tuned scenario. With every other parameter in place we are ready to constrain ϵ_1 and ϵ_2.

Constraining ϵ_2 with Three Body Final States

Decays of B mesons into a meson and n_i result in final states such as $K\mu\mu$, $K^*\mu\mu$, $\phi\pi\pi$. The s-channel contribution from the broad n_1 is negligible compared to the much narrower on-shell n_2 as long as $\epsilon_2 > 10^{-4}\epsilon_1$, which we will find true. Therefore, these decay channels only depend on ϵ_2, δ_2 and m_2. Since many of these final states are well constrained by experimental measurements and some are accessible to theoretical predictions with varying range of accuracy and reliability we can use these measurements and predictions to put significant constraints on ϵ_2. Table 4.3 lists the decay channels we use to constrain our model as well as the HFAG combinations [116], the Standard Model predictions and the allowed 2σ deviation for each channel. Similar results in agreement with ours can be found in [122]. Every B_d channel has an equivalent B_u channel. The currents responsible for these transitions are identical (if we treat the u and d quarks as spectators there is no difference at all) and so up to minor electromagnetic corrections these modes are nearly identical. The experimental constraints are also very similar and so we list the charged B meson modes for completeness rather than for additional information. Notice that for the same reason the lattice predictions are identical for the neutral and charged modes. The widths for

Process	HFAG combination [116]	SM prediction	Allowed 2σ Excess
$B_d \to K\mu\mu$, $q^2 < 2\text{GeV}^2$	$0.32^{+0.21}_{-0.20} \times 10^{-7}$	$(0.67 \pm 0.28) \times 10^{-7}$, [123]	0.35×10^{-7}
$B_d \to K\pi\pi$ (NR)	$(14.7 \pm 2.0) \times 10^{-6}$	Unreliable	18.7×10^{-6}
$B_d \to K^*\mu\mu$, $q^2 < 2\text{GeV}^2$	$(1.46 \pm 0.5) \times 10^{-7}$	$(2.0 \pm 0.25) \times 10^{-7}$, [124]	0.57×10^{-6}
$B_d \to K^*\pi\pi$	$(55 \pm 5) \times 10^{-6}$	Unreliable	65×10^{-6}
$B_u \to K^+\mu\mu$, $q^2 < 2\text{GeV}^2$	$(0.53 \pm 0.04) \times 10^{-7}$	$(0.67 \pm 0.28) \times 10^{-7}$, [123]	0.42×10^{-7}
$B_u \to K^+\pi\pi(NR)$	$(16.3 \pm 2.0) \times 10^{-6}$	Unreliable	20.3×10^{-6}
$B_u \to K^{+*}\mu\mu$ $q^2 < 2\text{GeV}^2$	$(1.41 \pm 0.5) \times 10^{-7}$	$(2.0 \pm 0.25) \times 10^{-7}$, [124]	0.52×10^{-6}
$B_u \to K^{+*}\pi\pi$	$(75.3 \pm 10.1) \times 10^{-6}$	Unreliable	95.5×10^{-6}
$B_s \to \phi\mu\mu$	$(0.91 \pm 0.24) \times 10^{-6}$	1.23×10^{-6} [125]	0.16×10^{-6}
$B_s \to K\pi\pi$	$(11.9 \pm 3.7) \times 10^{-6}$	Unreliable	19.3×10^{-6}

Table 4.3: Some three body decay channels of B mesons we use to constrain the parameters of our model. NR stands for non-resonant and $q^2 < 2\text{GeV}^2$ implies a constraint in a particular bin of the differential cross-section.

$B_q \to Pn_2$ and $B_q \to Vn_2$ are expressed in terms of Form Factors adopted from [126, 127]:

$$\Gamma(B_q \to Pn_2) = \frac{\lambda_q^2 \epsilon_2^2 \cos^2(\gamma - \alpha - \delta_2)}{64\pi m_{B_q}^3 m_b^2} \left(m_{B_q}^2 - m_P^2\right)^2 \left|f_0^{q\to P}(m_2^2)\right|^2 \times \times \left[\left(m_{B_q}^2 - (m_2 - m_P)^2\right)\left(m_{B_q}^2 - (m_2 + m_P)^2\right)\right]^{1/2} \quad (4.47)$$

$$\Gamma(B_q \to Vn_2) = \frac{\lambda_q^2 \epsilon_2^2 \cos^2(\gamma - \alpha - \delta_2)}{16\pi m_{B_q}^3 m_b^2} \left|A_0^{q\to V}(m_2^2)\right|^2 \left[\left(m_{B_q}^2 - (m_2 - m_V)^2\right)\left(m_{B_q}^2 - (m_2 + m_V)^2\right)\right]^{3/2} \quad (4.48)$$

Since n_2 is very narrow, there is virtually no interference between the SM processes and New Physics, which justifies incoherently adding results of equations 4.47 and 4.48 to the Standard Model contribution. The spectrum of the invariant mass of the two muons would

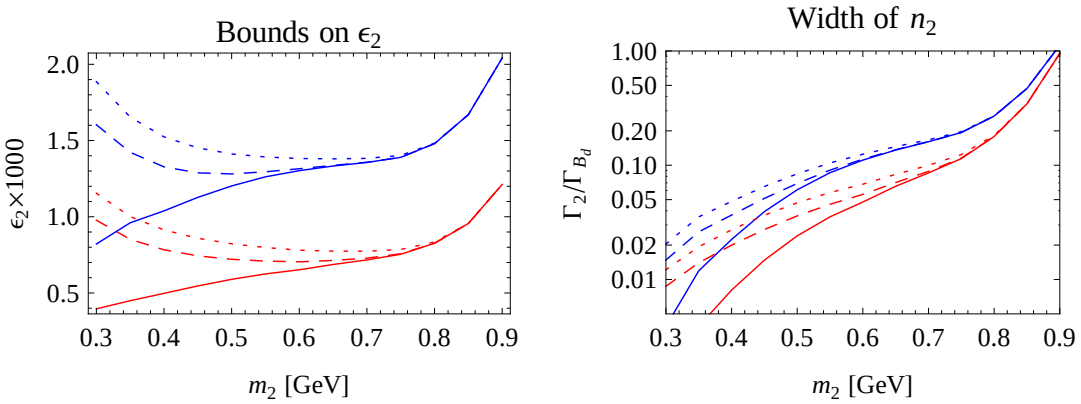

Figure 4.3: On the left, the bounds on ϵ_2 for $\delta_2 = \pi/4$ are shown in red and the bounds for $\delta_2 = \pi/16$ are shown in blue. The solid lines represent results of a naive analysis that assumes a full sensitivity independent of the lifetime of n_2. The dotted and dashed lines represent the bounds on ϵ_2 if decays that happen within 5 cm or 10 cm of the primary interaction point were recorded. The right figure shows the width of n_2 in terms of width of B_d. The dashed lines show the actual values including the correction from lowered detector acceptance due to long lifetimes of n_2.

show a narrow peak centered around m_2. It may seem dangerous to place a very narrow line in a well measured process. However, although the differential width $d\Gamma dq^2$ is a well measured quantity, a search for narrow lines has been only done below $m_2 < 0.3$ GeV [128]. Above this mass the results are quoted in somewhat coarser bins. Since our study points satisfy $m_2^2 < 2$ GeV^2, when the differential width measurements are available, we use the binned ($0 < q^2 < 2$ GeV^2) measurement to obtain stronger constraints on ϵ_2.

When ϵ_2 is low enough, n_2 becomes long-lived on detector scales. As a result, the detector acceptance suffers and the bounds on ϵ_2 weaken. In order to model this effect when considering the bounds on ϵ_2 we only consider the portion of n_2s that decay within 5 cm or within 10 cm from the primary interaction point. We summarize these bounds on ϵ_2 in figure 4.3.

Constraining ϵ_1 with $B_q \to \mu\mu$ and $B_q \to \pi\pi$

With recent experimental determination of the branching fraction $B_s \to \mu\mu$ and ever increasing constraints on $B_d \to \mu\mu$, these two channels could provide a constraint on our model. In $B_q \to n_i \to \mu\mu$ the momentum flowing through n_i is fixed to $q^2 = m_B^2$. Unless m_1 or m_2 are close to the mass of the B meson, this processes is not enhanced by any resonances as it was in $B_q \to M n_i$. Given that the n_1 and n_2 propagators are both of nearly equal size, the relative strength of these two s-channel processes is set by the ratio ϵ_1/ϵ_2. However, bounds from $B_q \to M n_2$ force ϵ_2 so low that n_2 has no measurable effect on this branching fraction. Notice that the contribution from the neutral Higgs particle with mass m_h is suppressed by $(m_B/\epsilon_1 m_h)^4 \sim (25\epsilon_1)^{-4}$. Therefore we cannot constrain ϵ_1 much below 0.04 using this decay. As a result the expression for this partial width is relatively simple (as long as $\epsilon_1 \gtrsim 0.04$):

$$\Gamma(B_q \to n_1^* \to \mu\mu) = \frac{1}{8\pi} \frac{m_{B_q}^5 m_\mu^2 f_{B_q}^2}{v^2 m_b^2 \cos^2\beta} \frac{\lambda_q^2 \epsilon_1^4 \cos^2(\gamma - \alpha - \delta_1) \sin^2(\delta_1)}{(m_{B_q}^2 - m_1^2)^2 + m_1^2 \Gamma_1^2(m_{B_q}^2)}, \tag{4.49}$$

where it is important to evaluate the width of n_1 at $q^2 = m_B^2$. We show the experimental values and the Standard Model predictions for branching fractions as well as the allowed 2σ deviations for the decay modes of interest in table 4.4. The constraints from these processes

Process	HFAG combination [116]	SM prediction	Allowed 2σ Excess
$B_s \to \mu\mu$	$(3.2 \pm 1) \times 10^{-9}$	$(3.23 \pm 0.27) \times 10^{-9}$, [129]	2×10^{-9}
$B_s \to \pi\pi$	$(0.73 \pm 0.14) \times 10^{-6}$	$(0.57^{+0.26}_{-0.23}) \times 10^{-6}$, [130]	0.76×10^{-6}
$B_d \to \mu\mu$	$< 8 \times 10^{-10}$	$(1.07 \pm 0.1) \times 10^{-10}$, [129]	7×10^{-10}
$B_d \to \pi\pi$	7.01 ± 0.29	pQCD: $(6.7 \pm 3.8) \times 10^{-6}$, [130]	7.9×10^{-6}
		SCET: $(6.2 \pm 4) \times 10^{-6}$, [131]	9.1×10^{-6}

Table 4.4: Two particle decay channels of B mesons we use to constrain ϵ_1.

are in general not strong enough to constrain ϵ_1. This is because these processes do not create any on-shell Dark Sector states and are therefore suppressed by the additional factors of $(\epsilon_1 m_\mu/v)^2 \sim 10^{-9}$. In general we will obtain much higher rates (at the possible cost of

displaced vertices) by creating on-shell Dark Sector states that decay into SM particles later. The most constraining modes are presented in the next section.

Constraining ϵ_1 with $B_q \to 4\mu$ and $B_q \to 4\pi$

As we have mentioned, $B_q \to n_i \to \mu\mu$ do not constrain ϵ_1 all that well in comparison with other decay modes such as $B_q \to 4\mu$. Similar to the three particle final state, the dominant contribution to $B_q \to 4\mu$ comes from $B_q \to 2n_2 \to 4\mu$ with both n_2s on-shell. The width for this processes is not complicated:

$$\Gamma(B_q \to 2n_2) = \frac{1}{32\pi}\frac{\lambda_q^2 f_{B_q}^2 m_{B_q}^3}{m_b^2}\left|\frac{4m_2\sqrt{\pi\lambda_{122}}\epsilon_1\cos(\gamma-\alpha-\delta_1)}{m_{B_q}^2 - m_1^2 + im_1\Gamma_1(m_B^2)} + \frac{4m_2\sqrt{\pi\lambda_{222}}\epsilon_2\cos(\gamma-\alpha-\delta_2)}{m_{B_q}^2 - m_2^2 + im_2\Gamma_2(m_B^2)} + \right.$$
$$\left. + \frac{\Lambda_{h22}\cos(\gamma)}{m_{B_q}^2 - m_h^2} + \frac{\Lambda_{H22}\sin(\gamma)}{m_{B_q}^2 - m_H^2}\right|^2 \quad (4.50)$$

Notice that we have set $\lambda_{122} = \lambda_{222}$ and the n_1 and n_2 propagators are dominated by m_B^2 and so their relative contribution is again determined by the ratio ϵ_1/ϵ_2. We only need to keep the contribution from n_1 unless $\epsilon_1 \sim \epsilon_2$. The Higgs contribution is suppressed by

$$f_h = \frac{\Lambda_{h22} m_B^2}{\epsilon_i \Lambda_{i22} m_h^2} \sim \frac{\Lambda_{h22}}{\epsilon_i \Lambda_{i22}}\frac{m_B^2}{m_h^2}. \quad (4.51)$$

We expect $\Lambda_{h22} \sim \epsilon_i \Lambda_{i22}$ and so the s-channel Higgs contribution is suppressed by $(m_B/m_h)^2$ and is negligible. This is true every time n_1 carries momentum much smaller than the mass of Higgs and we will ignore the low momentum Higgs boson contribution in the future. Thus, we only need to consider a simple partial width:

$$\Gamma(B_q \to 2n_2) = \frac{\lambda_q^2 f_{B_q}^2 m_{B_q}^3 m_2^2}{m_b^2}\frac{\lambda_{122}\epsilon_1^2\cos^2(\gamma-\alpha-\delta_1)}{(m_{B_q}^2 - m_1^2)^2 + m_1^2\Gamma_1(m_B^2)^2} \quad (4.52)$$

The properties of the three experimentally measured decay channels that fall into this category are summarized in table 4.5. The most stringent test (not surprisingly) comes from $B_s \to 4\mu$ since the other two channels are suppressed by $|V_{td}/V_{ts}|^2$. Measuring $B_s \to 4\pi$ would provide a great constraint on ϵ_1 for $\delta_2 = \pi/16$, however, an experimental measurement of this mode is currently unavailable. We present bounds on ϵ_1 in figure 4.5.

Process	HFAG combination [116]	SM prediction	Allowed 2σ Excess
$B_s \to 4\mu$	$< 1.2 \times 10^{-8}$	NR: $< 10^{-10}$, [132]	$< 1.2 \times 10^{-8}$
$B_d \to 4\mu$	$< 5.1 \times 10^{-9}$	Negligible	$< 5.1 \times 10^{-9}$
$B_d \to 4\pi$	$< 19.3 \times 10^{-6}$	Unreliable	$< 19.3 \times 10^{-6}$

Table 4.5: Four particle decay channels of B mesons we use to constrain ϵ_1.

Changes to the $B - \bar{B}$ oscillations

Both n_1 and n_2 can cause the transition between B_q and $\bar{B}_q$ for $q \in \{d, s\}$ by participating in the following diagrams:

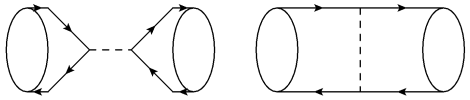

In the s-channel the momentum running through the n_1 propagator is just m_{B_q}. In the t-channel the momentum depends on the parton wave functions inside the B meson. Nevertheless, it will be on the order of $m_b - m_s$, therefore not much different from the s-channel and we will assume the two to be comparable. Assuming that the t-channel contributions are about the same (effectively doubling the rate) we can extract the contribution to both $\Delta m_q = 2M_{12} = \mathrm{Re}(\mathcal{M})/m_B$ and $\Delta\Gamma_q = 2\Gamma_{12} = \mathrm{Im}(\mathcal{M})/m_B$:

$$\begin{aligned}
\delta M_{12} =& \frac{2}{3}(\mathcal{B}\lambda_p^2 m_B f_B^2)\left(\frac{\epsilon_1^2\cos^2(\delta_1+\alpha-\gamma)(m_1^2-m_B^2)}{(m_1^2-m_B^2)^2+m_1^2\Gamma_1^2(m_B^2)} + \frac{\epsilon_2^2\cos^2(\delta_2+\alpha-\gamma)(m_2^2-m_B^2)}{(m_2^2-m_B^2)^2+m_2^2\Gamma_2^2(m_B^2)}\right)\\
\delta\Gamma_{12} =& \frac{1}{3}(\mathcal{B}\lambda_p^2 m_B f_B^2)\left(\frac{-\epsilon_1^2\cos^2(\delta_1+\alpha-\gamma)m_1\Gamma_1(m_B^2)}{(m_1^2-m_B^2)^2+m_1^2\Gamma_1^2(m_B^2)} + \frac{-\epsilon_2^2\cos^2(\delta_2+\alpha-\gamma)m_2\Gamma_2(m_B^2)}{(m_2^2-m_B^2)^2+m_2^2\Gamma_2^2(m_B^2)}\right),
\end{aligned} \tag{4.53}$$

where $\mathcal{B} \sim \mathcal{O}(1)$ is the bag parameter associated with the scalar operator $(b(1+\gamma_5)\bar{s})^2$. We use the scenario I from [133, 134] to evaluate the theoretical uncertainties connected with these measurements. The allowed deviations we are going to use are in table 4.6. Since the actual deviations cause by this model are quite small, it is unnecessary to study the relative CP violating phases ϕ_d and ϕ_s. Nevertheless, the changes to Δm_q and $\Delta\Gamma_q$ are at most on the order $\mathcal{O}(10^{-3})$, given other constraints on ϵ_1 and ϵ_2.

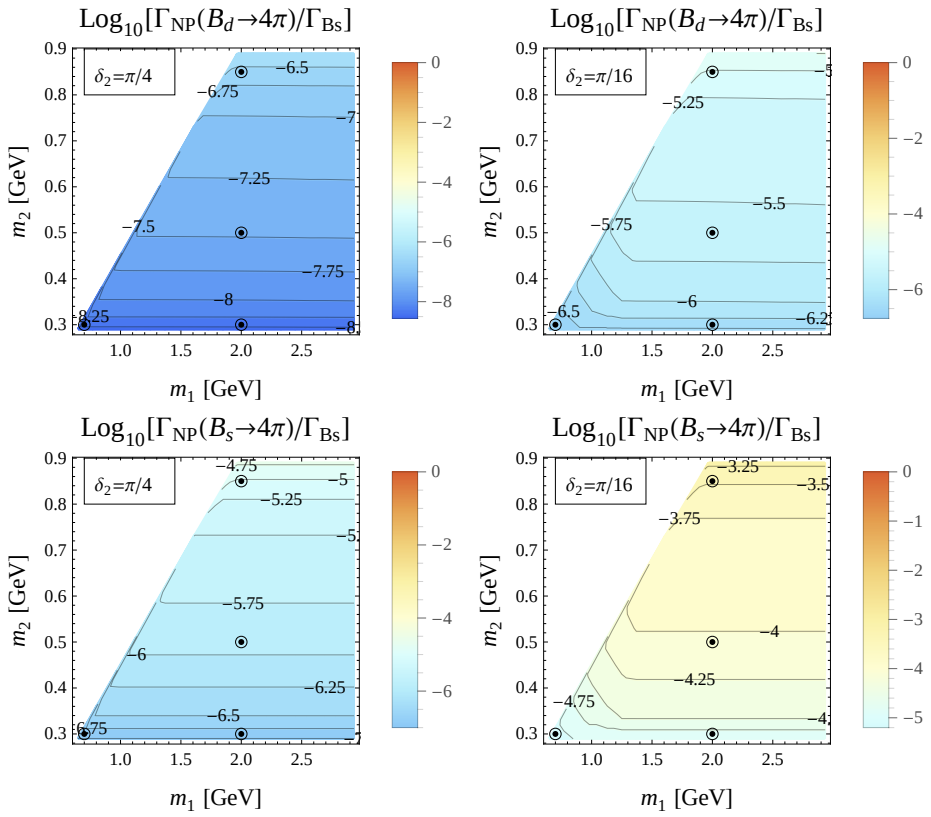

Figure 4.4: Plots of $B_d \to 4\pi$ and $B_s \to 4\pi$. $B_d \to 4\pi$ comes close to saturating the experimental bound for $m_2 \sim 0.9$ GeV. However, exploring the branching fraction for $B_s \to 4\pi$ would significantly constrain the model.

Collider Constraints: Higgs Decays and $pp \to \bar{b}bn_i$

Given the Dark Sector directly couples to the Higgs sector of the Standard Model, we naturally consider the constraints that would arise from collider studies. One of these is the invisible Higgs width, the second would associated production of n_i with a $\bar{q}q$ pair: $pp \to \bar{q}qn_i$.

If the $\bar{b}b$ is produced with energy much bigger than $E_{bb} \gg m_i$, it is quite possible to radiate n_i. The rate of radiation of a soft n_i is on the order:

$$\sigma(pp \to \bar{q}q + n_i) = \frac{y_q^2 \epsilon_i^2 f(\delta_i)^2}{4\pi} \sigma(pp \to \bar{q}q), \tag{4.54}$$

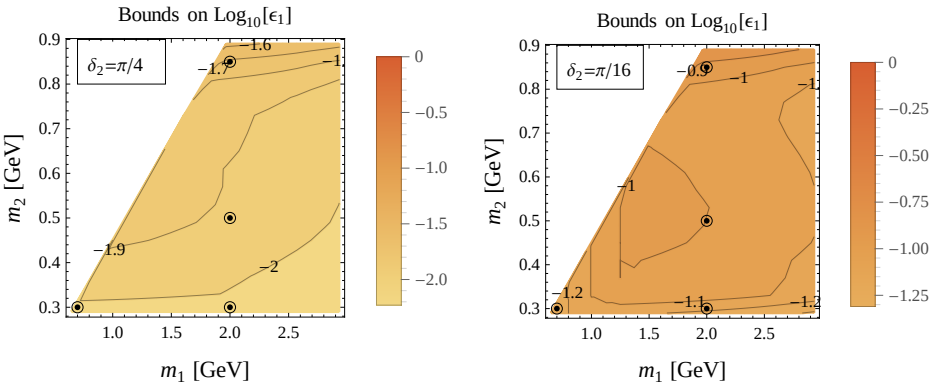

Figure 4.5: Bounds on ϵ_1 for $\delta_2 = \pi/4$ (left) and $\delta_2 = \pi/16$ (right). As expected choosing lower δ_2 relaxes the dominant bound from $B_s \to 4\mu$ which leads to larger ϵ_1.

Observable	Current experimental value	2σ Allowed NP contribution
Δm_d	3.3×10^{-13} GeV	$(-9.7, 7.0) \times 10^{-14}$ GeV
$\Delta\Gamma_d$	2.5×10^{-15} GeV	$(-0.7, 1.6) \times 10^{-15}$ GeV
Δm_s	1.2×10^{-11} GeV	$(-1.6, 2.1) \times 10^{-12}$ GeV
$\Delta\Gamma_s$	6.6×10^{-14} GeV	$(-2.4, 3.7) \times 10^{-14}$ GeV

Table 4.6: Allowed deviations from $B_q - \bar{B}_q$ mixing observables

where $f(\delta_i)$ is either $\cos(\delta_i)$ or $\sin(\delta_i)$ depending on the type of the quark. Since $\epsilon_1 \gg e_2$, we will consider n_1 makes the dominant contribution. A radiated n_i would promptly decay into $2n_2, 3n_2$ or $4n_2$ and these would then appear as multiple-muons, jets or muon rich jets, depending on m_2 and δ_2. The investigation of this phenomenon is quite beyond the scope of this paper and would be great topic of future work. Nevertheless, for our more sombre choice of $\delta_2 = \pi/4$, $\epsilon_1 \sim 10^{-2}$, which means that a pair of b quarks would radiate a soft n_1 with probability of about 5×10^{-8}. Since hard $\bar{b}b$ pair has a cross-section of about 11 nb, this makes the cross-section for radiative $\bar{b}bn_1$ on the order 0.5 fb, meaning there are about ten events in the 20 fb dataset. Therefore we believe this process does not represent a challenge to our model, so far.

As a result of the mass mixing our model allows processes such as $h \to n_i n_j$. Since $m_h \gg m_1, m_2$, the available phase space is about the same whether we consider $h \to 2n_1, n_1 n_2$, or $2n_2$. The partial width for $h \to n_i n_j$ is:

$$\Gamma(h \to \text{NP}) = \frac{1}{16\pi m_h} \sum_{ij} \frac{1}{S} \Lambda_{hij}^2, \tag{4.55}$$

where S stands for the necessary symmetry factor. If we impose a fairly loose constraint $\Gamma(h \to \text{NP}) \lesssim \frac{1}{2}\Gamma(h \to \text{SM}) \sim 2$ MeV, which would correspond to about 30% branching fraction for invisible decays of the Higgs boson. Thus we obtain a bound:

$$\frac{1}{2}\Lambda_{h11}^2 + \Lambda_{h12}^2 + \frac{1}{2}\Lambda_{h22}^2 \lesssim 16\pi(125 \text{ GeV})(2 \text{ MeV}) \sim (3.5 \text{ GeV})^2 \tag{4.56}$$

As we have shown in equation 4.27, the expected size of these operators is roughly $\sum \epsilon_i \Lambda_{ijk}$. As we will see, $\epsilon_1 \lesssim 10^{-1}$ or lower, and $e_2 \lesssim 10^{-3}$. Since the largest Λ_{ijk} is $\Lambda_{111} \lesssim \sqrt{16\pi} \times$ GeV ~ 20 GeV – this puts a slight constraint on ϵ_1 for the more massive n_1.

4.6.6 New Decay Channels of $\mathbf{B_q}$

This section presents decay channels of B mesons into multi-particle final states that have not been experimentally constrained. Our model provides a way to achieve rather high branching fractions for these modes.

Five Particle Final States

Instead of completely annihilating, the flavor changed constituent quarks of B meson might form another scalar or vector meson which appears in the final state. Therefore instead of $B_q \to 2n_2$ we might also observe $B_q \to M + 2n_2$, where M stands for any meson. In the future, we will use S for a scalar or pseudo-scalar meson and V for vector or pseudo-vector meson.

Under current constraints on ϵ_1 these decay modes have almost absurdly large branching fractions in the mesonic decay channels of B_d. Just as we have seen in the comparison between the 2PFS and 3PFS, the contribution from on-shell n_1 or n_2 can be large enough that these processes effectively become decays into two particle states, $B_q \to M n_i^*$, with n_i^*

slightly off-shell. We use the following width to obtain our predictions for final branching fractions we plot in figures 4.6 and 4.7 :

$$\frac{d\Gamma(B_d \to K + 2n_2)}{dq^2} = \frac{1}{128\pi^2}\frac{\lambda_{122}\epsilon_1^2\lambda_s^2 m_2^2\cos^2(\alpha-\gamma-\delta_1)}{m_b^2 m_{B_d}^3}(m_{B_d}^2 - m_K^2)^2\left|f_0^{B\to K}(q^2)\right|^2 \\ \frac{\sqrt{1-4m_2^2/q^2}\sqrt{\left(m_{B_d}^2-(|q|+m_K)^2\right)\left(m_{B_d}^2-(|q|-m_K)^2\right)}}{(q^2-m_1^2)^2+m_1^2\Gamma_1^2(q^2)} \quad (4.57)$$

$$\frac{d\Gamma(B_d \to K^* + 2n_2)}{dq^2} = \frac{1}{16\pi^2}\frac{\lambda_{122}\epsilon_1^2\lambda_s^2 m_2^2\cos^2(\alpha-\gamma-\delta_1)}{m_b^2 m_{B_d}^3}\left|A_0^{B\to K^\star}(q^2)\right|^2 \\ \frac{\sqrt{1-4m_2^2/q^2}\left(\left(m_{B_d}^2-(|q|+m_{K^\star})^2\right)\left(m_{B_d}^2-(|q|-m_{K^\star})^2\right)\right)^{3/2}}{(q^2-m_1^2)^2+m_1^2\Gamma_1^2(q^2)} \quad (4.58)$$

These modes present a great way to identify this particular model of the Dark Sector. Since all decays proceed through a Penguin operator, the annihilation decays of B_d are suppressed by a factor $|V_t d/V_{ts}|^2 \sim 0.04$. Nevertheless, the decays $B_d \to K +$ exotic proceed through the $b \to s$ penguin operator and therefore are not suppressed. Figure 4.8 shows the ratio $\Gamma_{NP}(B_s \to 2n_2)/\Gamma_{NP}(B_d \to K 2n_2)$, which is independent of all the couplings in the Dark Sector: ϵ_1, ϵ_2, δ_1, δ_2 and λ_{122}. This ratio should then only be dependent m_1, m_2 and the kinematic of the Standard Model bound states and forms an independent check on the model in decay modes of two *different* particles.

At first, it may be surprising that $B_d \to K + 4\pi$ has a larger rate compared to $B_s \to 4\pi$. However, since $m_B - m_K \sim m_B$ the only phase-space suppression comes from the $(4\pi)^{-1}$ factor. However, adding the Kaon allows n_1 to contribute on-shell and the form factor for $B_d \to K$ is typically larger than the annihilation form factor:

$$\langle K|b\bar{s}|B\rangle \sim (m_B^2 - m_K)^2\mathcal{O}(1) \quad (4.59)$$

$$\langle|b\bar{s}|B\rangle \sim f_B m_B^2 \quad (4.60)$$

Since the size of the phase-space is on the order m_B, ratio of these two is roughly $f_B/m_B \sim 20$. We will see that this trend persists and six and seven particle final states will also have comparable rates.

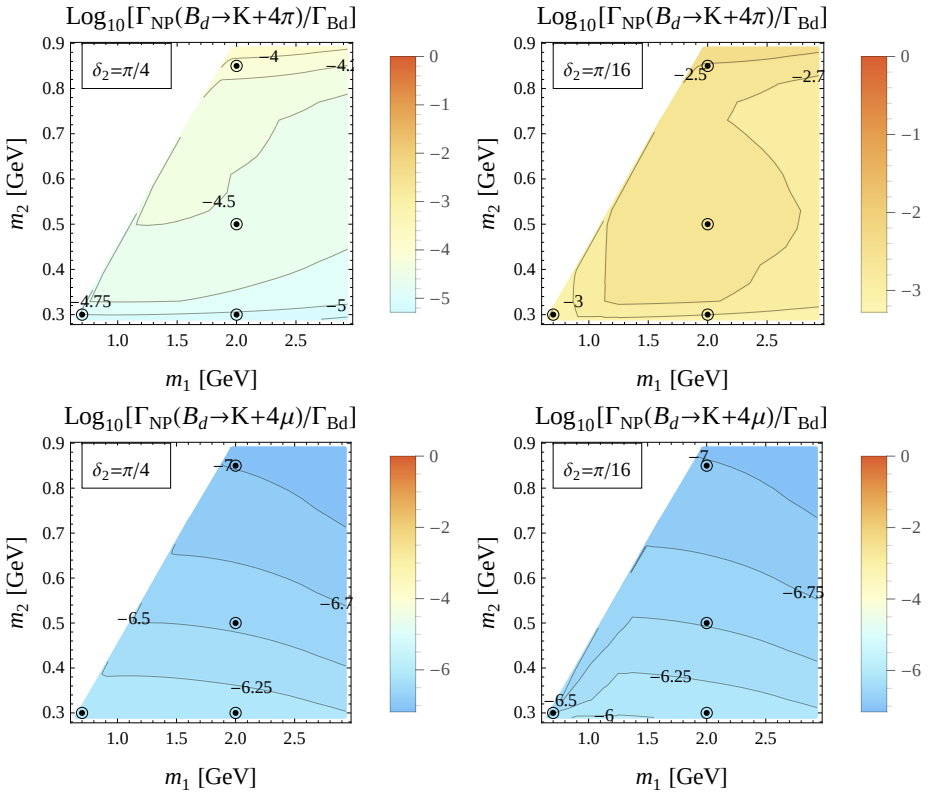

Figure 4.6: Five Particle decays $B_d \to K + 2n_2$. The purely muonic decay modes should be observable given the bounds on $B_q \to 4\mu$.

Six, Seven and Eight Particle Final States

The decay channel $B_s \to n_1^*$ does not have to proceed to $2n_2$ it can also turn into $n_1 n_2 \to 3n_2$ respectively $2n_1 \to 4n_2$ and so on. The later two options produce six and seven or eight and nine particle states, respectively. The even number particle states come from annihilation diagrams. Since we have designed the Dark Sector to sit close to the strongly coupled regime, additional branchings do not cost much and we expect these processes to have comparable branching fractions. Equations 4.61, 4.62, 4.63 and 4.64 show the widths for

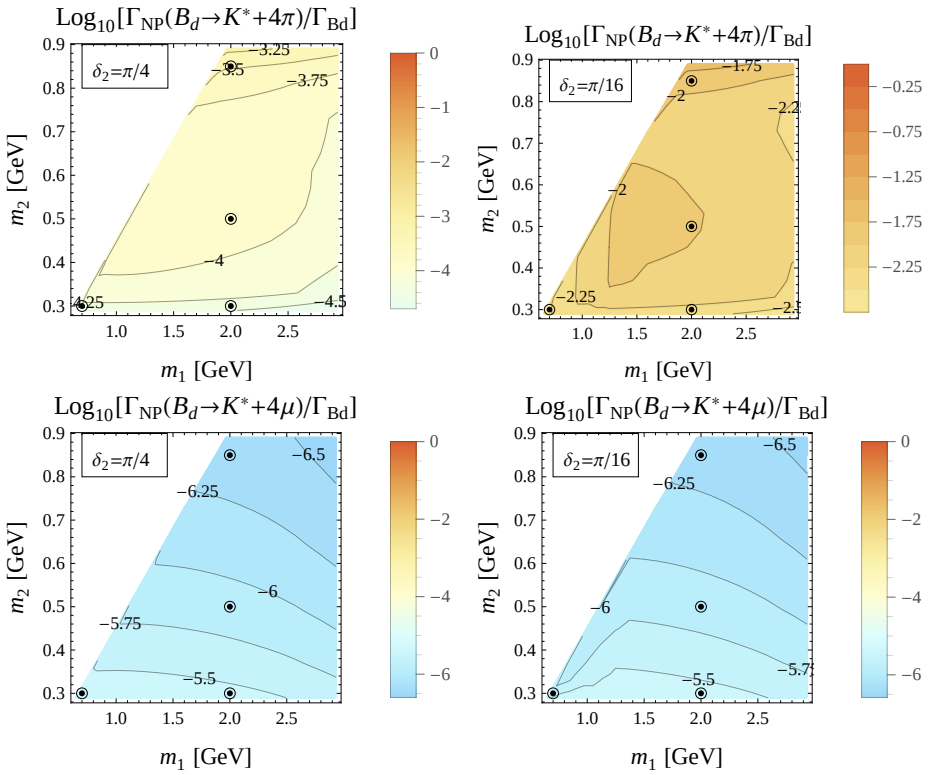

Figure 4.7: Five Particle decays $B_d \to K^* + 2n_2$. The purely muonic decay modes should be observable given the bounds on $B_q \to 4\mu$. The allowed branching fraction for $B_d \to K^{(*)} + 4\pi$ are very large and should be easy to constrain with experimental measurement.

these processes.

$$\frac{d\Gamma(B_s \to 3n_2)}{dq^2} = \frac{1}{6\pi} \frac{\lambda_{112}\lambda_{122}\epsilon_1^2\lambda_s^2 \cos^2(\alpha-\gamma-\delta_1) m_2^4 m_{B_s} f_{B_s}^2}{m_b^2} \times$$
$$\times \frac{\sqrt{1-4m_2^2/q^2}}{(m_{B_s}^2 - m_1^2)^2 + m_1^2\Gamma_1(m_{B_s}^2)} \frac{\sqrt{\left(m_{B_s}^2 - (|q|+m_2)^2\right)\left(m_{B_s}^2 - (|q|-m_2)^2\right)}}{(q^2-m_1^2)^2 + m_1^2\Gamma_1(q^2)} \quad (4.61)$$

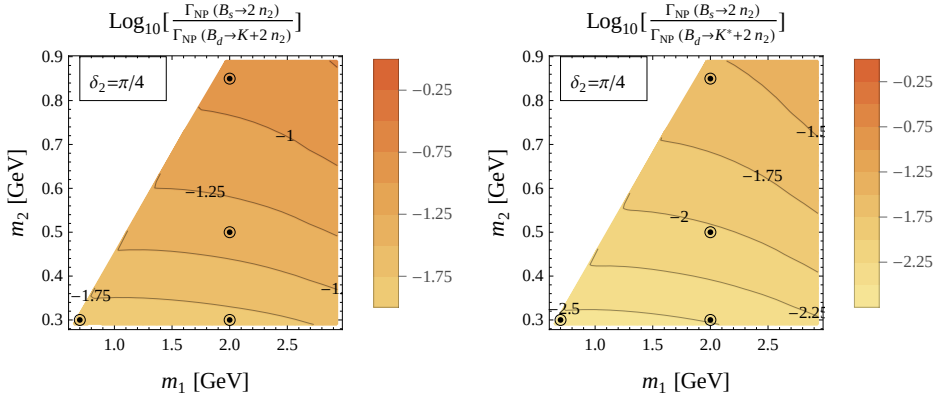

Figure 4.8: Comparison between four and five particle final states. This ratio is independent of ϵ_1, ϵ_2, δ_1, δ_2 and λ_{122}. You can see it does depend on m_1 and m_2. We can see that the five particle final states are preferred.

$$\frac{d^2\Gamma(B_d \to K + 3n_2)}{dq_{123}^2 dq_{12}^2} = \frac{1}{12\pi^3} \frac{\lambda_{112}\lambda_{122}\epsilon_1^2\lambda_s^2 \cos^2(\alpha-\gamma-\delta_1) m_2^4 m_{B_d}}{m_b^2 q_{123}^2} \left(1 - \frac{m_K^2}{m_{B_d}^2}\right)^2 \left|f_0^{B\to K}(q_{123}^2)\right|^2 \times$$
$$\times \sqrt{1 - 4m_2^2/q_{12}^2} \frac{\sqrt{\left(m_{B_d}^2 - (m_K + |q_{123}|)^2\right)\left(m_{B_d}^2 - (m_K - |q_{123}|)^2\right)}}{(m_1^2 - q_{123}^2)^2 + m_1^2\Gamma_1^2(q_{123}^2)} \times$$
$$\times \frac{\sqrt{\left(q_{123}^2 - (m_2 + |q_{12}|)^2\right)\left(q_{123}^2 - (m_2 - |q_{12}|)^2\right)}}{(m_1^2 - q_{12}^2)^2 + m_1^2\Gamma_1^2(q_{12}^2)} \quad (4.62)$$

$$\frac{d^2\Gamma(B_d \to V + 3n_2)}{dq_{123}^2 dq_{12}^2} = \frac{1}{3\pi^3} \frac{\lambda_{112}\lambda_{122}\epsilon_1^2\lambda_s^2 \cos^2(\alpha-\gamma-\delta_1) m_2^4}{m_b^2 q_{123}^2 m_{B_d}^3} \left|A_0^{B\to K^*}(q_{123}^2)\right|^2 \times$$
$$\times \sqrt{1 - 4m_2^2/q_{12}^2} \frac{\left(\left(m_{B_d}^2 - (m_K^* + |q_{123}|)^2\right)\left(m_{B_d}^2 - (m_{K^*} - |q_{123}|)^2\right)\right)^{3/2}}{(m_1^2 - q_{123}^2)^2 + m_1^2\Gamma_1^2(q_{123}^2)} \times$$
$$\times \frac{\sqrt{\left(q_{123}^2 - (m_2 + |q_{12}|)^2\right)\left(q_{123}^2 - (m_2 - |q_{12}|)^2\right)}}{(m_1^2 - q_{12}^2)^2 + m_1^2\Gamma_1^2(q_{12}^2)} \quad (4.63)$$

$$\frac{d^2\Gamma(B_s \to 4n_2)}{dq_{12}^2 dq_{34}^2} = \frac{1}{24\pi^2 m_b^2} \frac{\lambda_{111}\lambda_{122}^2\epsilon_1^2\lambda_s^2 \cos^2(\alpha-\gamma-\delta_1) m_1^2 m_2^4 m_{B_s} f_{B_s}^2}{(m_1^2 - m_{B_s}^2)^2 + m_1^2\Gamma_1^2(m_{B_s}^2)} \times$$
$$\times \sqrt{\left(1 - 4m_2^2/q_{12}^2\right)\left(1 - 4m_2^2/q_{34}^2\right)} \times$$
$$\times \frac{\sqrt{\left(m_{B_s}^2 - (|q_{12}| + |q_{34}|)^2\right)\left(m_{B_s}^2 - (|q_{12}| - |q_{34}|)^2\right)}}{\left((m_1^2 - q_{12}^2)^2 + m_1^2\Gamma_1^2(q_{12}^2)\right)\left((m_1^2 - q_{34}^2)^2 + m_1^2\Gamma_1^2(q_{34}^2)\right)} \quad (4.64)$$

The purely muonic final states are highly suppressed by the small muon branching fraction $BF(n_2 \to \mu^+\mu^-)$. Branching fractions on the order $\mathcal{O}(10^{-10})$ and lower rule out the possibility that discovery of New Physics will ever happen in the purely muonic final states. Instead we should turn our attention to hadronic decays as is apparent from figures 4.9 and 4.10.

4.6.7 Conclusion

We present to you a very simple model of the Dark Sector. By coupling this model to the Standard Model through a 2HDM generalization of the Higgs Portal we allow charmless high particle multiplicity decay modes of B mesons. While decays into muons are a great tool to discover many models of New Physics, it is not the case for this model because light Higgs-like scalars tend to decay into pairs of pions much more often than into pairs of muons, even if their coupling to up-type and down-type fermions are equal.

Although hadronic decays of B mesons are typically harder to constrain and the Standard Model backgrounds are hard to predict compared to their leptonic counterparts, our model offers branching fractions so large ($\sim 10^{-3}$) an experimental study should be able to significantly constrain the parameter space of our model. The signature of this model is a correlation between these exotic decay modes for B_d, B_u and B_s as well as presence of resonances that are invisible except in these large multiplicity decays.

4.6.8 Wide n_1

With the definition $\Lambda_{122} = \sqrt{16\pi\lambda_{122}}m_2$, let us have a look at the loop correction to the $n_1 n_2^2$ vertex:

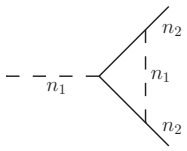

$$= \Lambda_{122}^3 \int \frac{dq^2}{16\pi^2} \frac{q^2}{(q^2 - m_2^2)^2(q^2 - m_1^2)} = \Lambda_{122} \frac{\lambda_{122}}{2\pi} f\left(\frac{m_2}{m_1}\right) \tag{4.65}$$

The function $f(m_2/m_1)$, ranges between 0 and 1 and so taking $\lambda_{122} \sim 1$ already seems to ensure the one-loop correction is subleading to the tree-level amplitude.

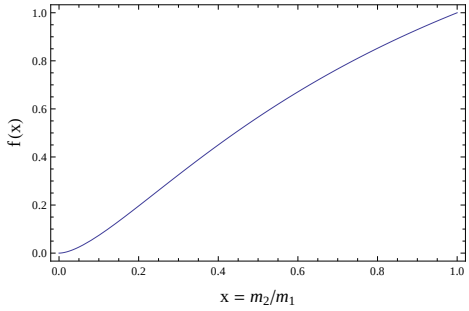

However, the estimate for one-loop correction to the mass of n_2 becomes of the order of m_2 for a cut-off scale Λ:

$$\frac{\Lambda_{122}^2}{16\pi^2} \ln\left(\frac{\Lambda^2}{m_2^2}\right) = \frac{\lambda_{122} m_2^2}{\pi} \ln\left(\frac{\Lambda^2}{m_2^2}\right) = m_2^2, \tag{4.66}$$

which implies:

$$\Lambda = m_2 \exp\left(\frac{\pi}{2\lambda_{122}}\right) \tag{4.67}$$

When $\lambda_{122} = 1/3$ the cut-off scale is roughly $\Lambda \sim 100 m_2$, already quite low. Nevertheless, for the masses of n_2 we will consider this cut-off scale is still higher than the mass of the B mesons.

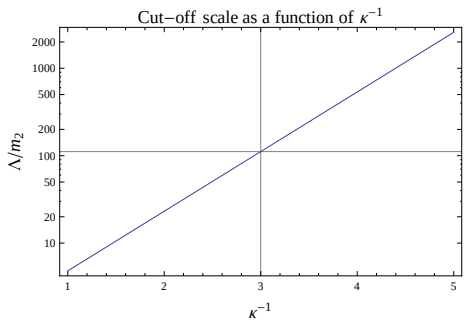

However, should we be satisfied with an order percent fine-tunning, $\pi/(2\lambda_{122})$ is replaced with $100\pi/(2\lambda 122)$. This pushes available range of λ_{122} to ~ 30 far out of the perturbative regime.

4.6.9 Estimates of Branching Ratios for a Light Higgs with χPT for $m_2 < 2m_K$

In this mass regime we can use χPT to compare the decay widths $\Gamma(n_2 \to \ell^+\ell^-)$ and $\Gamma(n_2 \to \pi^a\pi_a)$. Although $n_2 \to \gamma\gamma$ is allowed, it is unimportant unless $m_2 < 2m_e$. Coupling of light Higgs boson is well described by [135] and we follow their reasoning. The basic trick is to express the effective Higgs coupling in terms of operators that are easily evaluated within χPT. The effective theory for SM Higgs coupling to gluons and quarks can be obtained from integrating out the N_h heavy quark loops:

$$\mathcal{L}_{eff} = \frac{h}{v}\left(\frac{\alpha_s N_h}{12\pi}G^{\mu\nu}G_{\mu\nu} - m_u\bar{u}u - m_d\bar{d}d - m_s\bar{s}s\right) \tag{4.68}$$

For a 2HDM this can be easily translated in the h_u, h_d basis:

$$\mathcal{L}_{eff} = \frac{h_u}{v_u}\left(\frac{\alpha_s N_H^u}{12\pi}G^{\mu\nu}G_{\mu\nu} - m_u\bar{u}u\right) + \frac{h_d}{v_d}\left(\frac{\alpha_s N_H^d}{12\pi}G^{\mu\nu}G_{\mu\nu} - m_d\bar{d}d - m_s\bar{s}s\right) \tag{4.69}$$

In our case $N_h^u = 2$ and $N_h^d = 1$. As a result the n_2 coupling is given by:

$$\mathcal{L}_{eff} = \epsilon_2\frac{n_2}{v}\left[\frac{\cos\delta_2}{\sin\beta}\left(\frac{2\alpha_s}{12\pi}G^{\mu\nu}G_{\mu\nu} - m_u\bar{u}u\right) + \frac{\sin\delta_2}{\cos\beta}\left(\frac{\alpha_s}{12\pi}G^{\mu\nu}G_{\mu\nu} - m_d\bar{d}d - m_s\bar{s}s\right)\right] \tag{4.70}$$

This is very similar to the trace of the stress-energy tensor for the gluons and fermions of this effective theory:

$$\theta^\mu_\mu = -\frac{9\alpha_s}{8\pi}G^{\mu\nu}G_{\mu\nu} + \sum m_q\bar{q}q \to G^{\mu\nu}G_{\mu\nu} = \frac{8\pi}{9\alpha_s}\left(\sum m_q\bar{q}q - \theta^\mu_\mu\right) \tag{4.71}$$

And so we can express the effective coupling in terms of the stress-energy tensor and quark mass operator:

$$\mathcal{L}_{eff} = -\epsilon_2\frac{n_2}{v}\left[\frac{2N_E}{27}\theta^\mu_\mu + \left(\frac{\cos\delta_2}{\sin\beta} - \frac{2N_E}{27}\right)m_u\bar{u}u + \left(\frac{\sin\delta_2}{\cos\beta} - \frac{2N_E}{27}\right)\left(m_d\bar{d}d + m_s\bar{s}s\right)\right] \tag{4.72}$$

where the effective number of heavy flavors N_E depends on the couplings:

$$N_E = \left(2\frac{\cos\delta_2}{\sin\beta} + \frac{\sin\delta_2}{\cos\beta}\right) \tag{4.73}$$

On the χPT side, working with $\mathcal{L}_2$ to the leading order, the stress-energy tensor is simple:

$$\theta^{\mu}_{\ \mu} = g^{\mu\nu}\theta_{\mu\nu} = g^{\mu\nu}\frac{2}{\sqrt{-g}}\frac{\delta(\sqrt{-g}\mathcal{L}_2)}{\delta g^{\mu\nu}} = -2\mathcal{L}_2 \tag{4.74}$$

and so the matrix elements for transition to two pions is easy to evaluate:

$$\langle\pi_a\pi_b|\theta^{\mu}_{\ \mu}(q^2)|0\rangle = (q^2 + 2m_\pi^2)\delta_{ab} \tag{4.75}$$

We can similarly evaluate the matrix elements for the quark mass operators (since χPT predicts how pion mass depends on the quark masses):

$$\langle\pi_a\pi_b|\bar{q}q|0\rangle\rangle\pi_a\pi_b|\frac{f_\pi^2 m_0}{2}\frac{\partial \mathrm{Tr}(M\Sigma + M^\dagger\Sigma^\dagger)}{\partial m_q}|0\rangle \tag{4.76}$$

and so ignoring electromagnetic corrections we can evaluate the necessary matrix elements:

$$\begin{aligned}\langle\pi^+\pi^-|m_u\bar{u}u|0\rangle = m_0 m_u &= \frac{1}{2}\left(m_\pi^2 + m_{K^+}^2 - m_{K^0}^2\right)\\ \langle\pi^+\pi^-|m_d\bar{d}d|0\rangle = m_0 m_d &= \frac{1}{2}\left(m_\pi^2 - m_{K^+}^2 + m_{K^0}^2\right)\end{aligned} \tag{4.77}$$

We put all these results together to obtain the desired matrix element for $n_2 \to \pi\pi$ decay:

$$\begin{aligned}&\langle\pi\pi|\mathcal{L}_{eff}|n_2\rangle = -\frac{\epsilon_2}{v}\times\\ &\times\left(\frac{\sin\delta_2}{\cos\beta}\right)\left(\frac{2}{27}\left(2T^{-1}_{\beta\delta_2}+1\right)(m_2^2+m_\pi^2) + \frac{1}{2}\left(T^{-1}_{\beta\delta_2}+1\right)m_\pi^2 + \frac{1}{2}\left(T^{-1}_{\beta\delta_2}-1\right)\left(m_{K^+}^2 - m_{K^0}^2\right)\right)\end{aligned} \tag{4.78}$$

This allows us to compare the relative width for hadronic and leptonic decays for $m_2 < 2m_K$. Since the muon branching fraction is proportional to $\epsilon_2 \sin\delta_2/\cos\beta$, the relative branching fraction is only sensitive to the two parameters: m_2 and the product $T_{\beta\delta_2} = \tan\beta\tan\delta_2$. We plot the comparison between the results based on [121] and those obtained from using tree-level unimproved χPT in figure 4.6.9.

4.7 Future Directions

There are several directions in which our study could be expanded. We have not covered all the decay modes this model allows. We estimate that the branching fractions for higher and higher multiplicity final states begin to drop when the phase space available to the final

state particles becomes small. In particular the final number of n_2s in the final state cannot exceed $m_B/m_2 \lesssim 17$. Investigating these spectacular $B \to\approx 30\mu$ decay modes might be fun. Since our Dark Sector is strongly coupled we believe that the effect of quartic and cubic couplings is comparable. However, a more detailed study of this claim could prove worthwhile. Full collider phenomenology of this model is also beyond the scope of this paper and would benefit from future attention. Some of the consequences of this model have already been described in terms of muon-jets and photon-jets. Finally we believe that having introduced new channels might dilute some of the Standard Model asymmetries in decays of B mesons.

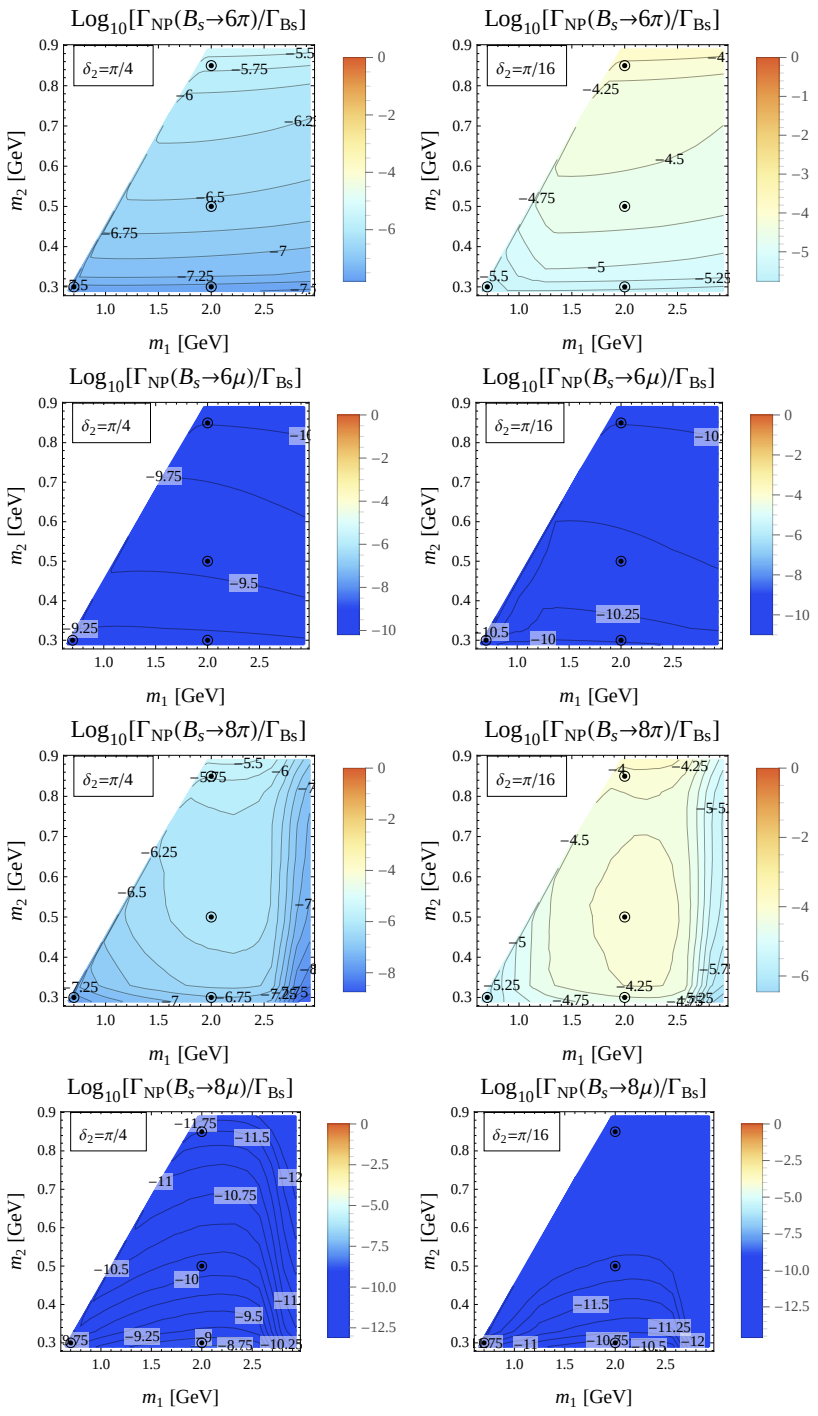

Figure 4.9: Six and Eight Particle Final States. The couplings between n_1 and n_2 are strong and we expect that additional particles in the final state do not significantly change the width for the process. It is clear that searching in the pure muonic channel would be fruitless. However, decays into purely hadronic decay channels should be abundant.

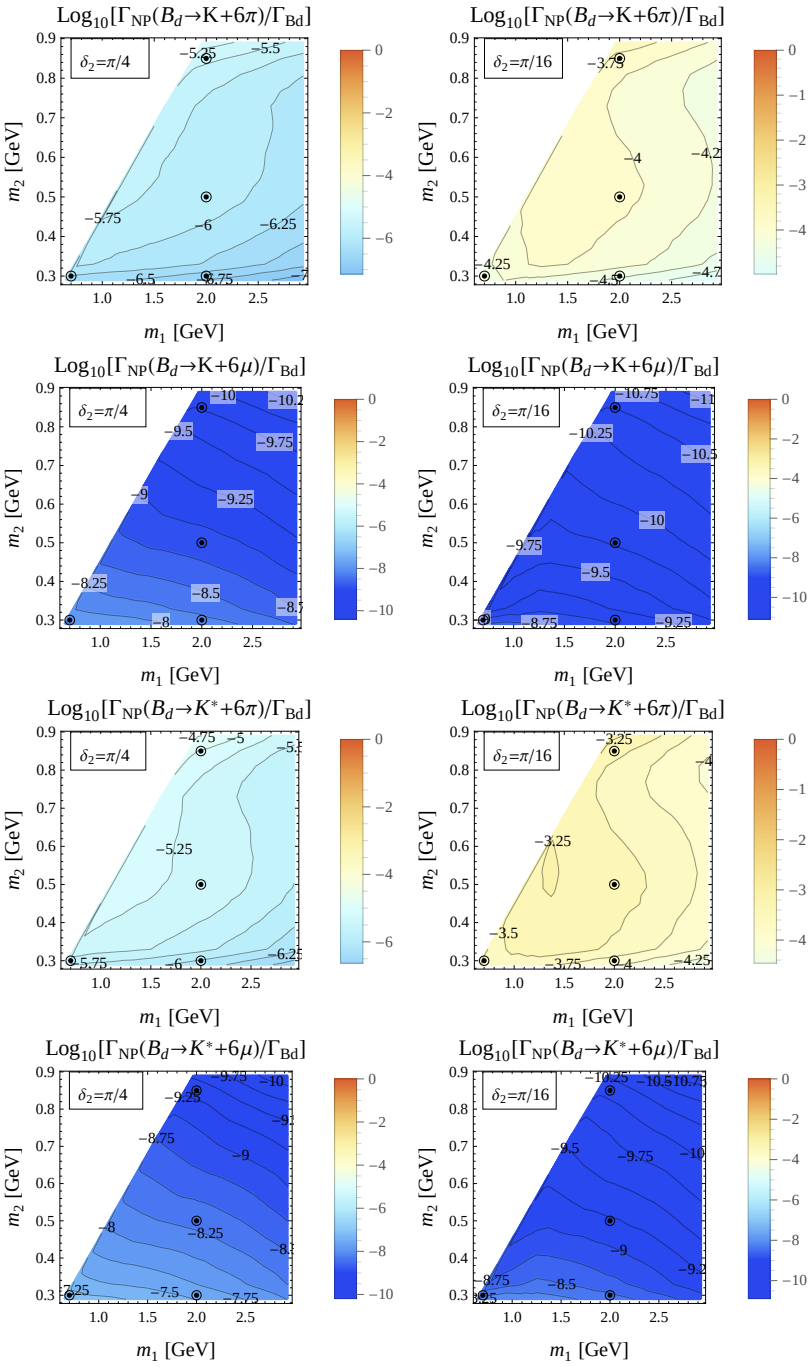

Figure 4.10: Seven Particle Final States. Additional meson in the final state can increase the branching fraction for the same Hidden Sector decay.

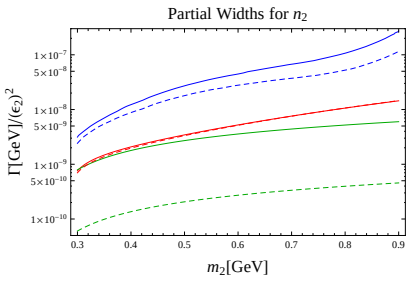

Figure 4.11: This plot shows partial width $\Gamma(n_2 \to \mu\mu)$ in green, $\Gamma(n_2 \to \pi\pi)$ according to tree-level χPT in red and $\Gamma(n_2 \to \pi\pi)$ based on improved χPT [121] in blue. The solid lines stand for $\delta_2 = \pi/4$, whereas the dashed lines mark the results for $\delta_2 = \pi/16$. The lack of change for tree-level χPT between $\delta_2 = \pi/4$ and $\delta_2 = \pi/16$ is caused by a numerical coincidence.

Chapter 5

CONCLUSION

It is very likely that there is a Dark Matter component to the energy density of our Universe. However, the precise structure of the Hidden Sector that contains this matter density remains completely unconstrained.

There are different ways to approach model building in the Hidden Sector. It is possible to build UV complete theories such as we presented in the Dark Photon project. It is also possible to study the phenomenology of low energy effective field theories as we have done in the Photon Jet project and the Hidden Sector and Heavy Flavor project.Each approach has its benefits. However, in order to facilitate the discovery of New Physics, I recommend an approach that explores as much signal space as possible. To this end, my colleagues and I have presented a simplified model of the Hidden Sector, responsible for both Photon Jets and multi-pion decays of B mesons.

BIBLIOGRAPHY

[1] B. Patt and F. Wilczek, "Higgs-field portal into hidden sectors," arXiv:hep-ph/0605188 [hep-ph].

[2] B. Holdom, "Two U(1)'s and Epsilon Charge Shifts," *Phys.Lett.* **B166** (1986) 196.

[3] R. Schabinger and J. D. Wells, "A Minimal spontaneously broken hidden sector and its impact on Higgs boson physics at the large hadron collider," *Phys.Rev.* **D72** (2005) 093007, arXiv:hep-ph/0509209 [hep-ph].

[4] M. J. Strassler and K. M. Zurek, "Echoes of a hidden valley at hadron colliders," *Phys.Lett.* **B651** (2007) 374–379, arXiv:hep-ph/0604261 [hep-ph].

[5] S. Dodelson, "Modern cosmology,".

[6] S. Weinberg, "Cosmology,".

[7] **Planck Collaboration** Collaboration, P. Ade *et al.*, "Planck 2013 results. I. Overview of products and scientific results," arXiv:1303.5062 [astro-ph.CO].

[8] F. Zwicky, "On the Masses of Nebulae and of Clusters of Nebulae," *Astrophysical Journal* **86** (1937) 217.

[9] V. C. Rubin and J. Ford, W. Kent, "Rotation of the Andromeda Nebula from a Spectroscopic Survey of Emission Regions," *Astrophysics Journal* **159** (1970) 379.

[10] J. D. Bekenstein, "The Modified Newtonian Dynamics: MOND and its implications for new physics," *Contemp.Phys.* (2007) , arXiv:astro-ph/0701848 [ASTRO-PH].

[11] **Supernova Search Team** Collaboration, A. G. Riess *et al.*, "Observational evidence from supernovae for an accelerating universe and a cosmological constant," *Astron.J.* **116** (1998) 1009–1038, arXiv:astro-ph/9805201 [astro-ph].

[12] P. Peebles and B. Ratra, "The Cosmological constant and dark energy," *Rev.Mod.Phys.* **75** (2003) 559–606, arXiv:astro-ph/0207347 [astro-ph].

[13] W. Hu, "Wayne Hu - Tutorials," May, 2013. http://background.uchicago.edu/~whu/.

[14] W. Hu and S. Dodelson, "Cosmic microwave background anisotropies," *Ann.Rev.Astron.Astrophys.* **40** (2002) 171–216, arXiv:astro-ph/0110414 [astro-ph].

[15] A. E. Nelson and J. Scholtz, "Dark Light, Dark Matter and the Misalignment Mechanism," *Phys.Rev.* **D84** (2011) 103501, arXiv:1105.2812 [hep-ph].

[16] M. Bullimore, J. P. Conlon, and L. T. Witkowski, "Kinetic mixing of U(1)s for local string models," *JHEP* **11** (2010) 142, arXiv:1009.2380 [hep-th].

[17] M. Goodsell, J. Jaeckel, J. Redondo, and A. Ringwald, "Naturally Light Hidden Photons in LARGE Volume String Compactifications," *JHEP* **11** (2009) 027, arXiv:0909.0515 [hep-ph].

[18] S. A. Abel, M. D. Goodsell, J. Jaeckel, V. V. Khoze, and A. Ringwald, "Kinetic Mixing of the Photon with Hidden U(1)s in String Phenomenology," *JHEP* **07** (2008) 124, arXiv:0803.1449 [hep-ph].

[19] E. C. G. Stueckelberg, "Interaction forces in electrodynamics and in the field theory of nuclear forces," *Helv. Phys. Acta* **11** (1938) 299–328.

[20] D. Feldman, Z. Liu, and P. Nath, "The Stueckelberg Z' extension with kinetic mixing and milli-charged dark matter from the hidden sector," *Phys. Rev.* **D75** (2007) 115001, arXiv:hep-ph/0702123.

[21] P. Fox, A. Pierce, and S. D. Thomas, "Probing a QCD string axion with precision cosmological measurements," arXiv:hep-th/0409059.

[22] A. D. Linde, "Inflation and Axion Cosmology," *Phys. Lett.* **B201** (1988) 437.

[23] M. S. Turner and F. Wilczek, "Inflationary axion cosmology," *Phys. Rev. Lett.* **66** (1991) 5–8.

[24] M. Tegmark, A. Aguirre, M. Rees, and F. Wilczek, "Dimensionless constants, cosmology and other dark matters," *Phys. Rev.* **D73** (2006) 023505, arXiv:astro-ph/0511774.

[25] J. Preskill, M. B. Wise, and F. Wilczek, "Cosmology of the invisible axion," *Phys. Lett.* **B120** (1983) 127–132.

[26] L. Abbott and P. Sikivie, "A Cosmological Bound on the Invisible Axion," *Phys.Lett.* **B120** (1983) 133–136.

[27] M. Dine and W. Fischler, "The not-so-harmless axion," *Phys. Lett.* **B120** (1983) 137–141.

[28] M. S. Turner, "Cosmic and local mass density of "invisible" axions," *Phys. Rev. D* **33** no. 4, (Feb, 1986) 889–896.

[29] M. Axenides, R. H. Brandenberger, and M. S. Turner, "Development of axion perturbations in an axion dominated universe," *Phys. Lett.* **B126** (1983) 178.

[30] D. H. Lyth, "A limit on the inflationary energy density from axion isocurvature fluctuations," *Phys. Lett.* **B236** (1990) 408.

[31] D. H. Lyth and E. D. Stewart, "Constraining the inflationary energy scale from axion cosmology," *Phys. Lett.* **B283** (1992) 189–193.

[32] M. Beltran, J. Garcia-Bellido, and J. Lesgourgues, "Isocurvature bounds on axions revisited," *Phys. Rev.* **D75** (2007) 103507, `arXiv:hep-ph/0606107`.

[33] S. D. Burns, "Isentropic and isocurvature axion perturbations in inflationary cosmology," `arXiv:astro-ph/9711303`.

[34] M. P. Hertzberg, M. Tegmark, and F. Wilczek, "Axion Cosmology and the Energy Scale of Inflation," *Phys. Rev.* **D78** (2008) 083507, `arXiv:0807.1726 [astro-ph]`.

[35] P. van Dokkum *et al.*, "Confirmation of the remarkable compactness of massive quiescent galaxies at z 2.3 : early-type galaxies did not form in a simple monolithic collapse," *Astrophys. J.* **677** (2008) L5–L8, `arXiv:0802.4094 [astro-ph]`.

[36] J. Redondo and M. Postma, "Massive hidden photons as lukewarm dark matter," *JCAP* **0902** (2009) 005, `arXiv:0811.0326 [hep-ph]`.

[37] C. Schwob, L. Jozefowski, B. de Beauvoir, L. Hilico, F. Nez, L. Julien, F. Biraben, O. Acef, J.-J. Zondy, and A. Clairon, "Optical Frequency Measurement of the $2S - 12D$ Transitions in Hydrogen and Deuterium: Rydberg Constant and Lamb Shift Determinations," *Phys. Rev. Lett.* **82** no. 25, (Jun, 1999) 4960–4963.

[38] M. Fischer, N. Kolachevsky, M. Zimmermann, R. Holzwarth, T. Udem, T. W. Hänsch, M. Abgrall, J. Grünert, I. Maksimovic, S. Bize, H. Marion, F. P. D. Santos, P. Lemonde, G. Santarelli, P. Laurent, A. Clairon, C. Salomon, M. Haas, U. D. Jentschura, and C. H. Keitel, "New Limits on the Drift of Fundamental Constants from Laboratory Measurements," *Phys. Rev. Lett.* **92** no. 23, (Jun, 2004) 230802.

[39] A. Mirizzi, J. Redondo, and G. Sigl, "Microwave Background Constraints on Mixing of Photons with Hidden Photons," *JCAP* **0903** (2009) 026, `arXiv:0901.0014 [hep-ph]`.

[40] M. Markevitch, W. R. Forman, C. L. Sarazin, and A. Vikhlinin, "The Temperature Structure of 30 Nearby Clusters Observed with ASCA. Similarity of Temperature Profiles," *Astrophys. J.* **503** (1998) 77, arXiv:astro-ph/9711289.

[41] J. H. Croston *et al.*, "Galaxy-cluster gas-density distributions of the Representative XMM-Newton Cluster Structure Survey (REXCESS)," arXiv:0801.3430 [astro-ph].

[42] A. Wagner, G. Rybka, M. Hotz, L. J. Rosenberg, S. J. Asztalos, G. Carosi, C. Hagmann, D. Kinion, K. van Bibber, J. Hoskins, C. Martin, P. Sikivie, D. B. Tanner, R. Bradley, and J. Clarke, "Search for Hidden Sector Photons with the ADMX Detector," *Phys. Rev. Lett.* **105** no. 17, (Oct, 2010) 171801.

[43] J. D. Jackson, *Classical Electrodynamics Third Edition*. Wiley, 1998.

[44] A. Martin, W. Stirling, R. Thorne, and G. Watt, "Parton distributions for the LHC," *Eur.Phys.J.* **C63** (2009) 189–285, arXiv:0901.0002 [hep-ph].

[45] **ATLAS Collaboration** Collaboration, G. Aad *et al.*, "The ATLAS Experiment at the CERN Large Hadron Collider," *JINST* **3** (2008) S08003.

[46] CERN, "CERN," May, 2013. http://home.web.cern.ch/.

[47] **ATLAS Collaboration** Collaboration, G. Aad *et al.*, "Expected Performance of the ATLAS Experiment - Detector, Trigger and Physics," arXiv:0901.0512 [hep-ex].

[48] S. D. Ellis and D. E. Soper, "Successive combination jet algorithm for hadron collisions," *Phys.Rev.* **D48** (1993) 3160–3166, arXiv:hep-ph/9305266 [hep-ph].

[49] Y. L. Dokshitzer, G. Leder, S. Moretti, and B. Webber, "Better jet clustering algorithms," *JHEP* **9708** (1997) 001, arXiv:hep-ph/9707323 [hep-ph].

[50] M. Cacciari, G. P. Salam, and G. Soyez, "The Anti-k(t) jet clustering algorithm," *JHEP* **0804** (2008) 063, arXiv:0802.1189 [hep-ph].

[51] M. H. Seymour, "Searches for new particles using cone and cluster jet algorithms: A Comparative study," *Z.Phys.* **C62** (1994) 127–138.

[52] J. Butterworth, B. Cox, and J. R. Forshaw, "WW scattering at the CERN LHC," *Phys.Rev.* **D65** (2002) 096014, arXiv:hep-ph/0201098 [hep-ph].

[53] J. M. Butterworth, A. R. Davison, M. Rubin, and G. P. Salam, "Jet substructure as a new Higgs search channel at the LHC," *Phys.Rev.Lett.* **100** (2008) 242001, arXiv:0802.2470 [hep-ph].

[54] J. Shelton, "TASI Lectures on Jet Substructure," arXiv:1302.0260 [hep-ph].

[55] J. Thaler and K. Van Tilburg, "Identifying Boosted Objects with N-subjettiness," *JHEP* **1103** (2011) 015, arXiv:1011.2268 [hep-ph].

[56] J. Thaler and K. Van Tilburg, "Maximizing Boosted Top Identification by Minimizing N-subjettiness," *JHEP* **1202** (2012) 093, arXiv:1108.2701 [hep-ph].

[57] S. D. Ellis, T. S. Roy, and J. Scholtz, "Phenomenology of Photon-Jets," *Phys.Rev.* **D87** (2013) 014015, arXiv:1210.3657 [hep-ph].

[58] **ATLAS Collaboration** Collaboration, G. Aad *et al.*, "Observation of a new particle in the search for the Standard Model Higgs boson with the ATLAS detector at the LHC," *Phys.Lett.B* (2012) , arXiv:1207.7214 [hep-ex].

[59] **CMS Collaboration** Collaboration, S. Chatrchyan *et al.*, "Observation of a new boson at a mass of 125 GeV with the CMS experiment at the LHC," *Phys.Lett.B* (2012) , arXiv:1207.7235 [hep-ex].

[60] B. A. Dobrescu, G. L. Landsberg, and K. T. Matchev, "Higgs boson decays to CP odd scalars at the Tevatron and beyond," *Phys.Rev.* **D63** (2001) 075003, arXiv:hep-ph/0005308 [hep-ph].

[61] N. Toro and I. Yavin, "Multiphotons and Photon-Jets," arXiv:1202.6377 [hep-ph].

[62] P. Draper and D. McKeen, "Diphotons from Tetraphotons in the Decay of a 125 GeV Higgs at the LHC," *Phys.Rev.* **D85** (2012) 115023, arXiv:1204.1061 [hep-ph].

[63] "Search for a Higgs boson decaying to four photons through light CP-odd scalar coupling using full luminosity of the 7 $\sim$ TeV pp collision data taken with ATLAS detector at the LHC," Tech. Rep. ATLAS-CONF-2012-079, CERN, Geneva, Jul, 2012.

[64] G. Brooijmans, "High pT Hadronic Top Quark Identification," Tech. Rep. ATL-PHYS-CONF-2008-008. ATL-COM-PHYS-2008-001, CERN, Geneva, Jan, 2008.

[65] J. Butterworth, J. R. Ellis, and A. Raklev, "Reconstructing sparticle mass spectra using hadronic decays," *JHEP* **0705** (2007) 033, arXiv:hep-ph/0702150 [HEP-PH].

[66] J. Thaler and L.-T. Wang, "Strategies to Identify Boosted Tops," *JHEP* **0807** (2008) 092, arXiv:0806.0023 [hep-ph].

[67] D. E. Kaplan, K. Rehermann, M. D. Schwartz, and B. Tweedie, "Top Tagging: A Method for Identifying Boosted Hadronically Decaying Top Quarks," *Phys.Rev.Lett.* **101** (2008) 142001, arXiv:0806.0848 [hep-ph].

[68] J. M. Butterworth, A. R. Davison, M. Rubin, and G. P. Salam, "Jet substructure as a new Higgs search channel at the LHC," *AIP Conf.Proc.* **1078** (2009) 189–191, arXiv:0809.2530 [hep-ph].

[69] J. M. Butterworth, A. R. Davison, M. Rubin, and G. P. Salam, "Jet substructure as a new Higgs search channel at the LHC," arXiv:0810.0409 [hep-ph].

[70] S. D. Ellis, C. K. Vermilion, and J. R. Walsh, "Techniques for improved heavy particle searches with jet substructure," *Phys.Rev.* **D80** (2009) 051501, arXiv:0903.5081 [hep-ph].

[71] S. D. Ellis, C. K. Vermilion, and J. R. Walsh, "Recombination Algorithms and Jet Substructure: Pruning as a Tool for Heavy Particle Searches," *Phys.Rev.* **D81** (2010) 094023, arXiv:0912.0033 [hep-ph].

[72] D. Krohn, J. Thaler, and L.-T. Wang, "Jet Trimming," *JHEP* **1002** (2010) 084, arXiv:0912.1342 [hep-ph].

[73] "Performance of large-R jets and jet substructure reconstruction with the ATLAS detector," Tech. Rep. ATLAS-CONF-2012-065, CERN, Geneva, Jul, 2012.

[74] **CMS Collaboration** Collaboration, "Search for qW/qZ/WW/WZ/ZZ-Resonances in the W/Z-tagged Dijet Mass Spectrum from 7 TeV pp Collisions at CMS," Tech. Rep. CMS-PAS-EXO-11-095, CERN, Geneva, 2012.

[75] T. Plehn, G. P. Salam, and M. Spannowsky, "Fat Jets for a Light Higgs," *Phys.Rev.Lett.* **104** (2010) 111801, arXiv:0910.5472 [hep-ph].

[76] J. Gallicchio, J. Huth, M. Kagan, M. D. Schwartz, K. Black, *et al.*, "Multivariate discrimination and the Higgs + W/Z search," *JHEP* **1104** (2011) 069, arXiv:1010.3698 [hep-ph].

[77] C. Hackstein and M. Spannowsky, "Boosting Higgs discovery: The Forgotten channel," *Phys.Rev.* **D82** (2010) 113012, arXiv:1008.2202 [hep-ph].

[78] G. D. Kribs, A. Martin, T. S. Roy, and M. Spannowsky, "Discovering the Higgs Boson in New Physics Events using Jet Substructure," *Phys.Rev.* **D81** (2010) 111501, arXiv:0912.4731 [hep-ph].

[79] G. D. Kribs, A. Martin, T. S. Roy, and M. Spannowsky, "Discovering Higgs Bosons of the MSSM using Jet Substructure," *Phys.Rev.* **D82** (2010) 095012, arXiv:1006.1656 [hep-ph].

[80] G. D. Kribs, A. Martin, and T. S. Roy, "Higgs boson discovery through top-partners decays using jet substructure," *Phys.Rev.* **D84** (2011) 095024, arXiv:1012.2866 [hep-ph].

[81] A. Katz, M. Son, and B. Tweedie, "Ditau-Jet Tagging and Boosted Higgses from a Multi-TeV Resonance," *Phys.Rev.* **D83** (2011) 114033, arXiv:1011.4523 [hep-ph].

[82] C. Englert, T. S. Roy, and M. Spannowsky, "Ditau jets in Higgs searches," *Phys.Rev.* **D84** (2011) 075026, arXiv:1106.4545 [hep-ph].

[83] M. Son, C. Spethmann, and B. Tweedie, "Diboson-Jets and the Search for Resonant Zh Production," arXiv:1204.0525 [hep-ph].

[84] A. Abdesselam, E. B. Kuutmann, U. Bitenc, G. Brooijmans, J. Butterworth, *et al.*, "Boosted objects: A Probe of beyond the Standard Model physics," *Eur.Phys.J.* **C71** (2011) 1661, arXiv:1012.5412 [hep-ph].

[85] A. Altheimer, S. Arora, L. Asquith, G. Brooijmans, J. Butterworth, *et al.*, "Jet Substructure at the Tevatron and LHC: New results, new tools, new benchmarks," *J.Phys.G* **G39** (2012) 063001, arXiv:1201.0008 [hep-ph].

[86] **LHC New Physics Working Group** Collaboration, D. Alves *et al.*, "Simplified Models for LHC New Physics Searches," arXiv:1105.2838 [hep-ph].

[87] J. Alwall, M. Herquet, F. Maltoni, O. Mattelaer, and T. Stelzer, "MadGraph 5 : Going Beyond," *JHEP* **1106** (2011) 128, arXiv:1106.0522 [hep-ph].

[88] T. Sjostrand, S. Mrenna, and P. Z. Skands, "PYTHIA 6.4 Physics and Manual," *JHEP* **0605** (2006) 026, arXiv:hep-ph/0603175 [hep-ph].

[89] T. Sjostrand, S. Mrenna, and P. Z. Skands, "A Brief Introduction to PYTHIA 8.1," *Comput.Phys.Commun.* **178** (2008) 852–867, arXiv:0710.3820 [hep-ph].

[90] private correspondence with Henry Lubatti.

[91] M. Cacciari and G. P. Salam, "Dispelling the N^3 myth for the k_t jet-finder," *Phys.Lett.* **B641** (2006) 57–61, arXiv:hep-ph/0512210 [hep-ph].

[92] M. Cacciari, G. P. Salam, and G. Soyez, "FastJet user manual," *Eur.Phys.J.* **C72** (2012) 1896, arXiv:1111.6097 [hep-ph].

[93] S. Catani, Y. L. Dokshitzer, M. Seymour, and B. Webber, "Longitudinally invariant K_t clustering algorithms for hadron hadron collisions," *Nucl.Phys.* **B406** (1993) 187–224.

[94] M. Wobisch and T. Wengler, "Hadronization corrections to jet cross-sections in deep inelastic scattering," arXiv:hep-ph/9907280 [hep-ph].

[95] M. Wobisch, "Measurement and QCD analysis of jet cross-sections in deep inelastic positron proton collisions at s**(1/2) = 300-GeV,".

[96] I. W. Stewart, F. J. Tackmann, and W. J. Waalewijn, "N-Jettiness: An Inclusive Event Shape to Veto Jets," *Phys.Rev.Lett.* **105** (2010) 092002, arXiv:1004.2489 [hep-ph].

[97] S. D. Ellis, A. Hornig, T. S. Roy, D. Krohn, and M. D. Schwartz, "Qjets: A Non-Deterministic Approach to Tree-Based Jet Substructure," *Phys.Rev.Lett.* **108** (2012) 182003, arXiv:1201.1914 [hep-ph].

[98] M. Cacciari, G. P. Salam, and G. Soyez, "The Catchment Area of Jets," *JHEP* **0804** (2008) 005, arXiv:0802.1188 [hep-ph].

[99] Y. Freund and R. E. Schapire, "Experiments with a New Boosting Algorithm,".

[100] A. Hocker, J. Stelzer, F. Tegenfeldt, H. Voss, K. Voss, *et al.*, "TMVA - Toolkit for Multivariate Data Analysis," *PoS* **ACAT** (2007) 040, arXiv:physics/0703039 [PHYSICS].

[101] S. D. Ellis, T. S. Roy, and J. Scholtz, "Phenomenology of Photon Jets," arXiv:in preparation [hep-ph].

[102] J. T. Ruderman and T. Volansky, "Decaying into the Hidden Sector," *JHEP* **1002** (2010) 024, arXiv:0908.1570 [hep-ph].

[103] C. Cheung, J. T. Ruderman, L.-T. Wang, and I. Yavin, "Lepton Jets in (Supersymmetric) Electroweak Processes," *JHEP* **1004** (2010) 116, arXiv:0909.0290 [hep-ph].

[104] A. Falkowski, J. T. Ruderman, T. Volansky, and J. Zupan, "Hidden Higgs Decaying to Lepton Jets," *JHEP* **1005** (2010) 077, arXiv:1002.2952 [hep-ph].

[105] A. Falkowski, J. T. Ruderman, T. Volansky, and J. Zupan, "Discovering Higgs Decays to Lepton Jets at Hadron Colliders," *Phys.Rev.Lett.* **105** (2010) 241801, arXiv:1007.3496 [hep-ph].

[106] J. Conway, R. Culbertson, R. Demina, B. Kilminster, M. Kruse, S. Mrenna, J. Nielsen, M. Roco, A. Pierce, J. Thaler, and T. Wizansky, "PGS4: Pretty Good Simulation of high energy collision,". http://www.physics.ucdavis.edu/~conway/research/software/pgs/pgs4-general.htm.

[107] N. Arkani-Hamed and N. Weiner, "LHC Signals for a SuperUnified Theory of Dark Matter," *JHEP* **0812** (2008) 104, arXiv:0810.0714 [hep-ph].

[108] M. A. Shifman, A. Vainshtein, and V. I. Zakharov, "Light Quarks and the Origin of the Delta I = 1/2 Rule in the Nonleptonic Decays of Strange Particles," *Nucl.Phys.* **B120** (1977) 316.

[109] M. A. Shifman, "Foreword to ITEP lectures in particle physics," arXiv:hep-ph/9510397 [hep-ph].

[110] **LHCb collaboration** Collaboration, R. Aaij *et al.*, "Measurement of the $B_s^0 \to \mu^+\mu^-$ branching fraction and search for $B^0 \to \mu^+\mu^-$ decays at the LHCb experiment," arXiv:1307.5024 [hep-ex].

[111] **Particle Data Group** Collaboration, J. Beringer *et al.*, "Review of Particle Physics (RPP)," *Phys.Rev.* **D86** (2012) 010001.

[112] BaBar, "BaBar Experiment," 2013. http://www-public.slac.stanford.edu/babar/default.aspx.

[113] Belle, "Belle Experiment," 2013. http://belle.kek.jp/.

[114] **BaBar Collaboration** Collaboration, B. Aubert *et al.*, "The BaBar detector," *Nucl.Instrum.Meth.* **A479** (2002) 1–116, arXiv:hep-ex/0105044 [hep-ex].

[115] LHCb, "LHCb Experiment," 2013. http://lhcb.web.cern.ch/lhcb/.

[116] **Heavy Flavor Averaging Group** Collaboration, Y. Amhis *et al.*, "Averages of B-Hadron, C-Hadron, and tau-lepton properties as of early 2012," arXiv:1207.1158 [hep-ex].

[117] J. Laiho, E. Lunghi, and R. S. Van de Water, "Lattice QCD inputs to the CKM unitarity triangle analysis," *Phys.Rev.* **D81** (2010) 034503, arXiv:0910.2928 [hep-ph].

[118] C. W. Bauer, S. Fleming, D. Pirjol, and I. W. Stewart, "An Effective field theory for collinear and soft gluons: Heavy to light decays," *Phys.Rev.* **D63** (2001) 114020, arXiv:hep-ph/0011336 [hep-ph].

[119] G. Branco, P. Ferreira, L. Lavoura, M. Rebelo, M. Sher, *et al.*, "Theory and phenomenology of two-Higgs-doublet models," *Phys.Rept.* **516** (2012) 1–102, arXiv:1106.0034 [hep-ph].

[120] C.-Y. Chen, S. Dawson, and M. Sher, "Heavy Higgs Searches and Constraints on Two Higgs Doublet Models," arXiv:1305.1624 [hep-ph].

[121] J. F. Donoghue, J. Gasser, and H. Leutwyler, "The Decay Of a Light Higgs Boson," *Nucl.Phys.* **B343** (1990) 341–368.

[122] B. Batell, M. Pospelov, and A. Ritz, "Multi-lepton Signatures of a Hidden Sector in Rare B Decays," *Phys.Rev.* **D83** (2011) 054005, arXiv:0911.4938 [hep-ph].

[123] C. Bouchard, G. P. Lepage, C. Monahan, H. Na, and J. Shigemitsu, "Standard Model predictions for $B \to K\ell\ell$ with form factors from lattice QCD," arXiv:1306.0434 [hep-ph].

[124] M. Beneke, T. Feldmann, and D. Seidel, "Systematic approach to exclusive $B \to V\ell^+\ell^-, V\gamma$ decays," *Nucl.Phys.* **B612** (2001) 25–58, arXiv:hep-ph/0106067 [hep-ph].

[125] C. Geng and C. Liu, "Study of $B_s \to (\eta,\, \eta',\, \phi)\ell\bar{\ell}$ decays," *J.Phys.* **G29** (2003) 1103–1118, arXiv:hep-ph/0303246 [hep-ph].

[126] P. Ball and R. Zwicky, "New results on $B \to \pi, K, \eta$ decay formfactors from light-cone sum rules," *Phys.Rev.* **D71** (2005) 014015, arXiv:hep-ph/0406232 [hep-ph].

[127] P. Ball and R. Zwicky, "$B_{d,s} \to \rho, \omega, K^*, \phi$ decay form-factors from light-cone sum rules revisited," *Phys.Rev.* **D71** (2005) 014029, arXiv:hep-ph/0412079 [hep-ph].

[128] **Belle** Collaboration, H. Hyun *et al.*, "Search for a Low Mass Particle Decaying into $\mu^+\mu^-$ in $B^0 \to K^{*0}X$ and $B^0 \to \rho^0 X$ at Belle," *Phys.Rev.Lett.* **105** (2010) 091801, arXiv:1005.1450 [hep-ex].

[129] A. J. Buras, J. Girrbach, D. Guadagnoli, and G. Isidori, "On the Standard Model prediction for BR($B_{s,d} \to \mu^+\mu^-$)," *Eur.Phys.J.* **C72** (2012) 2172, arXiv:1208.0934 [hep-ph].

[130] A. Ali, G. Kramer, Y. Li, C.-D. Lu, Y.-L. Shen, *et al.*, "Charmless non-leptonic B_s decays to PP, PV and VV final states in the pQCD approach," *Phys.Rev.* **D76** (2007) 074018, arXiv:hep-ph/0703162 [HEP-PH].

[131] A. R. Williamson and J. Zupan, "Two body B decays with isosinglet final states in SCET," *Phys.Rev.* **D74** (2006) 014003, arXiv:hep-ph/0601214 [hep-ph].

[132] D. Melikhov and N. Nikitin, "Rare radiative leptonic decays $B_{d,s} \to \ell^+\ell^-\gamma$," *Phys.Rev.* **D70** (2004) 114028, arXiv:hep-ph/0410146 [hep-ph].

[133] A. Lenz, U. Nierste, J. Charles, S. Descotes-Genon, H. Lacker, *et al.*, "Constraints on new physics in $B - \bar{B}$ mixing in the light of recent LHCb data," *Phys.Rev.* **D86** (2012) 033008, arXiv:1203.0238 [hep-ph].

[134] A. Lenz, U. Nierste, J. Charles, S. Descotes-Genon, A. Jantsch, *et al.*, "Anatomy of New Physics in $B - \bar{B}$ mixing," *Phys.Rev.* **D83** (2011) 036004, arXiv:1008.1593 [hep-ph].

[135] J. F. Gunion, H. E. Haber, G. L. Kane, and S. Dawson, "The Higgs Hunter's Guide," *Front.Phys.* **80** (2000) 1–448.

[136] S. Forte and G. Watt, "Progress in the Determination of the Partonic Structure of the Proton," arXiv:1301.6754 [hep-ph].

[137] B. R. Heckel, E. G. Adelberger, C. E. Cramer, T. S. Cook, S. Schlamminger, and U. Schmidt, "Preferred-frame and CP-violation tests with polarized electrons," *Phys. Rev. D* **78** no. 9, (Nov, 2008) 092006.

[138] J. Jaeckel, J. Redondo, and A. Ringwald, "Signatures of a hidden cosmic microwave background," *Phys. Rev. Lett.* **101** (2008) 131801, arXiv:0804.4157 [astro-ph].

[139] D. F. Bartlett and S. Loegl, "LIMITS ON AN ELECTROMAGNETIC FIFTH FORCE," *Phys. Rev. Lett.* **61** (1988) 2285–2287.

[140] H. Yuksel and M. D. Kistler, "Dark Matter Might Decay... Just Not Today!," *Phys. Rev.* **D78** (2008) 023502, arXiv:0711.2906 [astro-ph].

[141] M. Ahlers, H. Gies, J. Jaeckel, J. Redondo, and A. Ringwald, "Light from the Hidden Sector," *Phys. Rev.* **D76** (2007) 115005, arXiv:0706.2836 [hep-ph].

[142] B. Holdom, "Two U(1)'s and Epsilon Charge Shifts," *Phys. Lett.* **B166** (1986) 196.

[143] C. J. Hogan, "Cosmic fluctuations and dark matter from scalar field oscillations," *Phys. Rev. Lett.* **74** (1995) 3105–3108, astro-ph/9412054.

[144] A. D. Linde, "Axions in inflationary cosmology," *Phys. Lett.* **B259** (1991) 38–47.

[145] S.-Y. Pi, "Axion Dominated Inflationary Universe,". Presented at Conf. on 5th Unification Workshop, Providence, RI, Apr 12-14, 1984.

[146] G. G. Raffelt, *Stars as laboratories for fundamental physics: The astrophysics of neutrinos, axions, and other weakly interacting particles*. Chicago Univ. Pr., 1996.

[147] M. Kawasaki and T. Yanagida, "Are isocurvature fluctuations of the M-theory axion observable?," *Prog. Theor. Phys.* **97** (1997) 809–812, `arXiv:hep-ph/9703261`.

[148] D. Seckel and M. S. Turner, "Isothermal Density Perturbations in an Axion Dominated Inflationary Universe," *Phys. Rev.* **D32** (1985) 3178.

[149] D. Chelouche, R. Rabadan, S. Pavlov, and F. Castejon, "Spectral Signatures of Photon-Particle Oscillations from Celestial Objects," `arXiv:0806.0411 [astro-ph]`.

[150] K. M. Zurek, C. J. Hogan, and T. R. Quinn, "Astrophysical effects of scalar dark matter miniclusters," *Phys. Rev.* **D75** (2007) 043511, `arXiv:astro-ph/0607341`.

[151] A. De Angelis, O. Mansutti, M. Persic, and M. Roncadelli, "Photon propagation and the VHE gamma-ray spectra of blazars: how transparent is really the Universe?," `arXiv:0807.4246 [astro-ph]`.

[152] G. G. Raffelt, "Astrophysical axion bounds," *Lect. Notes Phys.* **741** (2008) 51–71, `arXiv:hep-ph/0611350`.

[153] G. Raffelt and L. Stodolsky, "Mixing of the Photon with Low Mass Particles," *Phys. Rev.* **D37** (1988) 1237.

[154] H. Murayama, G. G. Raffelt, C. Hagmann, K. van Bibber, and L. J. Rosenberg, "Axions and other very light bosons: in Review of Particle Physics (RPP 1998)," *Eur. Phys. J.* **C3** (1998) 264–271.

[155] J.-P. Uzan, "The fundamental constants and their variation: Observational status and theoretical motivations," *Rev. Mod. Phys.* **75** (2003) 403, `arXiv:hep-ph/0205340`.

[156] "Expected photon performance in the ATLAS experiment," Tech. Rep. ATL-PHYS-PUB-2011-007, CERN, Geneva, Apr, 2011.

[157] G. L. Bayatian, S. Chatrchyan, G. Hmayakyan, A. M. Sirunyan, W. Adam, T. Bergauer, and Dragicevic, "CMS physics Technical Design Report, Volume II: Physics Performance . oai:cds.cern.ch:942733," *J. Phys. G* **34** no. CERN-LHCC-2006-021. CMS-TDR-008-2, (2006) 995–1579. 669 p. revised version submitted on 2006-09-22 17:44:47.

[158] S. Bock, R. Lafaye, T. Plehn, M. Rauch, D. Zerwas, *et al.*, "Measuring Hidden Higgs and Strongly-Interacting Higgs Scenarios," *Phys.Lett.* **B694** (2010) 44–53, arXiv:1007.2645 [hep-ph].

[159] R. Harnik, J. Kopp, and J. Zupan, "Flavor Violating Higgs Decays," arXiv:1209.1397 [hep-ph].

[160] A. Ali, P. Ball, L. Handoko, and G. Hiller, "A Comparative study of the decays $B \to (K,\, K^*)\, \ell^+\ell^-$ in standard model and supersymmetric theories," *Phys.Rev.* **D61** (2000) 074024, arXiv:hep-ph/9910221 [hep-ph].

[161] U. Nierste, "Three Lectures on Meson Mixing and CKM phenomenology," arXiv:0904.1869 [hep-ph].

[162] F. Bezrukov and D. Gorbunov, "Light inflaton Hunter's Guide," *JHEP* **1005** (2010) 010, arXiv:0912.0390 [hep-ph].

[163] J. R. Ellis, M. K. Gaillard, and D. V. Nanopoulos, "A Phenomenological Profile of the Higgs Boson," *Nucl.Phys.* **B106** (1976) 292.

[164] D. McKeen, "Constraining Light Bosons with Radiative Upsilon(1S) Decays," *Phys.Rev.* **D79** (2009) 015007, arXiv:0809.4787 [hep-ph].

[165] A. Manohar and H. Georgi, "Chiral quarks and the non-relativistic quark model," *Nuclear Physics B* **234** no. 1, (1984) 189 – 212.

[166] T. Sjöstrand, "Homepage for Torbjörn Sjöstrand," July, 2013.